Turning sediments into soil

Effects of soil ripening and stockpile management on tensile strength and cracking of dredged material: an experimental study

Gabriel Mainieri Franco

Delft University of Technology

TU Delft

Turning sediments into soil

Effects of soil ripening and stockpile management on tensile strength and cracking of dredged material: an experimental study

by

Gabriel Mainieri Franco

to obtain the degree of Master of Science

at the Delft University of Technology,

to be defended publicly on Friday August 22, 2025 at 1:00 PM.

Student number:	5125642
Project duration:	March, 2025 – August , 2025
Thesis Committee:	Dr. J. Gebert (Chair)
	Dr.ir. D.J.M. Ngan-Tillard
	Dr. C. Chassagne
	PhD Candidate N. Elnaker
Faculty:	Faculty of Civil Engineering and Geosciences, Delft

Cover: Identification of desiccation cracks in a sample. Image by: Gabriel Franco

An electronic version of this thesis is available at http://repository.tudelft.nl/.

TU Delft

Preface

When I first arrived in the Netherlands six years ago, I was only planning on completing my Bachelor here, and then continue my studies somewhere else. As I went through my studies however, I grew increasingly attached to Delft, and eventually decided on staying here, and continue unto my master. I am so grateful for this decision, as not only has it lead me to a career path I am excited to follow, but also made me cross paths with some amazing people on the way.

First, I would like to thank my thesis committee for supporting me in these last five months of my student life. Thank you to Julia and Nazeir for guiding me through this research, and their hard work in setting up this extremely important research of which I am grateful to be a part of. Thank you to Dominique for always having time for me, and providing insights from a different and valuable perspective. Thank you to Claire, for always being so excited about my research, and for teaching me valuable knowledge on soils during the Cross-Over I followed the quarter before my thesis.

Additionally, my experiments would not have been possible without the work of people outside the project. I would like to thank Ties de Jong for setting up the Brazilian test, and taking time to teach me how to use it. I would also like to thank Cristina Panez, for all the times she helped me situate myself in the lab when I was lost, and for helping me set-up my crack formation experiments.

Finally, I want to thank all the people that were a part of my life all these years. First my parents, who have always believed in me, and supported me all these years. My brother Lucas, who was always happy to meet and listen to me ramble. To my friends, I am incredibly grateful to have met you. The trashy queens, Bas, Paul, all of my fellow board 74/75 members, and Tjasa, who was the best thesis companion I could have hoped for.

It's been a great time in Delft, but I'm excited for the next chapter.

Gabriel Mainieri Franco
Delft, August 2025

Summary

Rising sea levels, combined with land subsidence, have heightened the concerns for safeguarding the coast and waterways of Europe. This effort will require a large amount of strained resources, such as marsh soil, which is becoming increasingly difficult to source. A promising alternative is utilizing the vast amount of dredged sediments extracted by ports each year. Studies have already been conducted on the feasibility of using such a material in dike construction and reinforcements, and guidelines have been developed. Treatment of the material is recommended before application, usually through stockpiling. Although this is widely accepted as a suitable method to treat sediments, the potential for optimizing it has been a subject of few studies.

Therefore, focusing on physical ripening, this thesis set out to investigate the evolution of tensile strength and crack formation over time under different stockpile management practices. This research was motivated by the observation that unripened material tends to develop shrinkage cracks when applied in a dike, which creates preferential channels for water to flow through. An important factor influencing the formation of cracks is the material's tensile strength. Other aspects investigated were the Coefficient of Linear Extensibility (COLE) , which characterizes the shrinkage behavior, and the Atterberg limits. The latter is an important parameter to determine the suitability of a material to be used in dikes.

This thesis investigated mechanically de-watered dredged sediments processed in the METHA plant in Hamburg. After processing, the sediments were stockpiled (1,000-2,200 m^3) with varying turning rates (none, 2x per year, and 4x per year) and vegetation management (removed before turning or not). Samples were collected over approximately two years, covering ripening times from six months to two and a half years.

The results showed that tensile strength increased significantly after one turning event to around 105% of the original material, likely due to aeration improving structural stability. However, subsequent turning events led to a drop in tensile strength. SP7 and SP9 (4x turning per year) exhibited tensile strength 30 % lower than the original material after two years of ripening, suggesting that the repeated mechanical breakdown degraded soil structure. At the end of the investigated period, tensile strength was found to be highest in the control stockpile, where no turning was applied and vegetation was allowed to grow.

Higher turning frequency, however, greatly benefited the compactability of the samples. When tensile strength tests were carried out compacting the samples to 95 % of their Proctor density, an increase in tensile strength of 430 % was found in the sample with the highest Proctor density (SP-9). In comparison, SP-4 (control) exhibited an increase of 280 % at 95 % Proctor density.

COLE values stabilized after two years to values approximately half of the original material. This indicates reduced shrinkage potential and, therefore, a lower tendency for crack formation in ripened sediments.

Crack formation experiments exhibited no consistent pattern across different stockpiling methods and ripening periods. Instead, the most influential factor appeared to be the reduction in shrinkage due to ripening. Crack Intensity Factor (CIF) and average crack width results were consistently lower in the stockpiled material than in the unripened original material. This was likely caused by the reduced shrinkage behavior observed in COLE tests.

Finally, the results of the Atterberg limits determination showed that the material is unsuitable for use in the top layer of a dike, but is still appropriate for use as core material.

Overall, the findings highlight that limited turning preserves tensile strength, while higher turning frequencies improve compactability. Under field conditions, however, the improved compactability also greatly benefits tensile strength, outweighing the structural instability caused by mechanical breakdown. Ripening also significantly reduces shrinkage potential, thereby decreasing crack formation behavior.

These insights suggest a higher turning frequency is the best method for managing dredged sediment, when only tensile strength and crack formation are concerned.

Contents

List of Figures

List of Tables

Nomenclature

Abbreviations

Abbreviation	Definition
ASTM	American Society for Testing and Materials
BTS	Brazilian Tensile Strength
CIAS	Crack Image Analysis Software
CIF	Crack Intensity Factor
COLE	Coefficient of Linear Extensibility
DM	Dredged Material
dw	dry weight
HIP	High Intensity Press
HPA	Hamburg Port Authority
ISRM	International Society for Rock Mechanics
LVDT	Linear variable differential transformer
METHA	Mechanical Treatment of Harbor Sediments
MKFP	Multi-chamber Filter Press
RH	Relative Humidity
S2S	Sediments to Soil
SEM	Scanning Electron Microscope
(S)OM	(Soil) Organic Matter
SP	Stockpile
TPBT	Three Point Bending Test
TS	Tensile Strength
UDTT	Uniaxial Direct Tensile Test
UCS	Uniaxial compressive strength
vdW	van der Waal

1

Introduction

The Netherlands, as a low-lying country, has always been highly vulnerable to high water levels and at risk of flooding. Approximately 26% of the country lies below sea-level, and around 60% is at risk of flooding events [32]. This threat is further aggravated by the fact that current climate models predict a sea level rise of around one meter for the Netherlands by 2100 [1], and a potential rise of up to three meters, due to uncertainties around the melting potential of Antarctica [6]. All of these factors combined mean that an investment of around 100 billion euros is required to make the country robust to the shifting climate environment [3]. Within this sum is the investment required to strengthen the country's dike system. As it stands, dike reinforcement alone will cost between 16 to 33 billion euros, which amounts to two thousand kilometers of dikes that need reinforcement by 2050 [61].

Traditionally, the material for dike construction and reinforcement is sourced at the location itself. This approach includes an investigation of the underlying soil for foundational stability, as well as its suitability for use in the dike itself [101].

This working method implies ample space and resources around the dike, which is not often the case in a dense country like the Netherlands. In fact, it's estimated that around 12-17 meters of additional horizontal space around the dike would be required for each meter that it is raised [102]. The material therefore needs to be brought from other locations. As the traditional marsh soil is a strained resource in Europe [68], the need for sustainable and alternative sources is growing increasingly urgent.

One potential source comes from the reuse of dredged sediments. Vast amounts of material are dredged in Europe to maintain a navigable depth in the continent's ports and waterways every year. The port of Rotterdam alone dredges up 12 -15 million cubic meters of material every year [47]. Initially, this material is not suitable to be used in construction, as it can have contamination levels above the regulatory thresholds, due to its proximity to anthropogenic activities. In order for it to be beneficially reused, it needs to be environmentally compliant with chemical guidelines, which limit the concentration of certain contaminants [16].

In the Netherlands, sediments are considered an integral part of the water system, and are therefore subject to regulation under the Water Act. The standards for sediment contamination are set out in a guidance document that itself is based on the Water Act [35]. To render dredged sediments suitable for reuse, its chemical, physical and biological properties can be modified through a process called soil ripening. An initial test was conducted in Hamburg starting in 2004, where dredged material was used as a cover layer over the core of a dike. This material was not ripened, and after 8 years, the dike cover was excavated and the results of the experiment were analyzed. Large shrinkage cracks were observed to have developed, which led to a large increase in the hydraulic conductivity of the cover. These cracks were attributed to primary shrinking of the material after it had been put in place. This led to the recommendation that soil ripening should be a necessary step in the pre-treatment of the material [29]. Although the cause of the crack formation was identified, the effectivity of the soil ripening process has yet to be fully investigated, and the resulting soil has yet to be proven viable for use in dike construction and reinforcement.

The Sediments to Soil (S2S) project [28], was founded with the intent of closing these gaps in knowledge. This thesis took place within the project, investigating the evolution of key geotechnical properties during the ripening process, given different stockpiling techniques. The properties of interest include soil tensile strength, shrinkage, crack formation and the Atterberg limits.

1.1. Research Questions

The thesis aims to investigate the effect of soil ripening and stockpile management on the physical and mechanical properties of the soil, to then determine whether this process can be optimized. This in turn, feeds back into the suitability of using the material in dike construction. A suite of experiments have already been conducted for the S2S project, focusing on the three different properties of the soil: chemical, biological and physical. They are all interrelated, and undergo changes under ripening [73]. Physical ripening in particular was investigated in this thesis, which also includes the mechanical properties of the soil. The physical properties, or properties inherent to the soil (particle size distribution, water holding capacity, etc), are already part of the larger suite of investigation in the S2S project. Soil mechanical properties, or how the soil reacts to an external force (tensile strength, shrinking), was investigated in this thesis.

Soil crack formation is related to its tensile strength [54], but this relationship has been the subject of few studies [55]. As such, it is of great interest to the project to have direct data on the METHA sample's tensile strength and crack formation capacity. This motivates research question 1(RQ1):

1. How does soil tensile strength and crack formation evolve during the ripening procedure?

The effect of ripening over stockpiling is not the only factor of interest for the project, as different stockpiling techniques were also investigated, which are expected to influence the ripening rate and the soil properties. Specifically, it is of interest to examine how these techniques affect both the tensile strength and the crack formation capacity of the soil (RQ2):

2. How do different stockpile management procedures affect crack formation and tensile strength of the material?

Both of these research questions should lead to a good understanding of the soil properties, which will serve as input for the next research question (RQ3):

3. Are the ripened METHA material physical properties sufficiently evolved for use in dike construction?

1.2. Hypotheses

Before any experiment was conducted, hypothesis for these research questions were developed,based on previous experiments and articles. The expected outcomes for each research questions is presented below:

1. The initial hypothesis is that soil tensile strength will increase during ripening, and will therefore be less susceptible to crack formation. This is because under physical ripening, the sediment's bulk density increases, meaning a tighter organization of the soil particles and smaller pore sizes. Both of these factors mean a more stable structure, and therefore higher tensile strength [113]. The soil's water content fluctuates while stockpiled, from the exposure to the environment (rainfall, evaporation) and physical processes (consolidation). This means repeated wet-dry cycles, which re-orient the soil particles and aggregates them, also leading to an increased tensile strength [36].
2. The different management procedures are mainly varying stockpile turning rates, which affect the aeration. An increase in oxygen availability leads to a higher organic matter degradation [4], this is expected to influence the tensile strength and shrinking behavior of the soil. The exact influence is hard to predict, as studies have not found a consistent relationship between organic matter, organic matter degradation, and soil mechanical properties [31], [77], [83]. The other difference between stockpiles is the control on vegetation growth. Its presence should also yield a higher tensile strength, as vegetation enhances desiccation through transpiration, and contributes to soil

structure formation due to rootage [27]. The last process that should affect the soil is the turning rate. As soils are stressed (which can occur from the heavy machinery required to turn it), they are rearranged into a denser state, leading to an increase in their strength [36].

3. Elaborating a hypothesis for this question is challenging, as part of it is defining the criteria for assessing whether or not the material is suitable for dike construction. This question will in part be answered by looking at the relevant literature on dike construction, as well as testing for the shrinkage and the Atterberg limits on top of the tensile strength and crack formation. Based on previous studies [29], it is expected that the material can be used in the core of dikes.

1.3. Thesis Outline

This thesis is structured in five parts, organized in order to present a cohesive research and story. Chapter 2 presents theoretical concepts behind tensile strength, soil crack formation, the ripening process, and the utilization of clay in dikes, through a literature review.

The methodology used to answer the research questions is discussed in Chapter 3. First, a description of the METHA material is given. Then, the Brazilian splitting method - used to measure tensile strength - is explained. This is followed by a description of the desiccation experiments that were conducted to assess the crack formation behavior of the soil. Finally, the Coefficient of Linear Extensibility (COLE) and Atterberg limits tests are explained, which characterize the material.

Chapter 4 presents all of the experimental findings. This is followed by a discussion in Chapter 5 on the processes that explain them, and what they mean for the potential reuse of dredged material in dikes. Finally, in chapter 6, the findings are summarized and recommendations for future research are given.

2

Theoretical Background

For this thesis, four principal research topics are defined: Soil tensile strength, soil crack formation, sediment ripening, and the application of different materials in dike construction. It is important to understand the processes and factors affecting these properties, so as to support the results obtained in the lab.

2.1. Soil Tensile Strength

Strength is defined as a materials ability to resist an applied stress without yielding or failing [98]. Tensile strength in particular refers to stress caused by a pulling force. It is a relevant property for many engineering applications. The agricultural industry, for example, is interested in how tensile strength affects a soil's mechanical stability, for effective crop production [2]. In hydraulic engineering, soil tensile strength is a major factor controlling an earthen structure's propensity to crack under desiccation or extreme loading conditions [50].

2.1.1. Theory Behind Tensile Strength

Tensile strength in soils is regulated by interparticle interactions, namely, the van der Waals attraction, the electrical double layer repulsion/attraction, and the capillary forces from the pore water pressure [60].

The van der Waals (vdW) forces are the foundation for all other interactions. Explaining the theory behind them is beyond the scope of this thesis, as they originate in the quantum mechanical realm. Their effect, however, can be briefly explained as an attractive or repulsive force between particles, that can also align and reorient them [42]. The strength of the vdW forces is dependent on the distance between atoms, their size, and their electronic polarizability [42]. Figure 2.1 illustrates how these interactions take place.

The electrical double layer occurs on a larger scale and deals with the interaction between particles when a fluid is present. It arises from the electrostatic attraction/repulsion forces between the charged surface of a particle, and the ions present in the fluid. In short, the ions with opposite charge stick to the surface of the charged particle, in a region called the Stern layer. Surrounding this is the Diffuse layer, which includes the ions that are around the particle, but not attached to the surface. Oppositely charged ions are attracted to the particle, while similarly charged ions are repelled. This leads to an ion density gradient, which decreases with distance. Eventually, homogeneity is achieved again, at which point the double layer ends, and the fluid goes back to electroneutrality. A schematic representation of the phenomenon can be seen in Figure 2.2.

Clay particles typically have a negative charge [75]. As a result, when two clay particles interact, there is a repulsive force between their double layers. This repulsion dominates only until the two particles are forced close enough that the van der Waals forces can come into effect, at which point they aggregate.

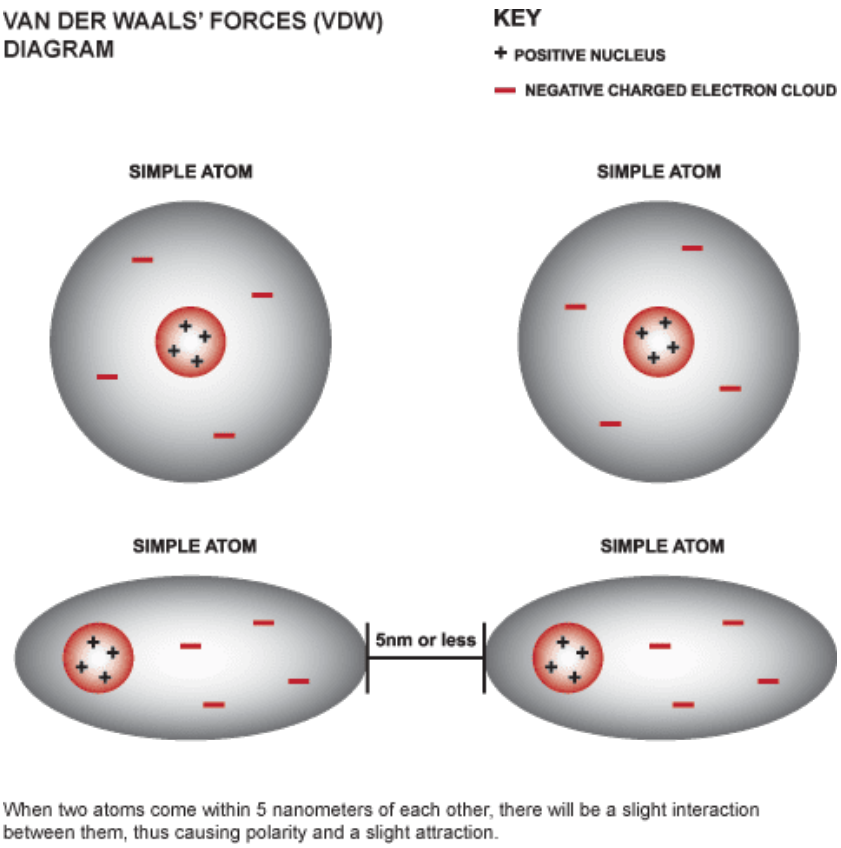

Figure 2.1: Diagram of the van der Waals forces, as molecules attract/repel each other based on their electron clouds [76].

The theory describing the force between particles as the sum of the van der Waals forces and the double layer is called the DLVO theory [48].

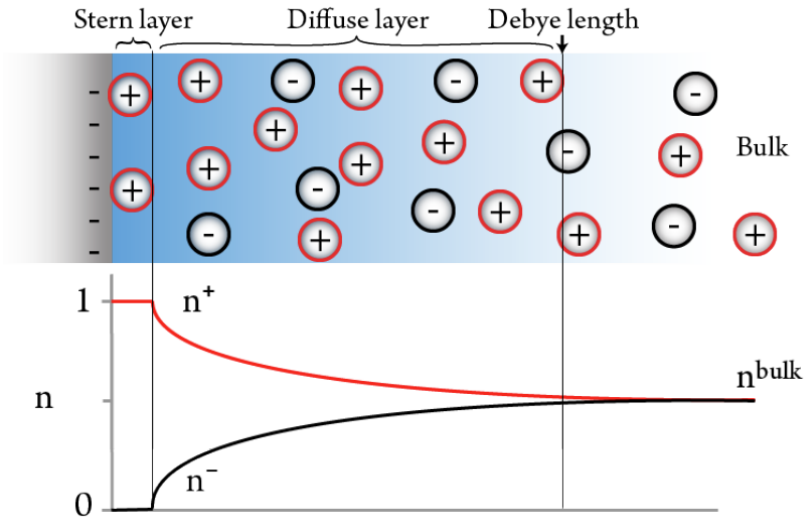

Figure 2.2: Diagram of a negatively charged surface, the Stern layer, and the Diffuse Layer. The Debye length marks the point at which the double layer ends. Underneath is a graph showing the density of the differently charged ions [48].

The capillary forces do not originate from interparticle interactions. Instead, they are caused by the presence of liquid bridges between them. The liquid bridges exert a force through a combination of the liquid cohesion and the adhesion between the liquid and solid phases. Again, the underlying physics

are beyond the scope of this thesis, but it is important to note that the capillary forces are dependent on the average size of the soil particles, the pore size and its saturation. Smaller particles, and therefore smaller pore sizes lead to a higher capillary pressure. Saturation plays a more complicated role, but in general, capillary pressure trends to zero at a fully saturated state [43]. This phenomenon is discussed in more detail in chapter 2.3.1.

Soil tensile strength is therefore linked to it's matric suction, which is closely related to the capillary pressure. Suction is defined as the difference between pore air pressure and pore water (capillary) pressure. Under unsaturated conditions, pore air pressure is typically equal to atmospheric pressure and can be neglected, capillary pressure is then equivalent to the matric suction [24].

2.1.2. Soil Properties Affecting Tensile Strength

There are many factors influencing tensile strength, but the most important ones are: water content [92], level of compaction (or dry density) [92], organic matter (OM) content [12], and clay content [12]. These factors are of course related; a higher clay content is generally considered to be a positive factor in stabilizing organic matter, for example. Although this view has been put into question - as it has also been observed to accelerate OM degradation in some cases [111] - it still exemplifies the complex relationship between both properties. There are even more factors that can influence tensile strength [40], but they are not investigated for this thesis.

All of these properties are directly related to the cohesiveness of the soil. Cohesion is the measure of a soil's particles tendency to stick together, or in simpler terms, the internal strength of the soil.

Several studies have demonstrated a direct correlation between organic matter content and an increase in soil tensile strength [69], [78], [12]. This relationship follows from the role organic matter plays in soils; it bridges mineral particles, and neutralizes surface charges, thereby enhancing the attractive forces discussed in section 2.1.1 [53]. Consequently, OM degradation is an important factor to monitor while soil conditions change, as it leads to a decrease in OM and therefore a lower soil strength [114].

Zhang [117] did find an inverse relationship between soil organic matter and tensile strength, but this can be attributed to the fact that in the study, porosity increased with OM content. A higher porosity means less interactions between particles, and therefore a lower tensile strength.

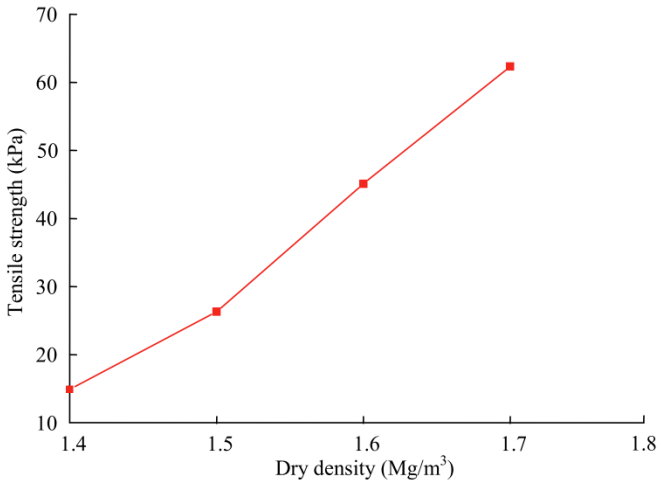

Figure 2.3: Effect of dry density on tensile strength of a silty clay loam [57].

Figure 2.3 illustrates the strong influence of dry density on soil tensile strength. This relationship is logical, as higher densities corresponds with more particle-particle interactions taking place, enhancing soil tensile strength. Indeed, this relationship has been observed in many studies [106], [92], [72], [57].

Such a direct relationship is not observed between water content and tensile strength. It is generally assumed that increasing water content leads to a decrease in tensile strength, as the capillary forces

weaken with increased saturation. However, at very low soil moisture, an initial increase in water content leads to a higher suction, due to the higher amount of water bridges that form as the sample leaves a fully dried state [92] (”Dry side” in Figure 2.4). Eventually, the sample reaches a moisture content (”Wet side” in Figure 2.4) at which the capillary forces start to decrease. This is due to the dissolution of aggregates, capillary bridges disappearing as the sample reaches the funicular state [82], and decreasing cohesion between clay particles. Increased bulk density moves the point with the highest tensile strength towards lower water contents.

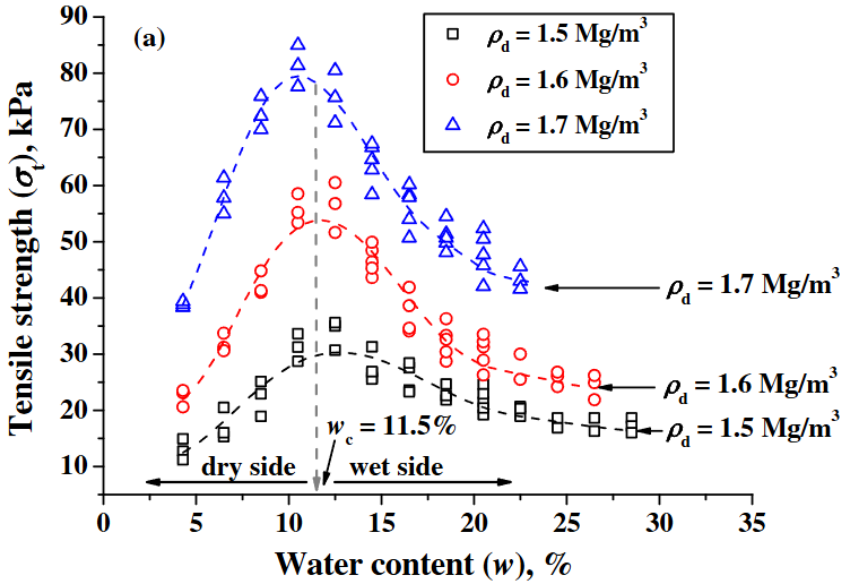

Figure 2.4: Tensile strength of a silt loam as a function of water content, at different dry densities. Two tensile strength regimes are observed, on the dry side and on the wet side [92].

Finally, a relationship between tensile strength and clay content exists. As briefly mentioned earlier, clay content indirectly influences tensile strength through its effect on SOM degradation. It also directly increases tensile strength, due to an increase in particle-particle interactions. Clay particles fill the space between larger particles in the soil matrix due to their very small size (< 2μm) . This creates clay bridges between the larger particles. The higher clay content also increases the cohesion of the matrix, which is explained by the clay's negative surface charge and particle attraction (section 2.1.1). This relationship has been observed experimentally [7].

2.2. Different Methods for Measuring Tensile Strength

The three most common methods for obtaining tensile strength of soils are the Brazilian disc splitting method, the Uniaxial Direct Tensile Test (UDTT), and the Bending Test [107]. They can be divided into direct and indirect methods. UDTT is a direct method, while TPBT and the Brazilian method are indirect. The Brazilian method is discussed in chapter 3.2. The other two methods are briefly discussed here.

2.2.1. Uniaxial Direct Tensile Test (UDTT)

The UDTT is a direct way to measure the tensile strength of a soil, and its standard is defined by the ISRM [10]. It involves clamping a sample at two points, usually with holders, and applying a tensile load at a constant displacement rate. The geometry of the test is designed so that the tensile load is transmitted through the central axis, without bending or torsional stress. This is the simplest test in theory, as tensile strength is then directly measured as:

$$\sigma_t = \frac{P}{A} \cdot 1000 \tag{2.1}$$

Where P is the tensile load in N, and A is cross-sectional area where the crack occurred in mm^2.

However, the simplicity of the test is mostly theoretical, as it is difficult to ensure that the fracture happens in the middle of the specimen. Additionally, it requires a large amount of material and is time-consuming.

2.2.2. Bending Test

An alternative method is the Bending test, which is most often employed with three or four bending points. The Three Point Bending Test (TPBT) is the most common configuration. It consists of a rectangular specimen, placed on top of two support points, and subjected to a downward force applied at the midpoint. This loading arrangement induces a tensile stress in the face opposite to the load, while a compressive stress happens at the load point [63]. The load geometry is shown in Figure 2.5.

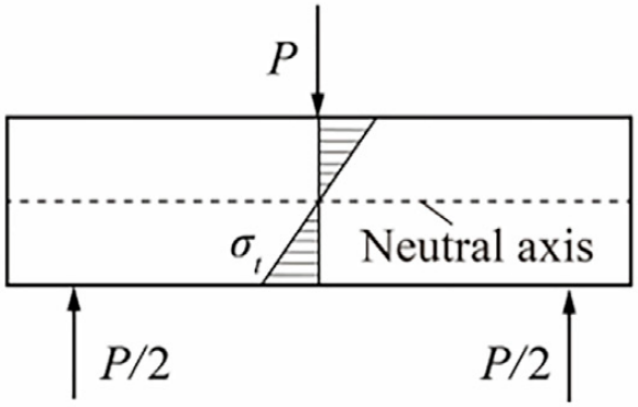

Figure 2.5: Load geometry for the TPBT, showing tensile stresses at the lower specimen face [107].

The compressive force is measured, and the corresponding tensile strength is determined with equation 2.2.

$$\sigma_t = \frac{3P \cdot l}{2bt^2} \cdot 1000 \tag{2.2}$$

Where P is the compressive load at failure in N, l is the distance between the two supporting points in mm, b is the width of the sample in mm, and t is the thickness in mm.

Although more reliable, this method still suffers from a large material requirement and is again time-consuming.

2.3. Soil Crack Formation

Crack initiation in a soil occurs when the stress caused by desiccation is equal to the soil's tensile strength [50]. As cracking progresses, tensile stresses caused by matric suction play a smaller role, and the process is then controlled by shearing stresses [62]. In addition, there are boundary conditions that affect crack formation in soils, such as the desiccation rate, initial moisture content, and the properties and geometry of the test container the soil is placed in. These are discussed in the following sections.

2.3.1. Theory Behind Crack Formation

As a saturated soil dries, water-air menisci form between the grains, which is the driver behind capillary forces. This forces the soil particles to rearrange, observed as soil shrinkage. Eventually, the tensile stress caused by capillarity can no longer be accommodated by soil shrinkage, and the soil cracks [115]. This is further aggravated by the boundary condition imposed by the surface the soil rests on - the rougher it is, the larger its constraint on soil movement from higher interfacial frictional forces [115]. A schematic overview of the process is shown in Figure 2.6.

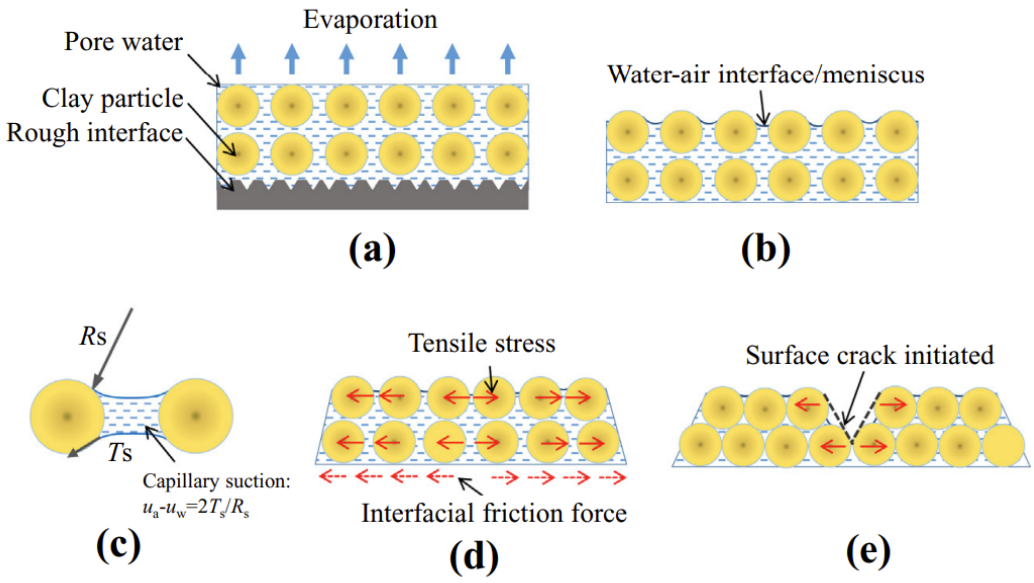

Figure 2.6: Schematic overview of the crack initiation process on soils [115].

An equation for capillary suction is written in Figure 2.6. This is equation 2.3.

$$s = \frac{2T_s}{R_s} \tag{2.3}$$

Where s is the capillary suction in Pa, T_s is the pore water surface tension, in N/m and R_s is the radius of the meniscus in meters. It follows from equation 2.3 and Figure 2.6 that drying increases suction. This can be attributed to a decrease in the meniscus radius (R_s), caused by the reduced amount of water in the pores, and the increased proximity of the particles from the soil shrinkage.

The increased stress at the crack tip (Figure 2.6e), causes the crack to propagate downward, until it reaches the lower surface boundary. This new water-air surface is the focus of the next crack, as tensile stresses perpendicular to the first crack are the highest [62]. Thus, secondary cracks tend to form perpendicular to primary cracks (also seen in Figure 2.11). Eventually, this propagation pattern stabilizes, as drying increases suction (and therefore tensile strength) enough to stop the formation of new cracks. In this stabilized regime, the only process observed is an increase in crack width, caused by further shrinkage of the clods due to moisture loss [70].

This is the process observed in laboratory crack formation tests, where soil thickness is relatively small, and cracks always propagate until the bottom of the container. In field conditions, however, crack propagation does not have a thickness limit. Once cracking reaches a certain depth and later stage of desiccation, the controlling soil property shifts from tensile strength to shear strength. This is due to the fact that gravity stress increases with depth. Eventually, the gravitational forces acting across the crack faces become greater than the matric suction [62], leading to shear failure propagation. This is

the motivation for also considering soil shear strength in crack formation analyses, although this was not investigated in this thesis.

In laboratory experiments, soil crack formation is largely dependent on sample preparation and the boundaries imposed on it. The following sections will investigate the possible external parameters that affect crack formation and propagation.

2.3.2. Factors Affecting Crack Formation: Sample Container

The sample container influences the final cracking pattern due to the different possibilities for its friction coefficient (figure 2.6d). Additionally, different geometries can affect the final result, specifically from the resulting container surface areas. The molds is also the easiest parameter to control, as it can be reused between tests, and its manufacturing is easy to reproduce. A variety of different materials have been used in studies of crack formation, with an overview shown in table 2.1.

Table 2.1: Overview of container materials and crack formations studies that used them.

Material	Studies Where it is used
Wood	Tollenaar,2017 [100], Lakshmikantha,2009 [54],Corte and Higashi, 1964 [14]
Plastic	Tollenaar, 2017 [100], Lakshmikantha, 2009 [54]
Metal	Huang et al., 2019 [38], Tollenaar, 2017 [100]
Teflon	Peron et al., 2009 [70], Sawada et al., 2021 [81]
(Plexi)glass	Zhang, 2020 [118], Corte and Higashi, 1964 [14], Costa et al., 2013 [15]

Tollenaar [100] tracked cracking of a soil when subjected to different bottom surfaces (Metal, plastic and wood) wherein each material displayed different cracking intensity and patterns. The study confirmed that materials with lower friction show a lower rate of cracking. Specifically, it was found that the wooden material produced a higher number of cracks, followed by plastic and then metal. This aligns with their respective surface friction properties. Peron et al. [70] further strengthened this idea by conducting experiments with Teflon bottom surfaces, which have even lower friction coefficients. The free desiccation tests (provided by the presence of the Teflon layer) saw a noticeable decrease in crack formation, when compared to similar constrained tests.

Additionally, the geometry of the sample containers is not consistent between studies. Laboratory crack formation studies are typically conducted with circular containers, and as a result few studies have been conducted on the effect of container shape on the cracking behavior.

Lakshmikantha, Prat, and Ledesma [56] found that the total surface area directly impacts crack formation, due to the different desiccation rates it provokes. Crack intensity factor was observed to increase with surface area. Furthermore, for rectangular containers, changing the thickness to width ratio significantly impacts the type of cracking observed. Wang et al. [108] found that containers with a high relative ratio present a parallel cracking pattern, enabling cracking characterization based on the distance between cracks. As the height to width ratio decreases, the type of cracking gradually shifts to a networked pattern.

2.3.3. Factors Affecting Crack Formation: Desiccation Rate

Desiccation rate - the driving force behind soil cracking (Figure 2.6) - is mostly controlled by the environmental conditions that the sample dries under. Specifically, temperature and the relative humidity influence evaporation, but in opposite ways: a higher temperature leads to more evaporation, while a higher relative humidity reduces the evaporation rate.

Early studies on soil cracking already observed a pattern between desiccation rate and water content at cracking. This can be seen in Figure 2.7

The effect that these different rates have on cracking, however, is ambiguous. Studies have been conducted on replicate samples with temperature as the primary variable, but results have been incon-

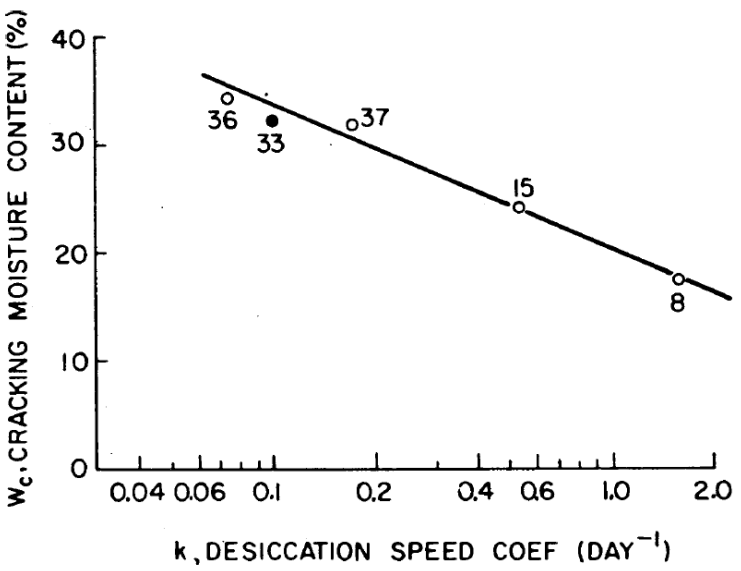

Figure 2.7: Cracking moisture content and desiccation speed coefficient [14]

sistent. Tang et al. [94] found that there is a trend for increased crack length and width with increased temperature, while Painuli et al. [67] found a decrease in crack width with increasing temperature.

It should be noted that the tests, although focused on changing temperatures, had different set-ups - most importantly different sample materials - which influenced their final results. It is also important to point out that these differences were mostly seen in higher temperatures, with the tests realized under ambient temperature conditions seeing small differences in cracking behavior [67].

2.3.4. Factors Affecting Crack Formation: Wet-Dry Cycles

The extended exposure time of the stockpiled material under different climatic conditions means it has endured several wetting-drying cycles. In soils, these changes in saturation have been observed to destroy soil structure, caused by the entrapment of pore air. Large air bubbles accumulate in the coarser pores, and exert internal air pressure larger than the binding strength of the surrounding grains. The elevated pressure causes the damage in the soil structure [20]. The destruction is aggravated by the fact that re-hydrating the sample weakens the binding strength of the grains, reducing the resistance to the elevated air pressure [91].

Figure 2.8 demonstrates clearly the effects of successive wetting-drying cycles. Clod disintegration is already apparent in the first two cycles as clod size is noticeably different between Figures 2.8a and 2.8b. This destruction of soil structure is a result of the process described above, and has been found to be irreversible [91]. Subsequent cycles reach an equilibrium state, as differences between Figures 2.8b, 2.8c, 2.8d, and 2.8e are minimal. Wetting and drying these samples does lead to destruction of soil structure, but unlike the first two cycles, this was found to be reversible [91].

The findings from Tang et al. [91] suggest that a material stockpiled for an extended period of time will - after the first few cycles - have reached a state where successive wetting-drying cycles do not greatly influence soil structure.

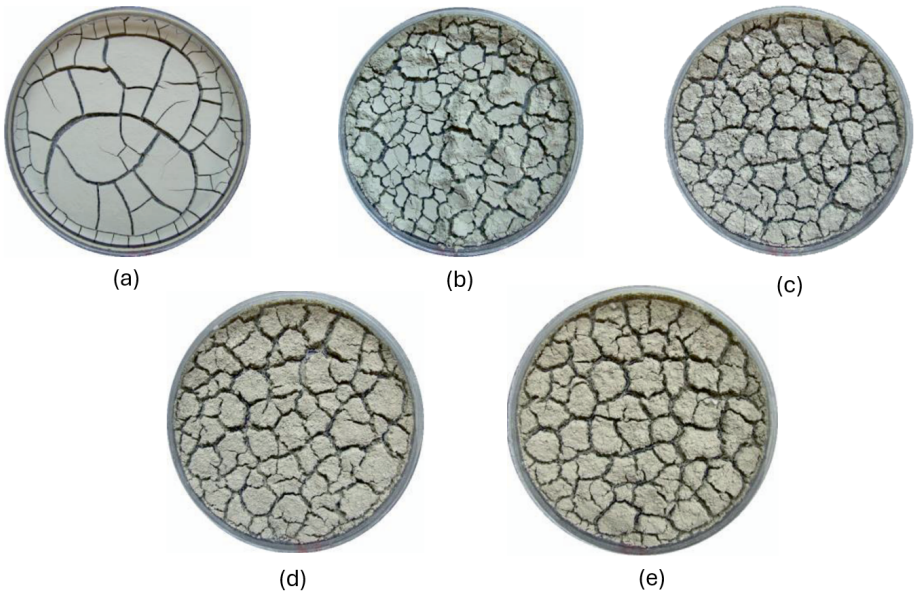

Figure 2.8: Differences in dessication cracks after successive wet-drying cycles. Images after first (a), second (b), third (c), fourth (d), and fifth (e) wetting-drying cycle. Irreversible damage to the soil structure is observed after the first two cycles, with subsequent cycles showing reversible changes. Adapted from Tang et al. (2016) [91].

2.3.5. Factors Affecting Crack Formation: Initial Moisture Content

The relationship between cracking behavior and the initial water content of the sample is often overlooked, and only a few studies have addressed it in detail. Moisture loss is the driving force behind crack initiation (figure 2.6), but it is assumed that as long as the sample is originally saturated, the initial water content is not relevant. Tang et al. [90] suggests a minimum initial water content of 1.5 times the liquid limit. Such a water content allows for complete saturation and dispersion of soil particles [91]. However, a water content above that is not investigated, as crack initiation only happens once a critical moisture is reached, independent of the starting moisture.

The findings from Tollenaar [100] indicate that varying initial water contents has an influence on the final crack formation pattern. Tests were conducted on replicate samples, with initial water content as the only variable. The results showed that a lower initial water content (but still above 1.5 times the liquid limit) led to smaller and fewer cracks at the end of the desiccation process [100]. This indicates maintaining a consistent initial water content for all samples is essential for replicability of the results.

2.3.6. Factors Affecting Crack Formation: Sample Thickness

The water flow rate and heat transfer in a sample are directly affected by a changing thickness [112], which in turn affects crack formation. A larger thickness, for example, means a noticeable moisture gradient evolves in the sample; this heterogeneous condition leads to different shrinkage rates within the sample. Moreover, thickness directly impacts the tensile resistance of the soil, as described in equation 2.4 [115].

$$\sigma = \frac{f \cdot L}{d} \tag{2.4}$$

Where σ is the tension stress in the soil, f is the frictional stress, L is the contact length with the container and d is the soil thickness. An increase in the thickness (d) leads to a decreased stress (σ) in the soil, which is the driving force behind the cracking. Therefore achieving a sufficient stress state for cracking is harder with an increasing thickness.

Figure 2.9 presents the influence of thickness on clod size. In the critical state (when crack formation

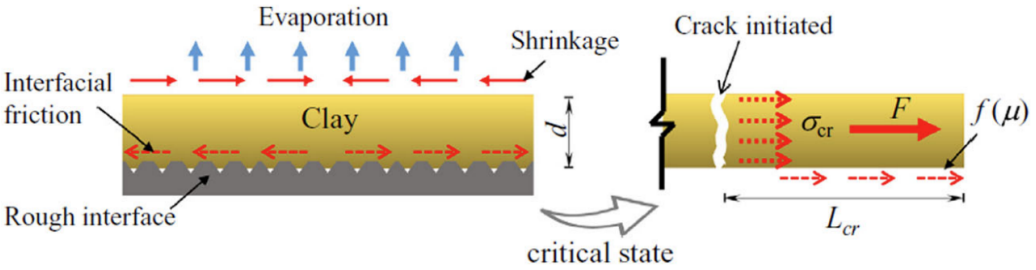

Figure 2.9: Schematic overview of the stress state of soil cracking under the influence of interfacial friction and soil layer thickness. Lcr = Critical contact length, equivalent to the clod size after fracturing. σ_{cr} = critical tensile strength of the soil. [115].

occurs), L in equation 2.4 is equivalent to the clod size (L_{cr} in Figure 2.9), while σ_{cr} represents the critical stress, equivalent to the tensile strength. Given that the 'L/d' ratio is the same for a constant tensile strain, clod size will increase with thickness. This conclusion assumes that the tensile stress is uniformly distributed over the soils, which can only be assumed for thin layers [115].

In essence, this means that a larger soil thickness leads to fewer, wider cracks, and bigger clods[100]. In order to eliminate this influence on experimental results, thickness needs to be constant between replicates. This can be achieved by trimming the samples at the container height.

2.4. Sediment Ripening

A large volume of material is dredged every year from ports across Europe. It is an essential part of their maintenance process, as it ensures navigable depth for maritime traffic in the port. In Hamburg, for example, around 4 million cubic meters of sediments were dredged in 2023 [33]. For a small part of the material that is dredged, concentrations of certain contaminants exceed regulatory thresholds, precluding the material's relocation in the water body. In Hamburg, they go to mono-landfills for dredged materials, after processing in the METHA plant. The most common practice however, is to dispose of them in temporary upland sites, a convenient and economic method. This disposal method transforms the material from contaminated waste into potentially useful soil, that can be used for any number of purposes. Common applications include the construction industry and landfill coverings [86], provided they meet legal standards. The process through which this happens is called ripening, named after cheese ripening, where soft milk curds are turned into cheese after being forcefully de-watered. The cheese then continues to lose water through evaporation [103], similar to the sediments.

A diagram of the processes that occur in sediment ripening is shown in Figure 2.10.

Upon extraction, dredged material typically has a water content over 70 percent of its total weight [105]. The METHA plant, however, mechanically de-waters the sediment, resulting in a material output with a water content around 50% by dry weight (dw). The de-watering process consists of physically pressing out the water, and is explained better in section 3.1.

Flocculation, sedimentation, and consolidation occur in the early stage, when the material is first dredged and flushed into de-watering basins, before they undergo any physical treatment. Flocculation is a natural process of suspended fine materials. Particles aggregate, and form larger structures, at which point their gravitational weight is stronger than the Brownian motion suspending them, and they settle. The theory behind these forces was briefly explained in section 2.1.1. Flocculation and primary consolidation allows the supernatant water to be discharged, as most of the sediments are no longer suspended. This is followed by a secondary compression regime, wherein the particles rearrange themselves into a tighter structure. This manifests as the settled layer thickness decreasing. This is again moved by gravitational forces, as the self-weight of the particles and the overlying sediment drives the structure down. The result is a volume decrease, which is accommodated by forcefully pushing out the sediment pore water [96].

Ripening only starts after the sediments go through these initial processes. It can be divided into physical, chemical and biological ripening, which are categorized separately, but influence each other

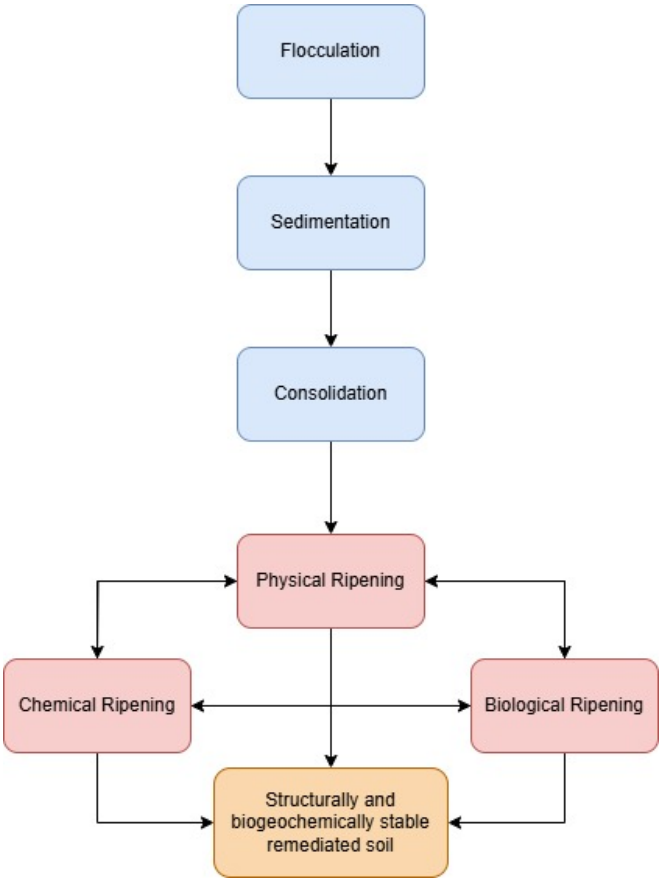

Figure 2.10: Processes that occur during sediment stockpiling, transformimg sediments into stable soils [105][27].

and occur simultaneously. Physical ripening, however, is the driving force behind all three [105]. It is the process through which bulk density increases and soil structure forms. Ripening is caused by desiccation, which in turn leads to shrinkage, and an increase in permeability caused the formation of cracks [74]. These cracks are the driver behind increased evaporation, and a further decrease in water content. This in turn, creates secondary horizontal cracks and tertiary vertical cracks, as shown in Figure 2.11.

A key observation from the figure is that cracks increase as ripening progresses. This is logical, as the cracks induce air intrusion, which itself accelerates evaporation and leads to the formation of even more cracks, thus forming a self-reinforcing feedback loop. It should also be noted that the x-axis is not quantitative. This is because the time it takes to physically ripen a sediment depends on the initial water content and on management practices. In a climate like the Netherlands, it typically takes around two years to physically ripen a one meter thick layer of dredged sediment [34]. This is with aeration alone taking place, however, which is the slowest de-watering method.

The increased aeration caused by the cracks leads to the onset of chemical ripening. Primarily due to the oxidation of soil sections that were only stable under reduced conditions [74]. With the presence of oxygen, processes that lead to changes in composition of the soil solution [29], aerobic organic matter degradation, speciation of contaminants [30], and organic matter stabilization [109] take place.

This chemical stabilization is what renders the sediments safe to be reused. Sulfides are oxidized [30] and the disassociated minerals are re-bound in oxidic or carbonate minerals, potassium complexes form and precipitate - which improves the stability of the soil structure [105] - and organic contaminants can be degraded or stabilized through organo-mineral complexes [105]. However, in poorly buffered sediments, the oxidation of sulfides leads to a drop in pH and consequentially, mobilization of heavy metals, which has already been observed in dredged sediments [87]. The leachability does drop as the material dries [87], but care should still be taken during stockpiling to not contaminate the surrounding

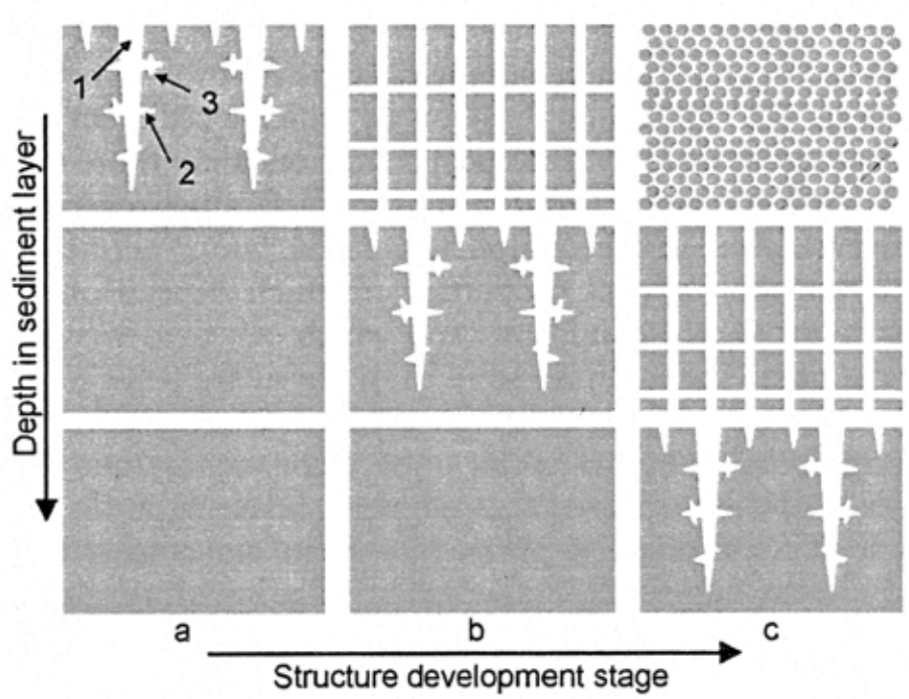

Figure 2.11: Geometry of cracks in a ripening stockpile, with different depth and times of ripening. Numbers 1,2, and 3 refer to primary, secondary, and tertiary cracks [105].

environment.

In addition to chemical processes, physical ripening also promotes biological ripening. This refers to any biological activity occurring in the material, including that from plants, animals or microorganisms. With the arrival of oxygen, aerobic bacteria can develop, which supports the degradation of aerobic organic matter. This activity, however, can be limited due to decreased moisture content as desiccation progresses [105]. Plant rootage and subsequent transpiration further aids de-watering of the sediment, while the presence of macro-fauna (mainly worms) leads to additional structure formations in the soil. All of this activity combined leads to the formation of more complex molecules, which stabilizes the soil, aids sequestration of carbon [104], and increases the contaminant retention potential of the material.

From these facts, it follows that in order to accelerate sediment ripening, efforts should be made to de-water the material before stockpiling (as implemented in the METHA plant), enhance aeration, and encourage vegetation growth in the material.

2.5. Dredged Materials and Clays in Dikes

The aim of this chapter is to present the possibility of using dredged material in dikes, and exemplify this with a previous case where dredged material was used in a test dike. Then the general use of clay in dikes is contextualized, and its required properties presented.

2.5.1. Dredged Materials in Dikes

The use of dredged material (DM) in dike construction has gained increased interest, as circularity efforts take the forefront of environmental policies [22]. In the port city of Bremen, for example, there is a standing directive to assess the availability of dredged material in any dike construction project, before other conventional materials are even considered [84].

A guidebook has been developed for the use of dredged materials in dikes (with a focus on German and Polish legislation), by the University of Rostock, in collaboration with Gdansk University of Technology [80]. It provides recommendations based on both the contamination level and physical properties of

the material.

The contamination level guidelines take into account the elevated concentration of certain pollutants that will potentially leach after application. These pollutants originate from the industrial and port waste characteristic of the original dredging site the material often comes from. The limiting concentrations are set out by Länderarbeitsgemeinschaft Abfall (LAGA), the German state working group on waste [52].

Additionally, the guidebook sets out geotechnical requirements for the material. These are presented in table 2.2.

Table 2.2: Overview of relevant geotechnical requirements for dredged material to be used in dikes. Adapted from Saathoff, Cantré, and Sikora [80]

Parameters	Limit
TOC (%)	≤ 9
Plasticity Index (%)	≥ 15
Liquidity Index (-)	≤ 0.3

Several large-scale applications of dredged materials in dikes have already been conducted, primarily in the rivers and coast of the south Baltic Sea. It was found to be a suitable building material, and its environmental impact was below the limits set by legislation. It should be noted that in these cases, the material was applied underneath a traditional marsh clay [80].

A pilot study was conducted on the METHA material, which is of particular relevance for this thesis [29]. In the study, dredged material was used as part of the cover layer for a dam along the river Elbe in Hamburg (see Figure 2.12). Adjacent to the experiment, a control dam was built with standard construction materials, specifically marsh soil in the cover.

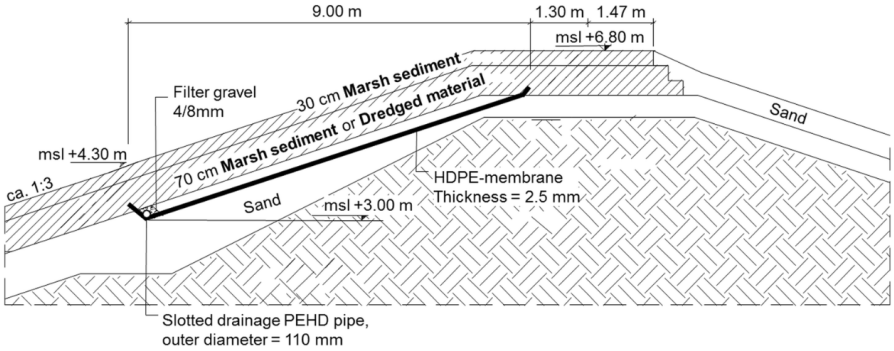

Figure 2.12: Schematic cross section of the test dike built with a dredged material cover [29]

After eight years, an excavation was carried out, and the dredged material showed significant differences with the control dike. The DM layer developed large cracks (greater than 1 centimeter width), whereas the control dike exhibited no cracking behavior (Figure 2.13). The formation of these cracks led to a higher hydraulic conductivity, and the onset of chemical and biological processes in the clay. This is attributed to the intrusion of air into the layer, which enabled aerobic processes to occur[29].

Figure 2.13: Profile view of the cover layer built with marsh sediments (left) and dredged materials (right)[29]

2.5.2. Clay in Dikes

Clays have been used in dikes for centuries. The the first dikes built in the Netherlands used them [97], due to the material's low permeability and high cohesiveness. These same properties are still what drives its use in modern day embankments, although with a more sophisticated structure. Modern dams generally consist of two functional structures: a top layer and a core. Clay is commonly used in both. In the top layer, its main function is to protect the core and limit permeability, whereas in the core, it is used for its shape retaining properties [95]. A schematic overview of this is seen in Figure 2.14.

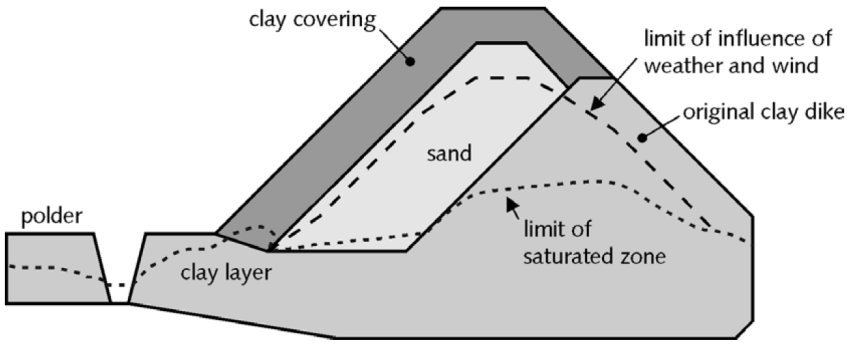

Figure 2.14: Dike profile showing a common pattern for saturation zone, and where weather conditions have significant influence [95].

Standards have been developed for the use of clay in dikes, in order to guarantee its ability to protect and support the structure. These standards are primarily concerned with the Atterberg limits and sand content of the clay. These properties determine a material's resistance to erosion. The reason erosion is such an important parameter is due to the primary function of the dike: They are built to contain water, which is a major erosive force. Additionally, dikes are made to endure extreme weather events, which include high water levels and wind speeds. Combined, this means a dike needs to be built so as to withstand highly erosive conditions. Given sufficient erosion-resistance, further standards are

recommended on the basis of organic matter content, salt content, chalk content, coloring and smell [95]. An overview of the requirements is provided in table 2.3.

Table 2.3: Overview of requirements for clays used in dikes. Adapted from Taw (1996) [95].

Erosion-Resistance Category	Liquid Limit (% dw)	Plasticity Index (% dw)	Sand Content (wt %)
1 - Erosion-resistant Clay	>45	>0.73 * (w_1 -20)	<40
2 - Moderately Erosion-resistant Clay	<45	>18	<40
3 - Clay with little erosion resistance	<0.73 * (w_1 -20)	<18	>40

With the additional requirements shown in table 2.4.

Table 2.4: Overview of additional requirements for all clays used in dikes. Adapted from Taw (1996) [95]

Parameter	Required Value
Organic Matter Content (% dw)	<5
Salt Content (NaCl g/l soil moisture)	<4
Water Content for Working (%)	Top Layer: $I_C \geq 0.75$ Core: $I_C \geq 0.60$

The requirement on the water content for working of the clay is based on the consistency index (I_C), which is a ratio describing the relationship between a clay's water content and its mechanical behavior. A higher I_C means a drier - and therefore firmer - clay. As a high rigidity is desirable in dike materials, a minimum consistency index value is given, which goes back to a maximum water content that needs to be maintained. Exceeding this moisture results in a cohesion insufficient for the clay to perform its function in the dike [95]. Different I_C thesholds have been defined based on the function of the clay. The standard for core materials require a lower I_C - which means a higher moisture content - than the top layer. This prevents negative suction pressure, and eventual drying and cracking of the top layer. This water content is usually 10 - 15% higher than the maximum water content given by the Proctor compaction test in clays [95].

Additionally, tensile strength is an important parameter to be investigated when assessing the suitability of a clay to be used in dikes. This is because of the prevalence of tensile cracks on earthen structures. The presence of these cracks lead to infiltration and erosion of the structure, and they are usually caused by a differential settlement of the structure, or friction forces between the core and the covering [88].

3

Materials and Methods

In this chapter, a description of the METHA material is given, followed by the different management techniques used to ripen it in the de-watering fields. Then, the methods used to test the tensile strength, crack formation, COLE, and Atterberg limits of the soil are described.

3.1. METHA Material

Around 4 million cubic meters of sediments were dredged by the Hamburg port authority in 2023[33]. This material undergoes separation at the port, and follows one of three main disposal routes: transfer to the North sea, transfer to the tidal Elbe or relocation to an upland facility. The vast majority of dredged sediments are relocated to another body of water, with only around 5% of them going to land treatment and disposal in 2020 [79]. That is still around 190 thousand tons in 2020, however - making it Hamburg's largest single waste stream. The deciding factor determining the relocation of the sediment is its contamination level. Ideally, sediments are relocated within the Elbe estuary or to the North Sea. However, if contamination exceeds regulatory thresholds, they must be transported to the METHA treatment plant, where they are de-watered and separated. The treated material is subsequently disposed of in mono-landfills [19].

No chemical or biological treatment is applied in the METHA plant. Instead, the materials are separated based on particle size and mechanically de-watered (Figure 3.1).

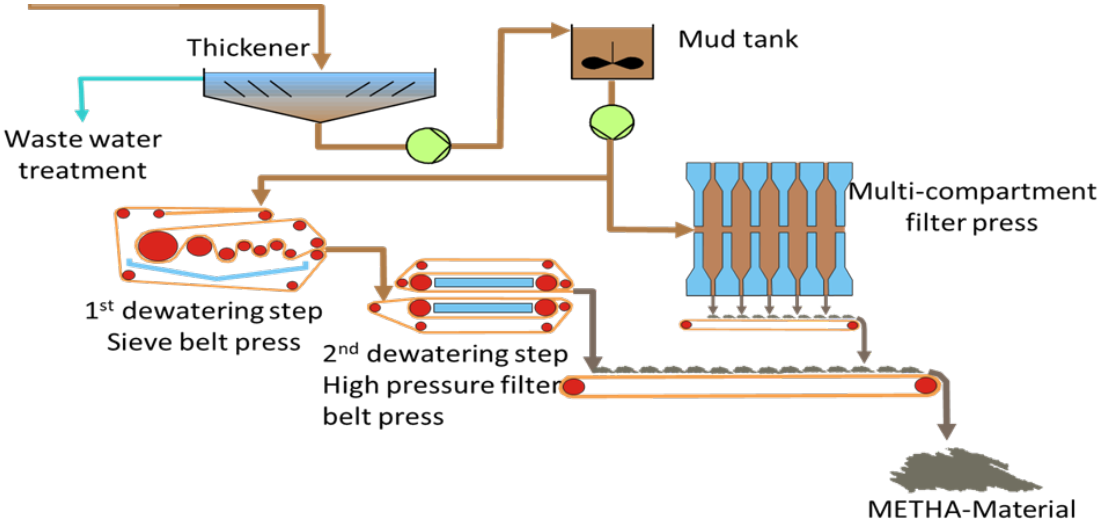

Figure 3.1: METHA plant de-watering procedure [18].

The process that takes place before Figure3.1 (Appendix E) separates the dredged sediment into four fractions: coarse material (>10mm), sand, fine sand, and the METHA material, which contains all the fine particles. Because smaller particles tend to be the most contaminated [37], the ripening stockpiles only contain the METHA material.

The particle size distribution for the METHA material is shown in table 3.1. Additionally, total organic carbon from the METHA material was measured at 3.0 wt %.

Table 3.1: Grain Size Distrubution of the METHA material.

Grain Size (μm)	%
0-20	46.70
20-63	33.70
63-100	13.17
100-200	4.40
200-630	1.4
630-1000	0.20
>1000	0.1

In order to research the ripening process in the METHA material, nine stockpiles were created (1000 - 2200 $m^{3)}$ in December 2022 nearby the METHA plant. Once there, the material undergoes chemical, biological and physical processes, wherein the alluvial mud can transition towards a consolidated soil. These processes were discussed in more detail in section 2.4.

Different stockpiling methods were implemented in the de-watering fields Moorburg-Ost, intended to investigate changing ripening time, and changes in the final material properties caused by each method. All of the stockpiles and their different management practices are listed in table 3.2, with stockpiles investigated in this thesis in **bold**.

Table 3.2: Stockpile management practices, investigated stockpiles in **bold**.

Stockpile	Material	Turning Events per year	Vegetation
SP-1	**HIP**	**2 times**	**Worked into stockpile**
SP-2	*HIP*	*None*	*No action*
SP-3	*HIP*	*4 times*	*Worked into stockpile*
SP-4	**HIP**	**Not turned**	**Allowed to grow**
SP-5	*HIP*	*4 times*	*Vegetation Removed before turning*
SP-6	**HIP**	**2 times**	**Vegetation Removed before turning**
SP-7	**HIP**	**4 times**	**Worked into stockpile**
SP-8	*MKFP*	*2 times*	*Worked into stockpile*
SP-9	**MKFP**	**4 times**	**Worked into stockpile**

SP-5 and SP-6 were originally intended to have the first 20 centimeters of rooting zone removed before each turning event so as to remove the influence of vegetation on the ripening process. However, it was observed after implementation that little to no rooting occurred in these stockpiles. As a result, only stockpile 4 (control) observed the effect of vegetation on ripening, while all other stockpiles saw no, or highly reduced, vegetation growth [26].

Sampling campaigns were planned twice a year, shortly before each turning event. One such campaign was carried out during this thesis, the March 2025 campaign. The campaign schedule can be seen in Appendix E.

Sampling consisted of collecting material from each stockpile at three different geographic points, with material taken from two depths (top and bottom) per location. This method was developed to ensure each sampling run was as representative as possible. Four out of the five stockpiles are from the High

Intensity Press (HIP) Material, while SP-9 was constructed out of material from the Multi-chamber Filter Press (MKFP), the treatment flow paths for each material can be seen in Figure 3.1.

The materials used in this thesis were collected in the last three sampling campaigns: Campaign 6 (March 2024), campaign 7 (September 2024), and campaign 8 (March 2025). These samples represent the later stage of ripening, two years after stockpiling. Additionally, samples from campaign 3 (June 2023) were later added, to represent samples at the early stage of ripening.

Figure 3.2: Sampling of one of the stockpiles

3.1.1. Sample Preparation

The samples were transported back to Delft in buckets. For each stockpile, two buckets were collected - one contained the samples from the bottom and another from the top of the stockpile - containing material from the three different sampling points. In the lab, each bucket was thoroughly mixed, to ensure homogeneity between the three sampling points. A portion from the top bucket and a portion from the bottom bucket of each stockpile was then collected and mixed again, producing a globally mixed sample. Afterwards, the moisture content of each stockpile was calculated (using equation 3.1), and then adjusted to 40% dry weight (dw), the target moisture content for the Brazilian tensile strength test. After allowing the samples to equilibrate in the fridge for a few days, they were sieved to four millimeters. This step was conducted to eliminate the effect of big clumps, as tests were conducted on small specimens.

$$W_c = \frac{W_W}{W_d} \cdot 100 \tag{3.1}$$

Where: W_c is the water content,W_W is the water weight, and W_d is the dry weight.

3.2. Brazilian Tensile Strength Test

Direct tensile strength methods, while inherently more reliable, are also more expensive. This is due to the complex procedure needed to prepare both the sample and the testing equipment [107]. The Brazilian tensile strength (BTS) test offers an efficient alternative for determining tensile strength of a material. This is accomplished through its smaller and therefore easier to handle samples, which allows for a large number of tests to be carried out in quick succession [17]. It should be noted that the test was originally developed for stronger materials, such as rock and concrete, but given certain

configurations (curved loading jaws, specific sample geometry), it has been proven suitable for use on soil samples [17].

The testing apparatus and methodology for analysis was developed in accordance with ASTM standard D3967−23 [5]. It consists of imposing a load on a cylindrical sample until tensile failure occurs. The loading distribution that leads to failure is shown in Figure 3.3.

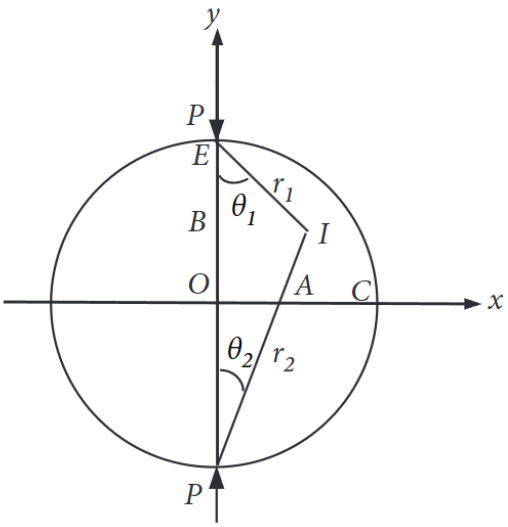

Figure 3.3: Force distribution under uniaxial load in the Brazilian splitting method [39]. Stress condition for a point I within the sample is derived in equations 3.2 - 3.4 and resulting stresses for points A,B,C,E, and O are described in table 3.3.

The stress at point *I* in Figure 3.3 can be divided into its normal components (σ_x and σ_y) and the perpendicular shear stress (τ_{xy}). The following equations can be derived from this geometry [39].

$$\sigma_x = \frac{2P}{\pi t}\left(\frac{\sin^2\theta_1 \cdot \cos\theta_1}{r_1} + \frac{\sin^2\theta_2 \cdot \cos\theta_2}{r_2}\right) - \frac{2P}{\pi dt} \tag{3.2}$$

$$\sigma_x = \frac{2P}{\pi t}\left(\frac{\cos^3\theta_1}{r_1} + \frac{\cos^3\theta_2}{r_2}\right) - \frac{2P}{\pi dt} \tag{3.3}$$

$$\tau_{xy} = \frac{2P}{\pi t}\left(\frac{\sin\theta_1 \cdot \cos^2\theta_1}{r_1} + \frac{\sin\theta_2 \cdot \cos^2\theta_2}{r_2}\right) \tag{3.4}$$

Filling in values for r_1, r_2, and θ for the different points labeled in Figure 3.3 leads to the stresses presented in table 3.3.

Table 3.3: Stress values at positions described in figure 3.3 (adapted from Huang et al. [39])

Position	Stress in the x direction (σ_x)	Stress in the y direction (σ_y)
A	$-(0.72P/\pi dt)$	$3.12P/\pi dt$
B	$-(2P/\pi dt)$	$8.66P/\pi dt$
C	0	0
E	$-(2P/\pi dt)$	Load Point
O	$-(2P/\pi dt)$	$6P/\pi dt$

Table 3.3, shows that the largest stresses occur in the compression regime (σ_y). All of the forces in the x direction (σ_x) show tensile stress. Because a material is generally weaker in tension than in

compression, failure will occur in the x direction (σ_x). Therefore, the peak stress observed in the sample at failure corresponds to the tensile strength of the material. This is equivalent to the stress observed in the midline of the sample, and described in equation 3.5.

$$\sigma_t = \frac{2 \cdot P_c}{\pi \cdot d \cdot t} \tag{3.5}$$

Where σ_t is the Brazilian tensile strength of the sample, P_c is the maximal load applied to the sample when failure occurs, d is the diameter of the sample, and t is the thickness of the sample.

The equipment developed to achieve the stress described in equation 3.5 consists of loading plates, a linear variable differential transformer (LVDT), a load cell, and an uniaxial compressive strength (UCS) loading frame. The frame controls the applied load, while the load cell measures it and the LVDT measures displacement. The loading plates can be arranged in different configurations (figure 3.4), which affect the boundary conditions, but always comply with the theory behind equation 3.5. In fact, all of these different loading configurations give almost identical strain results in the midline of the sample [51].

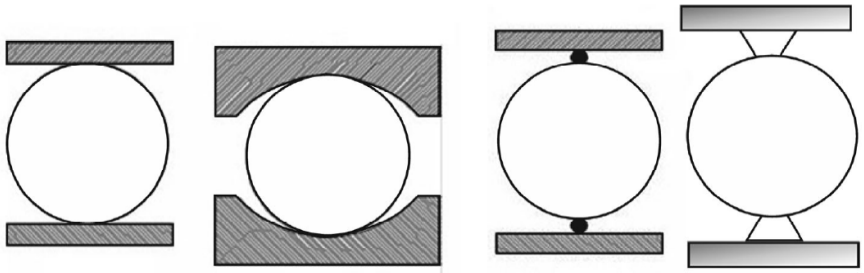

Figure 3.4: Different loading schemes for the Brazilian split method [21]

The configuration used in this thesis (Figure 3.5) follows the international standard given by the ISRM [11]. The resulting failure from loading should have the pattern shown in Figure 3.5 in order to be valid, that is, a break confined to roughly the midline of the sample. Any other fracture pattern - likely coming from sample heterogeneity - breaks the assumption in equation 3.5, and is not the result of tensile failure.

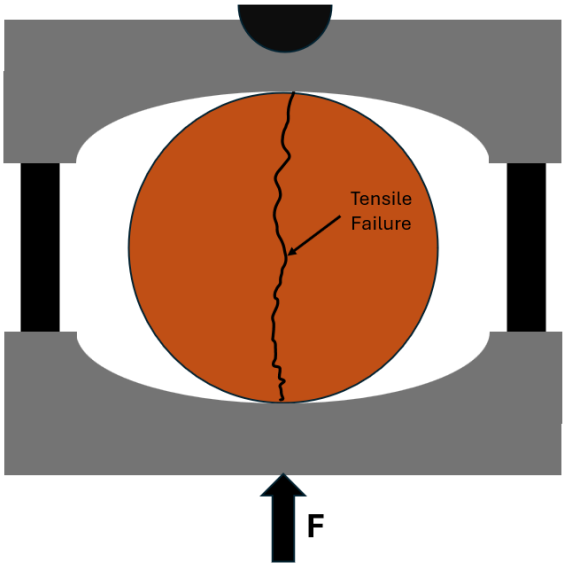

Figure 3.5: Set-up used for this thesis, with tensile crack example.

3.2.1. Testing Methodology

The first step of the sample preparation was described in section 3.1.1. The specific water content of 40% dw was selected based on the Proctor compaction test of the original material (Appendix B). Optimal compaction was observed at 40% dw. Since all samples originally showed a higher water content, they were first left to dry until the desired water content was reached. In some cases, samples were left to dry until a moisture content slightly under 40% dw was reached. At which point, samples were re-hydrated and allowed to equilibrate over night. This step ensured that the clay had time to swell, and that the water content was evenly distributed throughout the sample. Afterwards, samples were sieved to 4 mm. This was implemented in order to comply with ASTM standard D3967−23 [5], which requires the largest soil constituent to be 10 times smaller than the diameter of the disc (5cm) [5].

(a) Picture of the dredged material, after drying.

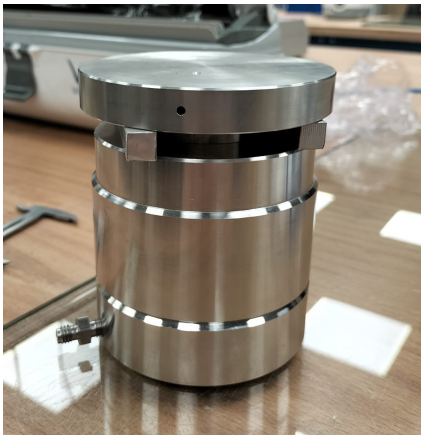

(b) Compression mold used for making Brazilian test discs.

Figure 3.6: Dredged material after drying, and the mold used to compress it.

Two sets of tests were conducted in this thesis. In the first set, all samples were compacted to the same dry density. As level of compaction directly affects tensile strength (section 2.1.2), this testing methodology compared the inherent tensile strength of each sample. A dry density of 1.14 g/cm^3 was selected, corresponding to the Proctor density of the original material . In the second set of tests, samples were compacted to 95% of their own Proctor density, which is a common test in dike construction [95]. This procedure compared tensile strength of samples under an actual dike application condition.

(a) UCS machine used for the BTS test.

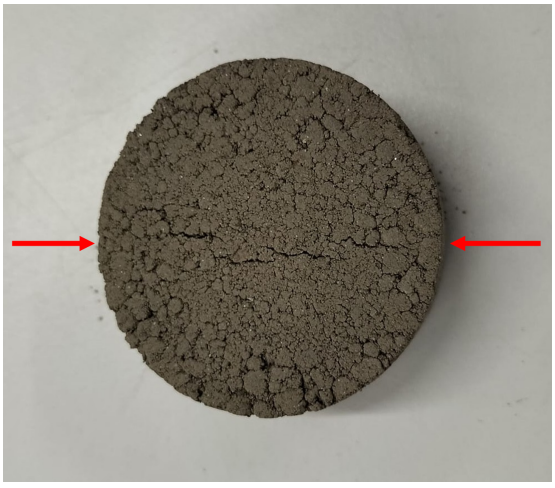

(b) Sample disc with 5 cm diameter after failure in the BTS test. Arrows indicate the failure plane.

Figure 3.7: UCS machine and the specimen after failure.

Sample compaction was conducted with the mold pictured in Figure 3.7b. The mold produced discs 2 centimeters in height and 5 centimeters in diameter, resulting in a radius to thickness ratio of 0.8. This is in line with the suggested radius to thickness range of 0.5-0.8, which was found to give ideal results [58].

The mold was placed in a 50 kN hydraulic press, at a controlled loading rate of 0.01 kN/s. This compaction rate was selected to allow the soil particles sufficient time to rearrange themselves during compaction. Samples were prepared in bulk before testing, and each one was wrapped in cellophane. This was to prevent moisture loss during the preparation stage. The resulting disc is seen in Figure 3.7b. Prior to testing, the dimensions of each disc were measured. A bounce-back effect was often observed in the disks, and the average observed height was approximately 21 millimeters. This deviation was taken into account when calculating the tensile strength with equation 3.5.

Using the frame pictured in figure 3.7a, samples were subjected to a controlled displacement rate of 0.05 mm/s until failure. This rate follows the ASTM standard [5], which recommends that tensile failure occur within 1 to 10 minutes of starting the test. The standard then defines the maximum observed load as the point at which tensile failure occurs (exemplified in figure 3.8b). This was seemingly confirmed visually, as the peak load highlighted in Figure 3.8b was consistently the point at which a tensile crack first appeared in the sample.

(a) Tensile Crack observed in one of the tests.

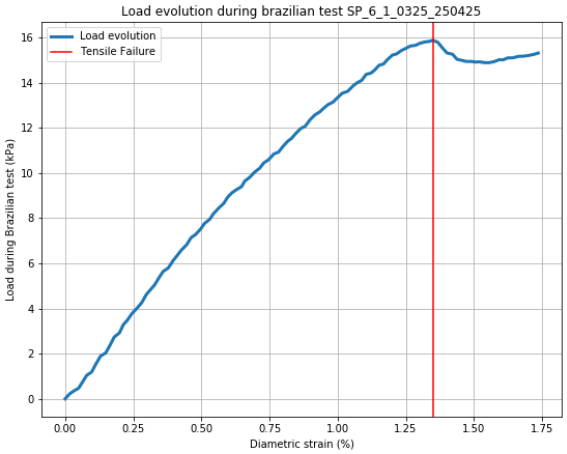

(b) Graph showing stress over strain, with the identified failure point highlighted with a vertical red line. Example of a test conducted on SP6 from March 2025.

Figure 3.8: Tensile crack, and the respective peak load.

Sample deformation was observed during loading, which is an expected consequence of the controlled displacement rate. This deformation is negligible if brittle behavior is observed, and the assumptions made in equation 3.5 still hold.

The sample analyzed in this thesis, however, exhibited ductile behavior. A different analysis is necessary in such cases. Two stages can be observed in Figure 3.9: before and after an inflection point. During the first stage, the stress-strain response is approximately linear, and the tensile strength of the sample can be considered fully mobilized [25]. In the second stage, the slope of the line decreases, attributed to microcracking within the sample [44]. At this point, additional load is no longer only supported by tensile strength, but also by sample compression. Consequently, the assumption that the maximum load corresponds to the tensile strength is no longer valid.

Gaspar and Jacobsz [25] recommend to take a conservative estimate of the tensile strength in such cases . This estimate was made based on the inflection point, defined as the stress before first tensile yielding occurred [25], and marked as ”tensile yielding point” in Figure 3.9.

After the test, a repeated measurement of the moisture content was taken to validate the results.

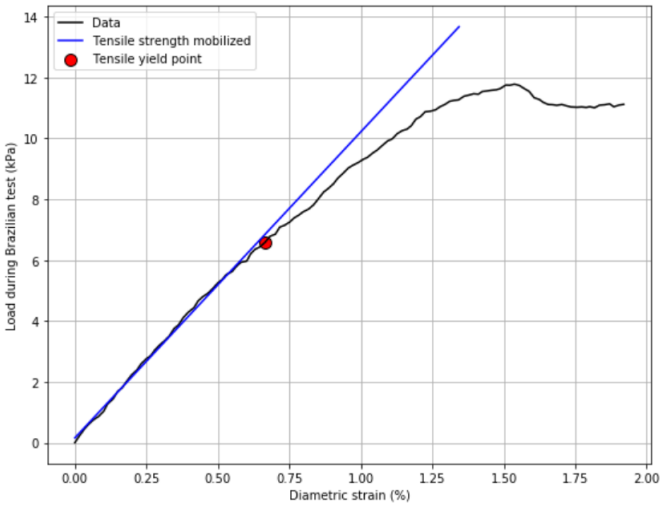

Figure 3.9: Exemplary result of a BTS test, conducted on SP6 material from March 2024. The inflection point where tensile yielding can be observed, is highlighted .

3.3. Crack Formation Experiment

The material utilized for the crack formation experiments was first prepared according to the procedure described in section 3.1.1. Then, the water content was increased to 90% dw, in order to achieve saturation. To ensure sample homogenization, samples were hand-mixed for three minutes, and poured into the crack formation mold. The mold, made of plastic, had dimensions of 15 by 15 centimeters, and a height of 12 millimeters. The sample and mold are shown in Figure 3.10a.

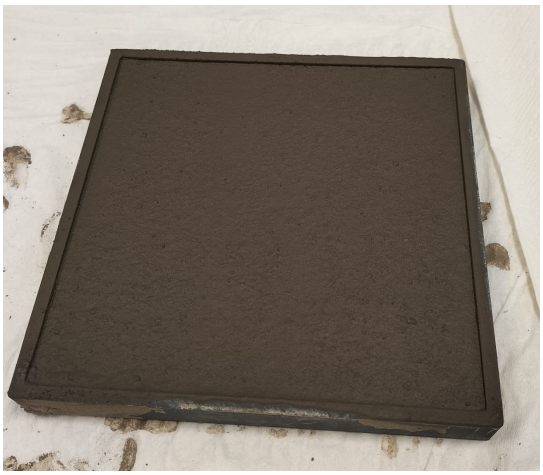

(a) Filled mold used for the crack formation test.

(b) Set-up used for the crack formation test.

Figure 3.10: Mold and set-up for the crack formation experiment.

After pouring, samples were placed in a vibrating table for five minutes to remove entrapped air bubbles. These preparation steps guarantee an initially saturated state [70]. Finally, the excess material was trimmed off to ensure consistency of the initial thickness - a fundamental parameter influencing crack formation (see section 2.3.6).

3.3.1. Experiment Set-up

The set-up for the crack formation tests is presented in Figure 3.10b. The sample was placed on top of a scale taking hourly measurements, in order to monitor moisture loss in the sample.A camera was

fixed fixed above the sample, and was set to take pictures every hour. To maintain constant lighting conditions for image analysis, an LED light was placed on top of the camera. Additionally, a humidity sensor was placed in view of the camera, so that the relative humidity could be monitored throughout the test. Finally, to minimize the effect of drafts and maintain stable drying conditions, boxes and a plastic barrier were set-up around the samples.

The test duration was determined based on the time needed for samples to reach a fully dried state. In Figure 3.11, an example of a test is plotted based on the sample weight over time. From that, it was surmised that each test should last for at least six days.

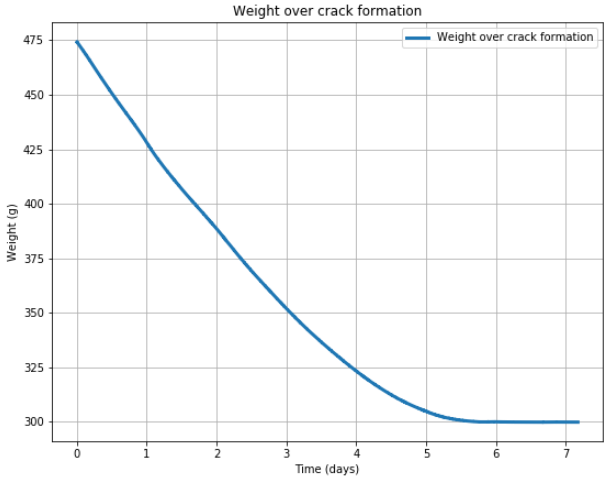

Figure 3.11: Weight loss due to desiccation over duration of test. Exemplary graph from SP-6 from March 2024.

3.3.2. Image Analysis

The flow-path for the image analysis is presented in Figure 3.12, and example images are given in Figure 3.13.

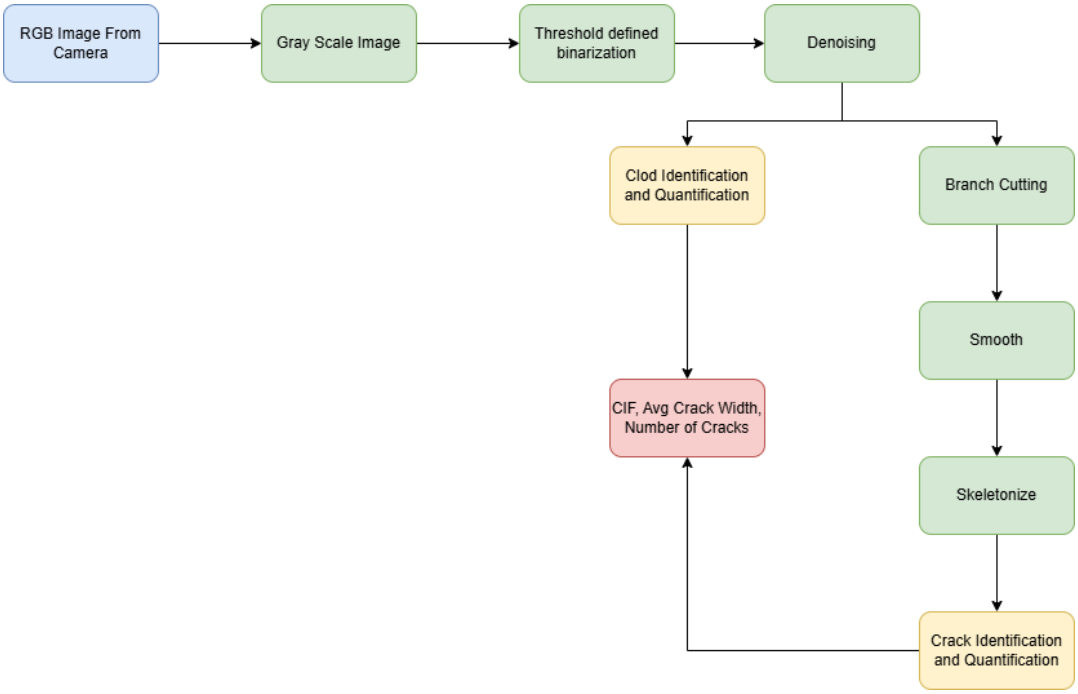

Figure 3.12: Flow-path for the image analysis.

The first step in the image analysis process was to crop the image to include only the mold. This was necessary due to the highly unstructured nature of the image around the mold, which would interfere with subsequent processing steps. The cropped image (Figure 3.13a) was then used as the input for the analysis software.

Image analysis was carried out using the CIAS software, developed by Nanjing University [94]. The image was first turned into a gray-scale copy of itself (Figure 3.13b. This facilitates binary processing of the image, as instead of each pixel containing three values (red, green and blue), it contained only one intensity value. The lightest pixels in the original image were turned into white, and the darkest into black. Values in between are given different shades of gray [59].

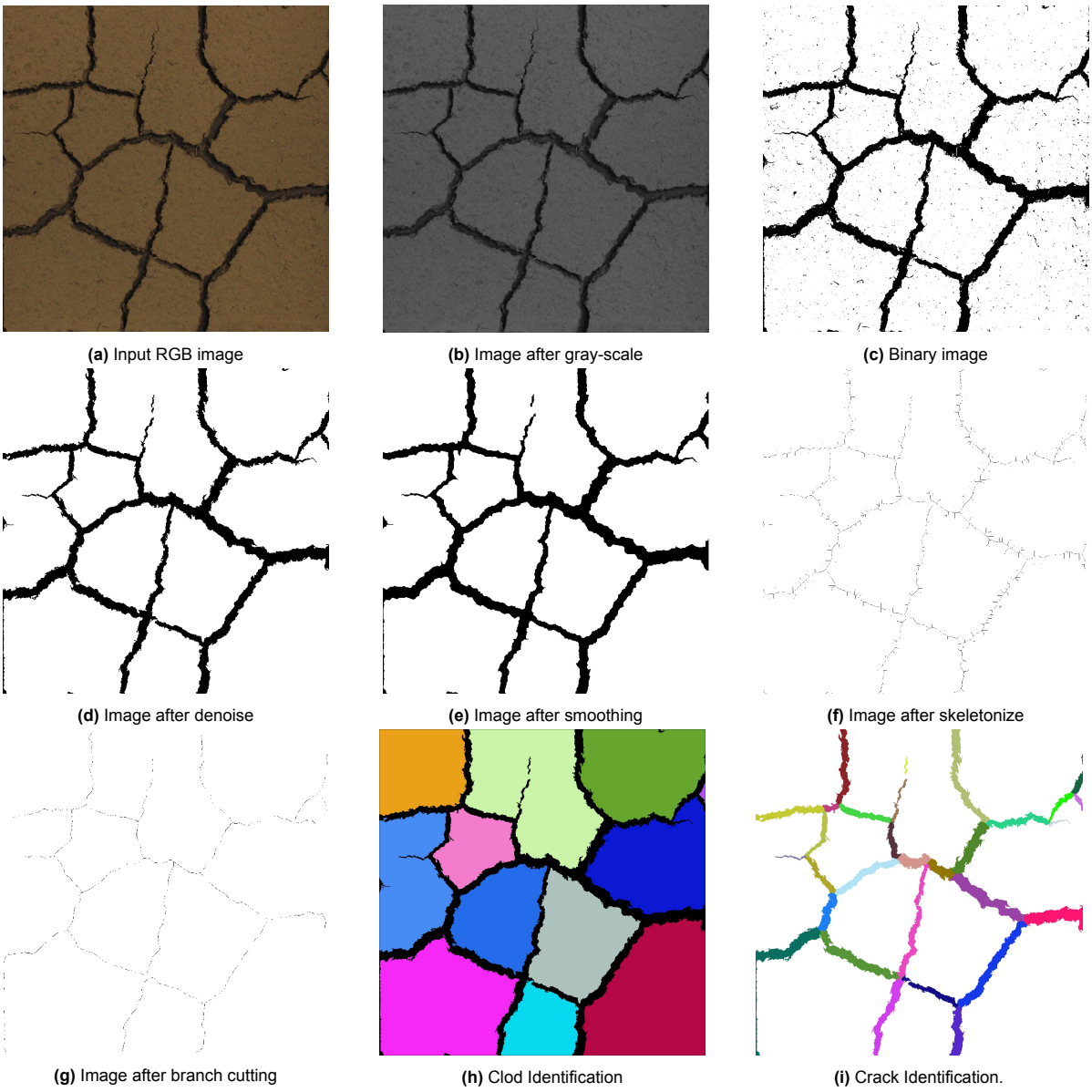

(a) Input RGB image **(b)** Image after gray-scale **(c)** Binary image

(d) Image after denoise **(e)** Image after smoothing **(f)** Image after skeletonize

(g) Image after branch cutting **(h)** Clod Identification **(i)** Crack Identification.

Figure 3.13: Image processing steps.

Next, the image underwent binary processing. That is, converting from gray-scale into a black and white image. In this step, each pixel was assigned a binary value: pixels with intensity below a certain threshold were set to white (0), and those above it to black (255). This threshold can be defined automatically, or for this thesis, decided by the user. The threshold was decided by analyzing the histogram of the gray values, and selecting the threshold that would yield the clearest image (best crack/clod distinction).

The resulting binary image (Figure 3.13c) already shows a clear differentiation between cracks and intact area. However, there is still considerable noise to be eliminated. These artifacts were caused by the uneven nature of the sample, which can lead to lighting variations, and consequently, dark spots in areas that are not cracked. To remove these, a denoising operation was conducted. The area of clusters was calculated by the software, and spots smaller than a certain size were removed. This ignores the cracks, as they have an area larger than the threshold. The selected threshold was determined based on the smallest observed crack, so that only non-crack-related noise was removed. The resulting image (Figure 3.13d) was ready for the clod identification. This was executed by categorizing each connected white region as a distinct object (see Figure 3.13h).

Next, a smoothing operation was performed to facilitate crack identification. The smoothing was performed using the OPEN function, which performs an ERODE operation followed by a DILATE operation. The ERODE operation replaces each pixel with the minimum value within a 3x3 area. DILATE does the opposite, replacing each pixel with the darkest in a 3x3 area. This essentially smoothens the crack boundaries and fills in small holes [55], improving the accuracy of crack detection.

From the smoothed binary image (Figure 3.13e), the skeleton of the cracks can be extracted, equivalent to the central axis of each crack. The SKELETONIZE function iteratively removes pixels from the edges of the crack shapes until only a one-pixel-wide structure remains. These skeletons follow the geometry of the cracks. However, due to the natural tortuosity and uneven contours of the cracks, many small inaccuracies were skeletonized (Figure 3.13f). These manifest themselves in the skeleton as numerous small branches. To accurately get the crack pattern and structure, they need to be eliminated.

Branch cutting operates by first identifying and categorizing the ends of each continuous skeleton segment as either an end-point or an intersection. Then, starting from each end-point, the number of pixels is counted until an intersection is reached. If this segment is shorter than a threshold determined by the user, it is eliminated. The threshold that defines this cutting length corresponds to the length of the longest observable branch.

Once the skeleton is cleaned (Figure 3.13g), it can be used to accurately identify cracks. This is performed by mapping the refined skeleton back onto the original binary image. Each segment within two intersections is defined as a separate crack (see Figure 3.13i).

With the cracks and clods identified, the relevant results can then be extracted using CIAS software [94]. For this thesis, the key parameters are: the Crack Intensity Factor (CIF), the number of cracks, and the average crack width. All of these give insights into the tendency of soil samples to crack.

The CIF is defined as the ratio of the total crack area (A_c) to the intact (clod) area (A_I):

$$CIF = \frac{A_c}{A_I} \tag{3.6}$$

The number of cracks and average crack width was obtained from the crack network segmentation and identification. It should be noted that these two parameters are reported in pixels, instead of standard measurement unit such as millimeters. This is because, as discussed in section 2.3.2, these results are highly dependent on the test boundary conditions. As such, evaluation is performed based on the relative changes (given in pixels), allowing comparison of samples amongst each other.

3.4. Atterberg Limits

The Atterberg Limits include the liquid Limit, the plastic limit, and the shrinkage limit (not investigated).

3.4.1. Liquid Limit

The liquid limit is defined as the water content at which the soil transitions between a plastic and liquid state. It is determined using the falling cone method, specified in the ISO standard 17892-12 [41]. The test utilizes the fall-cone device (shown in Figure 3.14) to measure the consistency of the soil. The test requires a sample sieved to 425 micrometers, which is obtained using a wet sieving method. The

resulting washings are collected and left to dry until a consistency corresponding to a cone penetration of about 15 mm is reached.

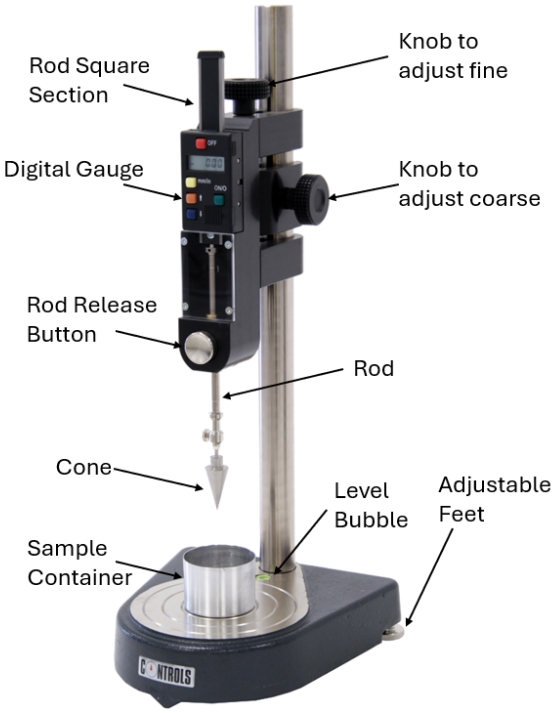

Figure 3.14: Fall cone device [13].

Once the initial penetration of around 15 millimeters is observed, a portion of the sample is removed from the container, to calculate its water content. A total of four penetration depths, ranging from 15 to 25 mm need to be measured, as well as their corresponding water contents (equation 3.1). The result is a penetration-water content graph, as seen in Figure 3.15.

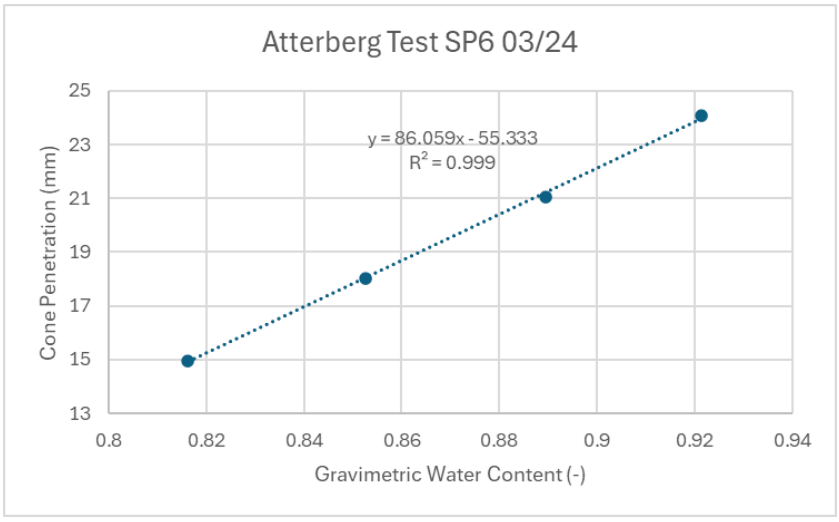

Figure 3.15: Exemplary result of the cone penetration test, conducted on SP6 material from March 2024.

Analytically, the liquid limit is defined as the interpolated water content at a penetration depth of 20 millimeters. This value is obtained from the linear fit of the data.

3.4.2. Plastic Limit

The plastic limit is defined as the lowest water content at which the soil is plastic. The test [41] is again conducted on sieved material (<425 μm), with about 40 grams needed. First, the sample - with a higher water content than the plastic limit- is rolled into a ball. By continuously hand-rolling the ball, it loses water content from the warmth, until cracks begin to appear. At this point, the ball is divided in two, and then each part divided in four, to ease handling in the next step.

These eight portions are then hand-rolled into a cylinder of around 6 millimeters. Using a glass plate, the cylinder is further rolled to a smaller diameter of about 3 millimeters. At these dimensions, if the sample reaches its plastic limit, it crumbles. If the limit is not reached, the sample is remolded and rolled again. This will mechanically dry out the sample, until its eventual crumbling at 3 millimeters. At which point the moisture content is taken, and the average value is taken as the plastic limit.

3.4.3. Plasticity and Consistency Indexes

The plasticity index I_P is calculated using the liquid (W_L) and plastic (W_P) limits, through equation 3.7.

$$I_P = W_L - W_P \tag{3.7}$$

It is an important parameter for determining the suitability of a soil to be used is dike construction, as explained in section 2.5.2. Another important parameter is the consistency index, calculated through equation 3.8.

$$I_C = \frac{W_L - W}{W_L - W_P} \tag{3.8}$$

Finally, the liquidity index is calculates through equation 3.9.

$$I_L = \frac{W - W_P}{W_L - W_P} \tag{3.9}$$

3.5. Coefficient of Linear Extensibility (COLE)

The coefficient of linear extensibility (COLE) is a measure of a soil's capability to swell and shrink under the prevailing conditions of temperature and relative humidity. First, the sample (around 100 grams) is mixed with water. The water content needs to be adjusted so that a paste slightly drier than saturation is obtained. In practice, this means that the paste should not flow when tilted. This mixture is left to equilibrate over 24 hours. Next, a syringe with an opening of 1 centimeter is filled with the paste. This allows for a rod to be slowly extruded unto a smooth surface, until it reaches a length of a little over 6 centimeters. A wet spatula is used to cut the rod at exactly 6 centimeters length. This is repeated three times per sample. The rod is then left to air-dry for 48 hours, and re-measured. The COLE can then be calculated with equation 3.10:

$$COLE_{rod} = \frac{L_m}{L_d} - 1 \tag{3.10}$$

Where: L_m is the rod length when wet, and L_d is the rod length after drying.

The rods are also oven-dried afterwards, to obtain a second COLE measurement related to drying at 105 deg C. This value is less dependent on relative humidity during sample drying.

3.6. Microscopy

Microscopy images of the samples were taken as an additional input to characterize the material. No

quantification was conducted on the images. Instead, they were used for interpretation of the results, as they contextualize the microstructure of the soil, which influences its mechanical properties.

First, the samples were analyzed with a Keyence light microscope VHX-X1. The analyzed samples came from the Brazilian Tensile Strength (BTS) tests, and no alteration was made after tensile failure. The samples were split open along the crack, in order to get a fresh surface. The analysis itself consisted of taking pictures at multiple resolutions. Wet samples were used, but at higher resolutions, the effect of water was all that could be observed. Therefore, only dried samples were used afterwards.

Next, the samples were analyzed with a Quanta™ 650 FEG scanning electron microscope. The higher resolution of the microscope meant some sample preparation was necessary. Again, BTS test samples were used. They were first trimmed down to a dimension of 2 centimeters by 2 centimeters. This smaller sample still included the tensile fracture, so that it could again be opened to obtain a fresh view. The samples were first scanned through with a low-resolution, to get a full view. This was to ensure that focus wasn't given to an irregularity, as zoomed in images were taken in areas of interest.

4

Results

4.1. Tensile Strength

Tensile Strength results for materials collected at the end of ripening (March 2024 to March 2025) are presented in Figure 4.1. For comparison, tensile strength of the original (HIP) material is also shown, allowing assessment of how the TS evolved after two years of stockpiling.

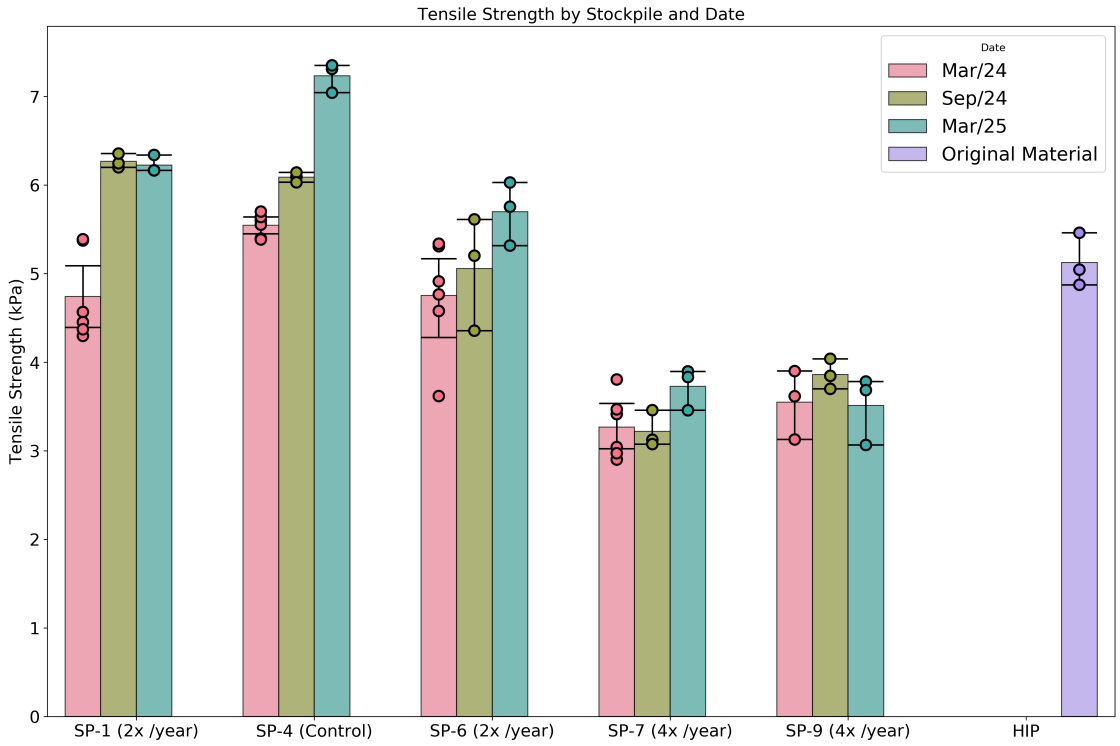

Figure 4.1: Tensile strength of material from stockpiles 1,4,6,7,and 9 from March 2024 until March 2025. HIP = High Intensity Press, original material from the METHA plant.

According to ASTM standard [5] ten replicate tests per sample are recommended. However, fewer replicates are required if reproducibility is high, that is, if a coefficient of variation (CV) smaller than 5% is observed. Most samples met this criteria (table C.1), resulting in an average of only three replicate tests per sample. A higher number of replicate tests were conducted for March 2024 samples, as extra tests were carried out to assess the accuracy of the load cell. Details of these testing runs are provided in Appendix C.

Figure 4.1 shows a clear relation between tensile strength and stockpile management practices. Specifically, TS is inversely correlated with the turning rate. SP-7 and SP-9, with turning rates of 4 times a year, consistently exhibited TS values lower than the original material. On average, measured TS of SP-7 and SP-9 was about 30% lower than the original material. Moreover, no significant variation was observed throughout the investigated ripening period.

In contrast, the highest tensile strength values were found in SP-4 (Control), where no turning was performed, and vegetation growth was unrestricted. TS increased over time, and at the last sampling period (March 2025), exhibited values approximately 50% higher than the original material. A similar trend was observed in SP-1 and SP-6 from March 2025, which were turned twice per year. Their average TS value was approximately 21% higher than the original material.

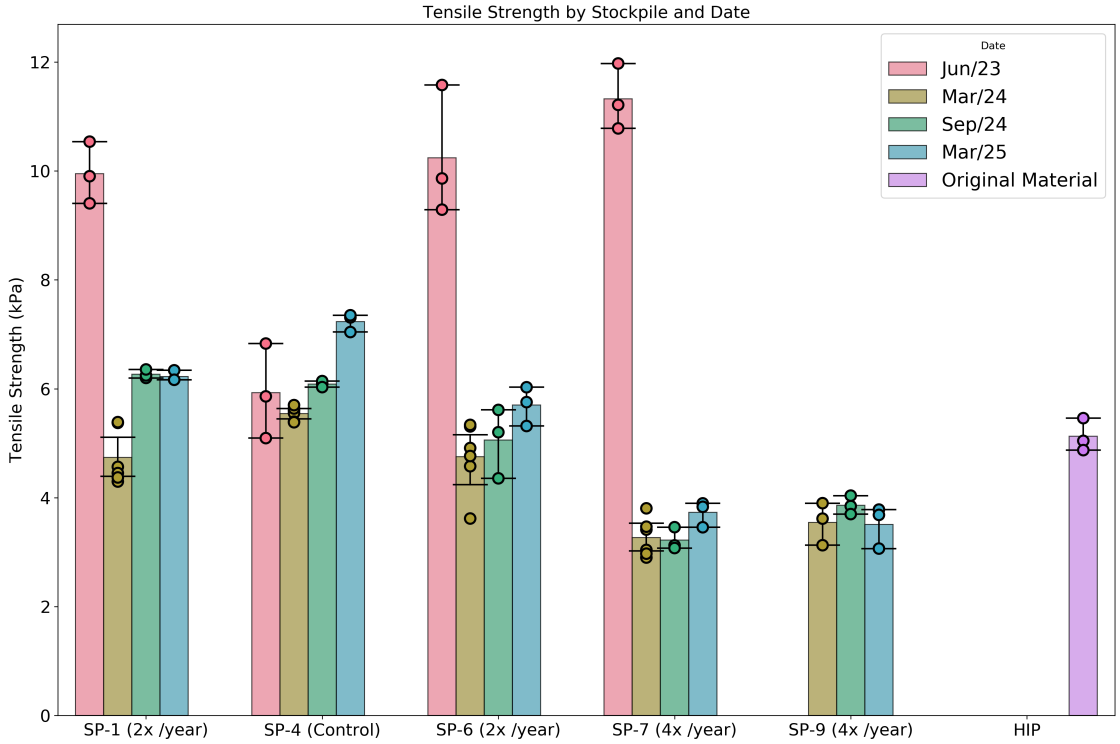

Figure 4.2: Tensile strength of material from stockpiles 1,4,6,7,and 9 from June 2023 until March 2025. HIP = High Intensity press, original material from the METHA plant.

Figure 4.2 includes additional tensile strength results from samples at an early stage of ripening - six months after stockpiling. At the time of sampling (June 2023), SP-1, SP-6, SP-7 and SP-9 had undergone only one turning event. SP-9 was excluded from the analysis due to insufficient material for testing, although a similar behavior to SP-1, SP-6, and SP-7 is expected. These three stockpiles exhibited elevated tensile strength values, about 115% higher than the HIP material. However, following subsequent turning events, all three showed a sharp decrease in tensile strength. SP-4, which experienced no turning, exhibited a lower tensile strength in June 2023, that increased over time.

Finally, Figure 4.3 shows tensile strength tests conducted on September 2024 samples at 95% of their Proctor density - a standard compaction rate for dike construction [95]. Proctor density was determined for September 2024 samples, at the late stage of ripening. The corresponding compaction curves are provided in Appendix B.

The tensile strength values at 95% Proctor density showed a trend opposite to the TS measured at a density of 1.14 g/cm^3. SP-9, with the lowest TS at 1.14 g/cm³, had the highest compactability, and TS values 430% higher than the original material. In contrast, SP-4, which previously exhibited the highest TS, had the lowest compactability. SP-4 exhibited TS values 280% higher than the original material. SP-1 and SP-6 showed similar results, despite a slightly higher compaction rate.

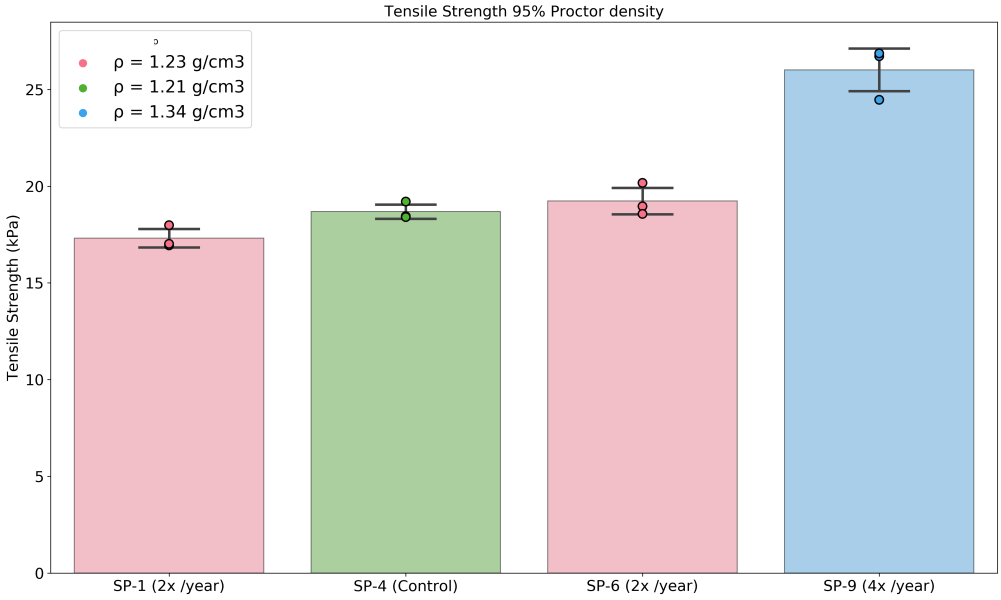

Figure 4.3: Tensile strength of material from stockpiles 1,4,6,and 9 from September 2024. Samples were compacted to 95 % of the respective Proctor density at a water content of...Density values refer to 95% of their Proctor density.

4.2. Crack Formation

Crack Intensity Factor (CIF) results for materials collected at the end of the ripening period (March 2024 to March 2025) are presented in Figure 4.4. An additional timestep was tested for SP-4, with material from September 2023.

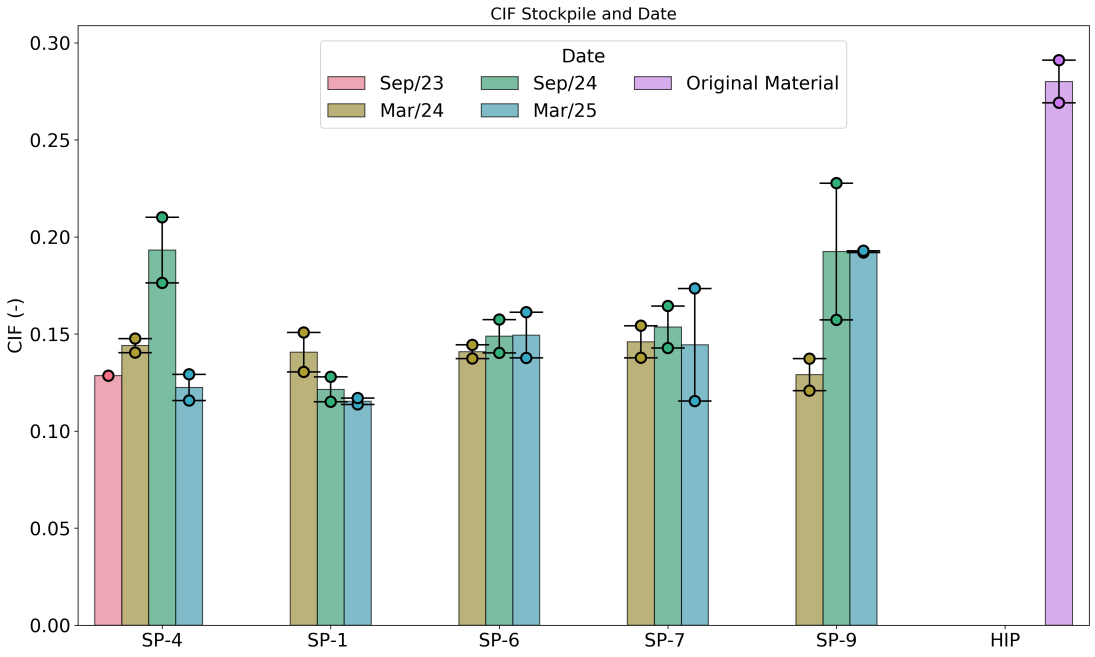

Figure 4.4: Crack Intensity Factor (CIF) of material from stockpiles 1,4,6,7,and 9 from September 2023 until March 2025. HIP = High Intensity press, original material from the METHA plant.

Overall, the CIF results do not display a consistent trend. SP-6 and SP-7 maintained relatively stable CIF values throughout the study period, despite the different turning rates between both stockpiles. SP-9 exhibited the highest average CIF, except for the March 2024 sample, and showed a notable

difference between replicates in results from September 2024. SP-1 and SP-4 both demonstrated a slight decrease in CIF over time, although SP-4 showed a high value in the sample from September 2024. The most important result to note then, is that all observed CIF values from the stockpiled material were lower than those from the original material. While the stockpiled samples averaged a CIF of approximately 0.15, the HIP material exhibited a CIF closer to 0.30.

The second parameter derived from image analysis was the average crack width, shown in Figure 4.5.

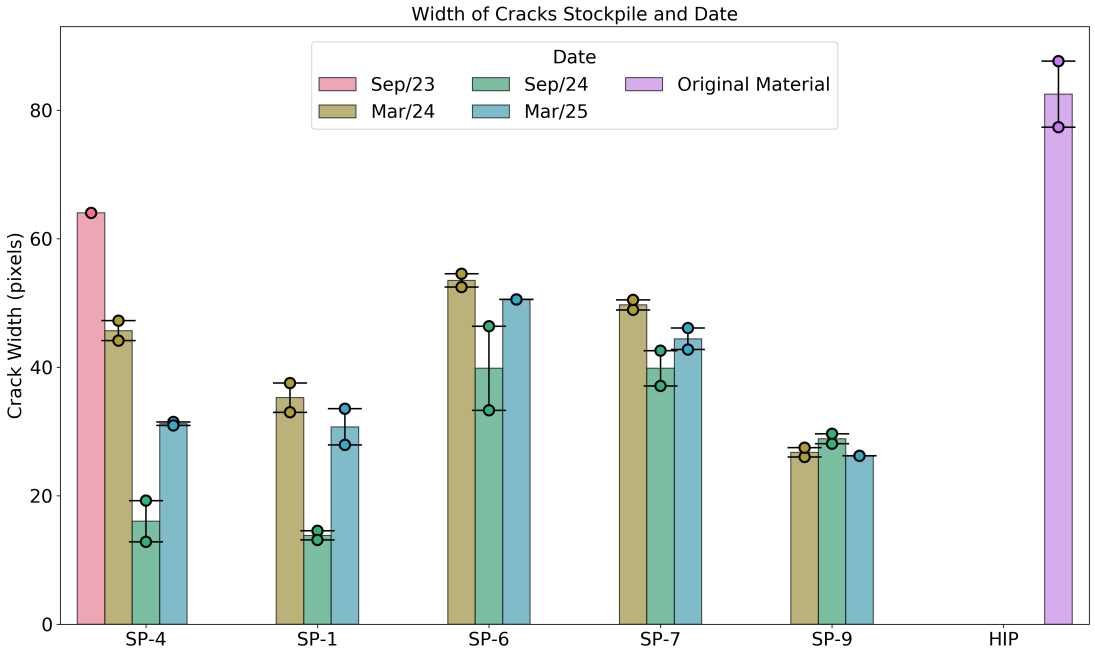

Figure 4.5: Average width of the cracks (in pixels) of material from stockpiles 1,4,6,7,and 9 from September 2023 until March 2025. HIP = High Intensity press, original material from the METHA plant.

SP-9 exhibited the most consistent results, giving on average the smallest crack widths throughout the ripening period.

In contrast, the widest cracks were found in SP-7 and SP-6, with SP-4 and SP-1 in between. Samples from September 2024 (except for SP-9) consistently exhibited smaller cracks than in adjacent sampling campaigns. The widest cracks were observed in the original material, approximately twice the averaged value of the stockpiled materials. This difference is illustrated in Figure 4.6.

(a) Final crack pattern for HIP material. Slightly darker tone is due to lighting, and had no effect on image analysis.

(b) Final crack pattern for SP-6 from March 2024.

(c) Final crack pattern for SP-6 from March 2025.

Figure 4.6: Comparison between cracking intensity of the original material versus SP-6 at two ripening periods. The average crack width and CIF in SP-6 are smaller than the original material, but no large variation was observed in later periods of ripening.

Finally, the number of cracks is presented in Figure 4.7, equivalent to the crack density.

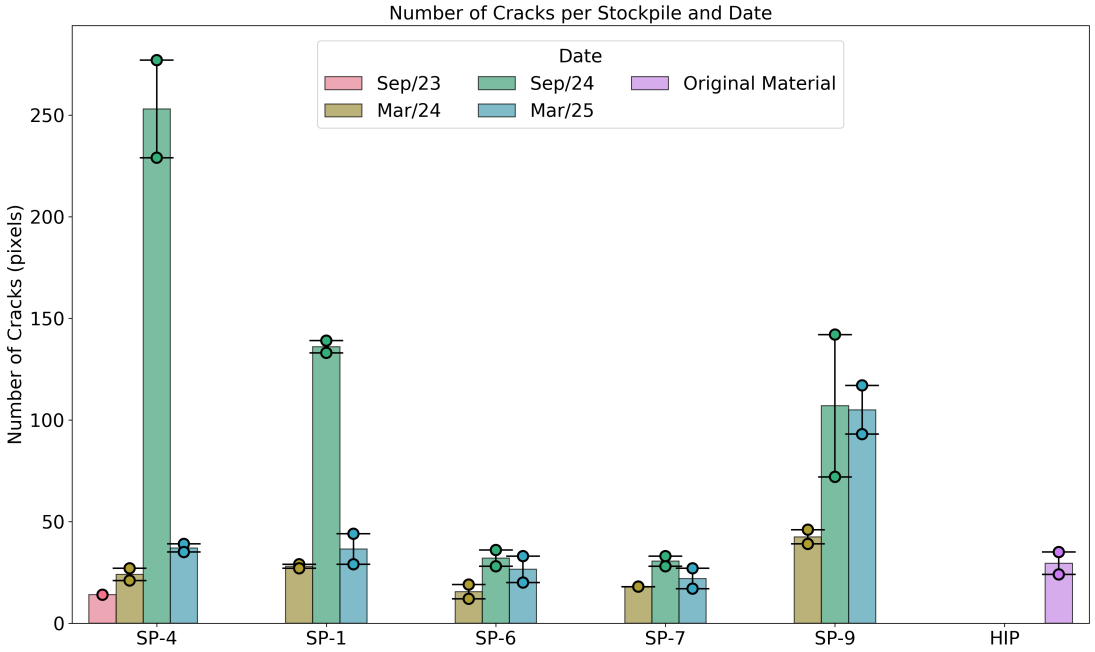

Figure 4.7: Number of cracks per test of material from stockpiles 1,4,6,7,and 9 from September 2023 until March 2025. HIP = High Intensity press, original material from the METHA plant.

The number of cracks show a similar pattern to the crack width, but reversed. This was expected, as the formation of smaller cracks tend to occur in greater numbers. SP-9 from March 2024 exhibited smaller cracks than in the later periods, which explains the lower CIF observed in the sample. Again, SP-1 and SP-4 had an abnormal result in September 2024, with a large number of small cracks. This anomalous behavior is pictured in Figure 4.8.

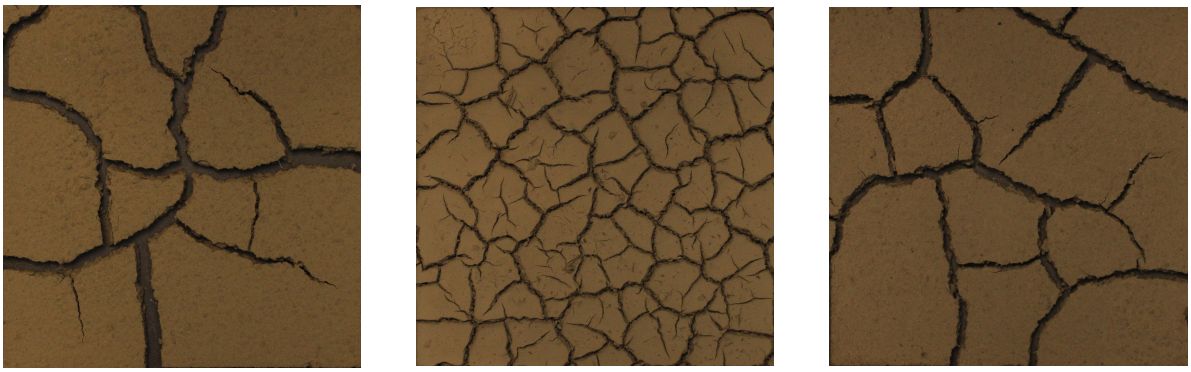

(a) Final crack pattern for SP-4 from March 2024.

(b) Final crack pattern for SP-4 from September 2024.

(c) Final crack pattern for SP-4 from March 2025.

Figure 4.8: Comparison between different ripening periods. The pattern drastically changes for the sample of September 2024.

Unlike CIF and crack width, the number of cracks in the original material was comparable to that of the stockpiled material. However, the cracking behavior is very different, as the cracks were significantly wider.

Overall, crack formation results did not show a clear influence from stockpile management practices, as a pattern could not be derived from different turning rates. All stockpiled samples, however, exhibited less cracking than the original material.

Additional analysis was performed on the five samples that were monitored during desiccation. This

includes identifying the moisture content at which cracking first occurred, and the range of relative humidity values observed during drying. The results are presented in Table 4.1.

Table 4.1: Water content at the appearance of the first crack in the sample. RH = Relative Humidity.

Samples	Water Content (% dw)	RH Range (%)
SP-6 03/24	64.63	31-42
SP-7 03/24	64.18	45-63
SP-9 03/24	60.35	37-45
SP-7 09/24	63.75	65-50
SP-7 03/25	70.53	43-57

Samples showed a consistent moisture content at crack initiation of 60 - 65 % dw. The exception was SP-7 from March 2025, which initiated cracking at 70 % moisture content, despite relative humidity values comparable to other samples. It should be noted that these results were obtained from different samples, which means identifying a relationship between water content at first cracking and relative humidity is difficult, as all samples exhibit different crack formation characteristics.

4.3. Atterberg Limits

Atterberg limits values are shown in table 4.2. The linear data fits used to determine the liquid limits are presented in appendix D, and the resulting plasticity index was calculated using equation 3.7. Some of the liquid and plastic limits were previously obtained as part of the S2S project; to distinguish them, values measured during the thesis are shown in **bold**.

Table 4.2: Liquid limit, plastic limit, and resulting plasticity index for stockpiles 1,4,6, 7, and 9. Values obtained experimentally during this thesis are in **bold**.

Sample	Liquid Limit (%)	Plastic Limit (%)	Plasticity Index
SP-1 03/24	**88.82**	56.23	32.58
SP-4 03/24	**86.95**	51.57	35.39
SP-6 03/24	**87.54**	50.92	36.62
SP-7 03/24	**77.55**	56.94	20.61
SP-9 03/24	**70.01**	53.77	16.24
SP-1 09/24	92	58.53	33.47
SP-4 09/24	90.95	59.63	31.33
SP-6 09/24	71	39.67	31.33
SP-7 09/24	82.5	51.39	31.11
SP-9 09/24	76.40	68	8.4
SP-1 03/25	**77.75**	**49.79**	27.96
SP-4 03/25	**75.15**	**47.88**	27.27
SP-6 03/25	**83.53**	**53.54**	29.99
SP-7 03/25	**67.62**	**47.82**	19.79
SP-9 03/25	**74.83**	**48.56**	26.27

To visualize requirements set by the TAW guidelines [85] (see also Table 2.3), the results from table 4.2 were plotted based on liquid limit and plasticity index values. These parameters classify the erosion resistance of the samples, shown in Figure 4.9.

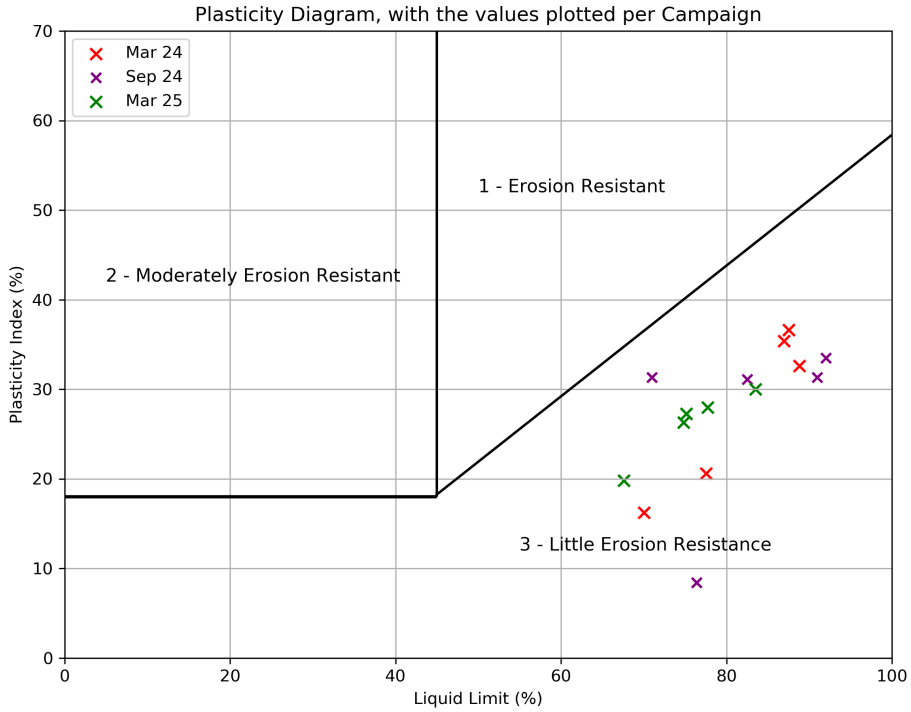

Figure 4.9: Relationship between Plasticity Index and Liquid Limit (Plasticity diagram) showing different erosion resistance zones based on criteria from table 2.3.

The diagonal line dividing zones 1 and 3 in Figure 4.9 is defined by equation 4.1, and is called the A-line.

$$I_P = 0.73 \cdot (w_1 - 20) \tag{4.1}$$

All samples fall into the third category: Little erosion resistance. This classification arises from high liquid limit values, combined with a high plastic limit. This means the plasticity index is not large enough to offset the high liquid limit.

The lowest observed liquid limit was from SP-7 03/25, with 67.62 % dw. The highest observed liquid limit was from SP-1 09/24, with 92 % dw. Regarding stockpile management, the lowest values for the liquid limit and plasticity index generally come from SP-7 and SP-9, which have a high turning rate (4x per year).

An exception to this is SP-7 from September 2024, which showed a relatively high plasticity index (31.11 %), compared to the other samples with a high turning frequency. This data point was collected previously in the S2S project, however, and the determination of Atterberg limits have been observed to be investigator dependent. The liquid limit and plasticity index decreased over time for every stockpile, with the exception of SP-9.

The water content for working of the soil in cores is another important parameter (see table 2.4). It defines an upper boundary for the water content on application (w_n), given the relationship:

$$w_{opt} \leq w_n \leq w_{max}$$

Where w_{opt} is the optimum water content given by the Proctor density, and w_{max} is the maximum water content. Dutch regulations define w_{max} by the consistency index ($I_C \geq 0.60$), and German regulations define w_{max} based on the liquidity index ($L_I \leq 0.3$). This range is presented in Table 4.3.

Table 4.3: Upper and lower boundaries for the material's water content on application. Maximum Water content is presented for Dutch and German regulations. Wc = Water Content.

Sample	Optimum Water Content: w_{opt} (%)	Maximum Wc Dutch: w_{max} (%)	Maximum Wc German: w_{max} (%)
SP1 03/24	40.08	69.27	66.01
SP4 03/24	34.91	65.72	62.18
SP6 03/24	37.86	65.56	61.90
SP7 03/24	32.60	65.18	63.12
SP9 03/24	35	60.27	58.65
SP1 09/24	32.43	71.92	68.57
SP4 09/24	35.03	72.16	69.02
SP6 09/24	37.86	52.20	49.07
SP7 09/24	36.21	63.83	60.72
SP9 09/24	32.89	71.36	70.52
SP1 03/25	-	60.97	58.18
SP4 03/25	-	58.79	56.06
SP6 03/25	-	65.54	62.54
SP7 03/25	-	55.74	53.76
SP9 03/25	-	59.06	56.44

Finally, plasticity index is linked to the crack formation behavior of a soil. A short comparison between it, CIF, and average crack width is presented in Table 4.4.

Table 4.4: Comparison between plasticity index and crack formation results for March 2025 samples.

Stockpiles	Plasticity Index (%)	CIF (%)	Average Width (pixels)	Comment
SP-1	27.96	11.54	30.72	
SP-4	27.27	12.25	31.21	
SP-6	29.99	14.95	50.54	Highest Ip, and largest average width
SP-7	19.79	14.45	44.42	Lowest Ip, but second largest average width
SP-9	26.27	19.24	26.21	Largest CIF, despite Ip comparable to other samples

4.4. Coefficient of Linear Extensibility

The Coefficient of Linear Extensibility (COLE) gives a measurement of a soil's shrinking response to drying. It is directly related to soil crack formation. As such, it was measured in order to contextualize the results presented in section 4.2. Figure 4.10 presents COLE results after air-drying the samples.

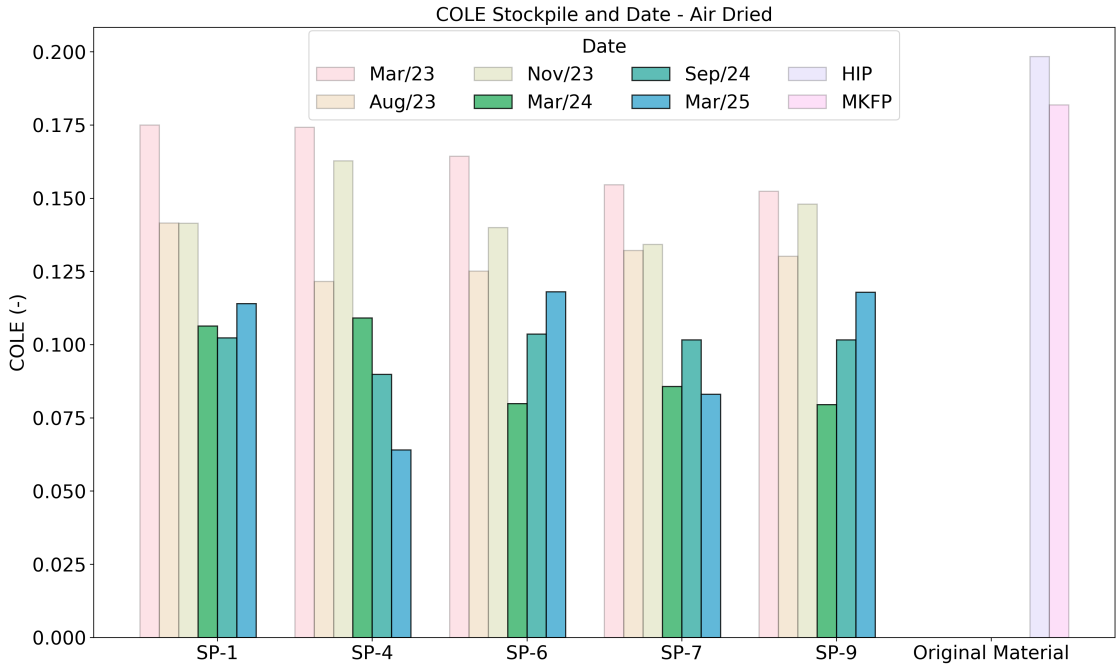

Figure 4.10: Development of COLE over time and stockpile, obtained after air-drying. COLE calculated in this thesis are highlighted.

A decrease in COLE values throughout the ripening period can be observed. Although SP-6 and SP-9 exhibit an increase in values in the later time periods, it is still lower than values obtained at the start of stockpiling. As air-dried results are susceptible to the influence of temperature and relative humidity, COLE tested in this thesis was also oven-dried. Results are shown in Figure 4.11.

Figure 4.11: Development of COLE over time and stockpile, obtained after oven-drying at 105 °C.

Overall, when looking at oven dried samples, a noticeable decrease in shrinking behavior can be ob-

served compared to the original material. Measured COLE values were 30-60% lower. No clear trend can be observed from figure 4.11, as samples were taken at a later stage of ripening, when COLE had stabilized. SP-4 shows a decrease in the COLE, while SP-6 increases over the one year time period.

4.5. Microscopy

In addition to the quantitative experiments, the soil microstructure was examined using scanning electron microscopy (SEM) to provide context to the results.

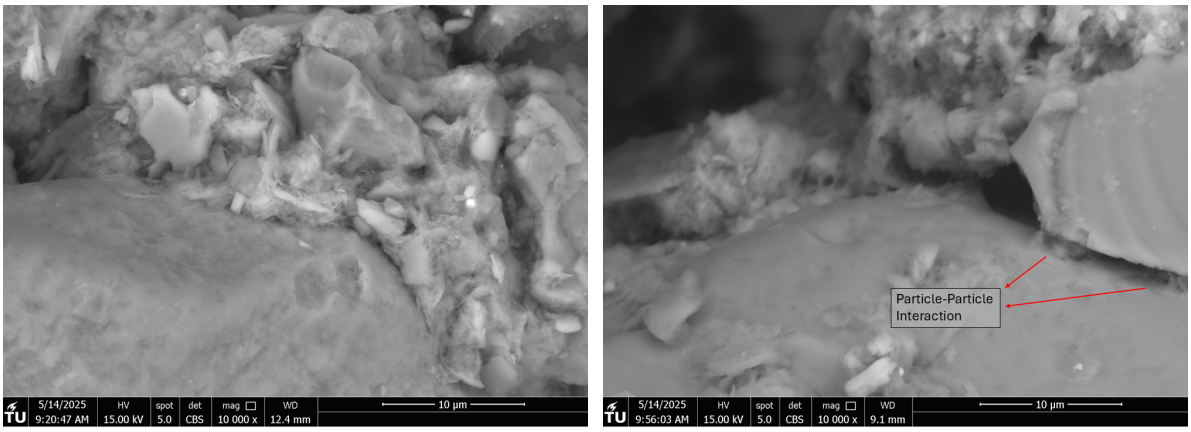

Figure 4.12: SEM pictures showing the interaction between different phases (left), and bridges connecting two larger grains (right).

Some notable features were identified. First, interactions between different soil phases and the formation of clay bridges were frequently observed, as pictured in Figure 4.12. The soil matrix was seen to adhere to larger grains, which is beneficial to the tensile strength of the material. However, this was not always the case, as very often cracks were observed between different phases (Figure 4.13). These cracks formed as a result the drying process prior to SEM imaging, which is necessary due to the vacuum environment required by the microscope. Additionally, interparticle bridges were observed between similarly sized particles, as illustrated in Figure 4.12. Again, this enhances cohesion within the soil matrix and contribute positively to its mechanical stability.

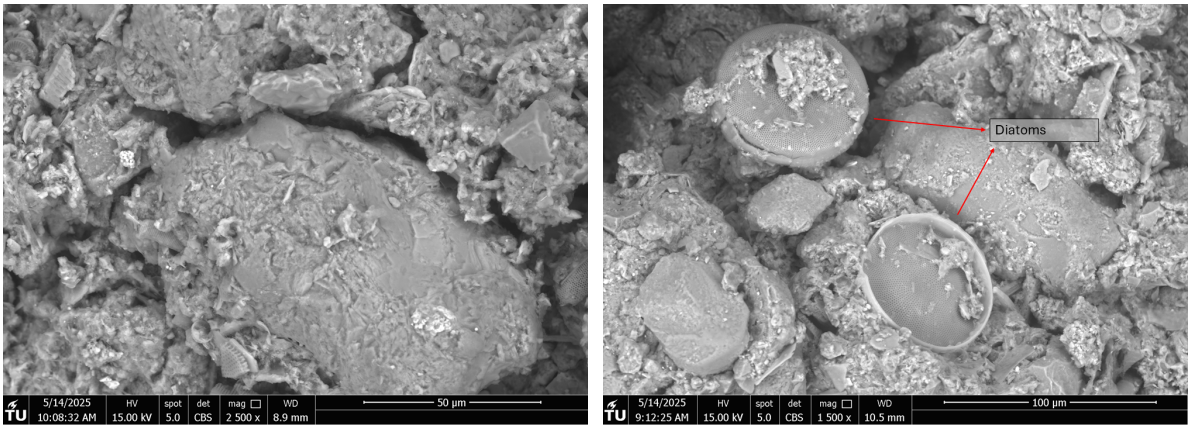

Figure 4.13: SEM pictures showing the cracks that form in the matrix (left), and the presence of diatoms in the soil composition (right).

Finally, another interesting phenomena to look at in the microscope is the matrix composition. Pictured in Figure 4.13, diatoms were prevalent throughout the samples, constituting a fundamental fraction of

the soil matrix. Their abundance is beneficial to the soil's physical characteristics, as the diatom's hollow and rough skeleton enhances the compressibility and shear strength of the soil through enhanced particle interlocking [85].

5

Discussion

5.1. Tensile Strength

Tests were carried out on materials from different stockpiles after two years of ripening. When compacted to a density of 1.14 g/cm^3, the highest tensile strength was observed on SP-4 (control). In contrast, the lowest TS values were measured in SP-7 and SP-9 (4x turning/year), with values lower than in the original material. SP-1 and SP-6 (2x turning/year) showed a higher tensile strength than the original material, but still lower than SP-4. Additionally, stockpiles subjected to minimal or no turning (SP-1, SP-4, and SP-6) showed a continued increase in tensile strength over time. TS in SP-7 and SP-9 stabilized after 2 years of ripening, suggesting minimal benefits from a higher turning frequency.

It was hypothesized in Chapter 1 that increased aeration would enhance tensile strength, as it leads to greater compactability and a stable structure [65], [113], [36]. This hypothesis appears valid during the early stages of ripening. Six months after stockpiling, SP-1, SP-6, and SP-7 indeed showed a much higher tensile strength than SP-4 (no turning), seen in Figure 4.2. These first three stockpiles had undergone one turning event, and exhibited an average tensile strength that was 77% higher than in SP-4.

However, subsequent turning events were observed to reduce TS in the materials. This reduction is likely due to the mechanical breakdown of the soil aggregates caused by repeated turning. Previous studies in agricultural soil management have shown that mechanical disturbance generally decreases soil tensile strength, as turning is used to increase friability for enhanced crop production [49].

Mechanical disturbance disrupts the compacted soil structure, leading to its reorganization into less stable, freshly formed aggregates. This results in decreased mechanical stability, and thus a lower tensile strength [8], [71]. This explains the tensile strength found in SP-7 and SP-9 (28 % lower than HIP), as those stockpiles were turned 4 times per year, and therefore endured more mechanical breakdown. Interestingly, SP-1 and SP-6, with only two turning events per year, exhibited higher TS values. Increased aeration led to TS values 21 % higher than in the original material, still increasing over time.

These results (obtained after two years of stockpiling) raise questions regarding the necessity of frequent active management for marginal TS improvements. SP-4, with no turning, exhibited a consistent increase in tensile strength over time, likely due to self-weight consolidation, where soil compression, caused by the stress imposed by its own weight produces large strains, and higher compaction rates [9], [23]. SP-4 ultimately achieved the highest tensile strength with minimal intervention, suggesting that passive ripening may be the most efficient strategy if TS is the only property of interest.

Finally, tensile strength tests were conducted on samples compacted to 95% of their Proctor density. These results aligned more closely with the hypotheses presented at the beginning of this thesis. Specifically, increased aeration led to greater compactability in SP-7 and SP-9, which in turn, led to higher TS values. This outcome follows from the direct correlation between compaction rate and tensile strength [92], [113] (see section 2.1.2).

Upon application, SP-9 will therefore show the largest TS, as the benefits of higher compactability exceed the drawback of a lower inherent tensile strength. This is evidenced when comparing TS values between SP-9 (lowest inherent TS) with SP-4 (highest inherent TS and lowest Proctor density) in Figure 4.3.

A complex relationship between stockpile management, ripening time, and tensile strength was therefore observed. While frequent turning may reduce tensile strength in isolation, its positive effects on compactability — and thus TS under applied conditions — make it beneficial in practical applications such as dike construction.

5.2. Crack Formation

Crack formation results - unlike tensile strength - were influenced by drying conditions (see sections 2.3.2 to 2.3.6). Because of this, a higher degree of uncertainty was expected. This was primarily seen in the large variability between replicates of samples SP-4 09/24, SP-9 09/24, SP-6 09/24, and SP-7 03/25 (Figures 4.4, 4.5, and 4.7). The replicates of SP-9 09/24 and SP-7 03/25 were dried in separate boxes, and the differences in drying environments likely contributed to the variability. SP-4 09/24 and SP-6 09/24 replicates, however, were dried in the same environment, but still exhibited a large variability. Varying mold surface texture could also explain the observed behavior [100]. Although molds were reused between tests and manufactured using the same 3D printer, further investigation is warranted, as the printing process can introduce inconsistencies [64]. Additionally, ridges in the mold surface could have been filled with material from previous tests. Ideally, a more homogeneous material, such as glass, would have been used.

Inconsistencies were also observed between stockpiles at different ripening periods. Specifically, samples from September 2024 behaved differently from adjacent periods (see SP-1 and SP-4 from September 2024 in Figure 4.7). This indicates an event influencing all stockpiles at that time, such as seasonal variability or weather conditions prior to sampling. A prolonged dry period, for example, slows down the development of soil cohesion, as fewer clay particles are able to bond [46], and the continuous drying leads to widespread cracking in the soil. However, because all September 2024 samples were tested simultaneously - thus under identical drying conditions - the laboratory conditions could have also played a role in the anomalous behavior. That is, since all September 2024 samples displayed a result inconsistent with other time periods, the higher relative humidity in the lab at the time (see Table 4.1, SP-7 09/24) likely played a role. However, a higher RH is expected to increase crack width [116], but an opposite trend was observed in the results. Furthermore, RH has been observed to strongly correlate with water content at crack initiation [115], a trend which was not observed in the analyzed samples (see Table 4.1).

The stockpile materials most affected by the anomalous behavior (enhanced number of cracks, lower average crack width) were SP-1 and SP-4, which had different management techniques. SP-4 specifically, exhibited this behavior with the greatest intensity. A mistake was made during sample preparation, which resulted in an initial water content of approximately 120 % dw, instead of 90 % dw. This mistake likely influenced the result, as higher initial water content is linked to an increase in number of cracks [100]. This anomalous behavior was not observed in the Atterberg limits, tensile strength, or shrinkage measurements from this thesis. Drying conditions, as previously mentioned, also possibly influenced the results. Both SP-1 09/24 and SP-4 09/24 were dried in the same box, which which may have been overtly influenced by a draft from the ventilation system. However, this explanation is inconsistent with other results, since samples dried in the same location did not display similar behavior. To exclude seasonal variability as a potential cause, an additional test was conducted on an SP-4 sample from September 2023. Its results differed from SP-4 09/24, and were instead consistent with the other time periods. This discrepancy also can't be attributed to weather conditions prior to sampling, as both samples experienced a prolonged dry period before sampling, with similar temperature ranges and no recorded rainfall in the preceding two weeks. As a result, it was difficult to define a cause for the behavior found in the September 2024 samples.

As the onset of cracking is governed by the tensile resistance of the soil, a relationship between cracking and tensile strength was expected. Previous studies on the topic, however, are limited, and show ambiguous results. In some of them, higher tensile strength has been observed to lead to narrower

and fewer cracks [89], [93], although in those cases, higher tensile strength values were achieved through the introduction of natural fibers. This likely had an additional effect on cracking besides through increased tensile strength. This contrasts with the expected relationship, where higher tensile strength would concentrate failure into fewer, wider cracks. This relation has been observed experimentally in other studies [99], [119], where tensile strength was increased through a higher sample compaction rate.

Tensile strength variation in the crack formation tests conducted in this thesis, however, did not originate from fiber reinforcement or increased compaction rates. This made assessing a potential relationship more challenging, due to the lack of comparable studies. This was further exacerbated by the relative small variation in tensile strength values. Crack formation results were likely more influenced by shrinkage rather than tensile strength. This is supported by the stabilized shrinkage behavior seen in later samples (Figure 4.11), and the fact that all stockpiled material showed crack widths and CIF values well below those observed in the original material, consistent with COLE results. This trend is illustrated in Figure 4.6.

Cracking was also examined in relation to the measured Atterberg limits. Specifically, the relationship between the plasticity index and crack width, as previously studied by [94]. A higher plasticity index was found to correlate with increased CIF values and greater average crack widths.

However, no consistent relationship emerged in this thesis when assessing the plasticity indexes, CIFs and average crack widths (Table 4.4). The highest crack width was indeed observed in the sample with the highest plasticity index (SP-6 03/25), but SP-7, with the lowest plasticity index, still showed wide cracks. Similarly, an opposite trend to Tang et al. [94] was presented by SP-9, which had the highest CIF, despite a plasticity index comparable to other stockpiles.

Overall, crack formation experiments showed that sediment ripening greatly benefits its cracking characteristics. After two years of stockpiling, CIF decreased by 30 - 60 % and crack width by 40 - 70 % compared to the original material. No consistent pattern was observed between different stockpiling techniques, and only samples at a late stage of ripening were considered. The only tested sample from an earlier stage was SP-4 from September 2023, which exhibited wider cracks than in later periods. If the anomalous result from September 2024 is taken out, SP-4 does show a consistent decrease in the crack width and a stable CIF, which is consistent with the decrease in shrinkage observed in the same period.

This analysis however, neglects the effect that different turning rates have on compactability. Stockpiles turned more frequently exhibit higher Proctor densities (see Appendix B), which can affect cracking behavior. Upon application, the material will have a higher tensile strength, which would decrease crack formation [99], [119]. Further testing on compacted samples from different stockpiles is necessary to confirm this effect.

5.3. Atterberg Limits

Atterberg limit tests were performed on samples from March 2025, while only liquid limits were determined for March 2024 samples. For the September 2024 samples, as well as the plastic limits of the March 2024 samples, data was obtained from the S2S project, that had been obtained by a different operator . This distinction is noted due to the uncertainty stemming from the operator dependent nature of the Atterberg Limits test [45]. Despite potential differences, the datasets are consistent with each other, as seen in Figure 4.9.

None of the analyzed samples were deemed suitable for use as dike cover material based on their erosion resistance classification. This is consistent with the original assessment by the port authority, which had ruled out use of the dredged material in dike covers due to the contaminant inventory. Instead, the original intent was to use it in the dike core, with a 30 cm cover of clean clayey soil. Different criteria are imposed for core material. In this context, the critical property is the material's shape retention capability, which is a function of the available water content [95]. This result was expected, as these standards are developed for soils with a much higher clay content than the METHA material. Soils with a lower clay content have been observed to have reduced erosion resistance [110].

The water content upon application (i.e. when the dike is constructed with the material) follows from both the optimum water content by dry weight (given by the Proctor test), as well as the maximum water content by dry weight (given by the consistency index). All samples for which Proctor density was determined present a reasonable range of values based on Dutch standards, as seen in Table 4.3. Different requirements are imposed in Germany, where the material originates (Table 2.2). These requirements are based on total organic carbon (TOC), plasticity index, and the liquidity index. TOC was not measured for this thesis, but data from the S2S project confirm values below 9 %, at 3.0 wt % . Table 4.2 shows all samples have a plasticity index above 15. Finally, Table 4.3 presents reasonable values for a maximum water content upon application based on the liquidity index, ranging from 40 % to 70 %. Therefore, given compliance with environmental regulations, the material is suitable to be used as core material for the construction of a dike.

5.4. Coefficient of Linear Extensibility

COLE tests were carried out to asses the shrinkage response of the material to desiccation. The results showed that, after two years of ripening, shrinkage was 30-60% lower than in the original material. COLE values across the dataset were already lower than those of the HIP material just three months after stockpiling, decreasing further over time. By the end of the investigated period, COLE appeared to have stabilized, showing only a small variation between March 2024 and March 2025 results. SP-4 was the exception, as it exhibited a decrease of 50% over the same period. This suggests the possibility that SP-4 has not stabilized, due to the reduced aeration and de-watering from not being turned. This finding supports the assumption that ripening is largely complete after two years in the turned stockpiles, due to the increased aeration. Oing, Gröngröft, and Eschenbach [66] reported significant COLE reductions within one year of stockpiling, albeit on a smaller experimental scale than in the stockpiles investigated in thesis. Quantitatively, the study reported COLE values 20-80% lower than those of the original unripened material [66]. The same study also suggested that a single intense drying cycle is sufficient to stabilize shrinking. The stabilized COLE measured after two years of ripening in this thesis reinforces that conclusion.

5.5. Limitations

For the tensile strength test, the UCS machine was equipped with a load cell (pictured in Figure 3.7). The sensitivity of this load cell was not originally put into question, as the device had been calibrated and used in previous experiments. However, those experiments involved highly compacted samples that failed under relatively high loads. In contrast, the samples used in this study were compacted to lower densities, resulting in failure at significantly lower loads. A load cell with a higher sensitivity would have therefore been more appropriate. Unfortunately, this was only investigated after a majority of the tests had already been carried out. The load cell used had a maximum capacity of 3000 N, yielding a sensitivity of around $\pm$ 1.5 N (3 N total resolution). A comparison of measurements using different load cells is presented in Appendix C. Despite this limitation, the tensile strength results were consistent across replicates (Table C.1), suggesting reliability within the bounds of the equipment's precision. Nonetheless, the sensitivity used was at the edge of acceptable limits, and the use of a higher-resolution load cell is strongly recommended for future studies.

In addition, some tensile strength results did not yield good fits for linear interpolation. This raised concerns about the validity of using the Brazilian splitting disc method - a method devised for high strength brittle material - for low strength, ductile material. Although the feasibility of using it in such samples has been studied (see Gaspar and Jacobsz [25]), and a methodology for accurately measuring tensile strength recommended, a direct method for measuring tensile strength (in combination with the BTS test) would have been nonetheless preferable.

Another limitation comes from the sample preparation. As discussed in section 3.1.1, the samples were sieved to a size of 4 millimeters, according to the standard for the BTS test [5]. An appropriate grain size for the crack formation test, however, was not initially investigated. Common methodology for such tests is to sieve the sample to two millimeters, in order to improve replicability [91].

Common methodology also recommends two other standards for crack formation tests: to have an

initial moisture content of 1.5 times the liquid limit, and allowing the sample to rest for 24 hours before testing [90]. Initial tests done for this thesis had a much higher water content, around 2 times the liquid limit, but as the available time was short, and these samples took over two weeks to dry, a decision was made to have an initial water content of 90%. The METHA material has a very high liquid limit, which is why such a high water content still does not satisfy the recommended 1.5 threshold. As samples rested in the mold for a long period of time, and therefore the moisture content should equilibrate before any cracking occurs, letting samples dry for a day was also omitted. However, given no time-constraint, both of these steps should have been followed.

Finally, environmental conditions introduced further uncertainty. As outlined in the literature review, uncontrolled or volatile ambient conditions can negatively affect test outcomes. Ideally, all of the tests would have been carried out in an environmental chamber, with controlled temperature and relative humidity. Unfortunately, such a facility would not have been available in the lab during the period of this thesis, and setting up the test in a temperature controlled room, with a humidity sensor taking measurements was taken as a compromise.

6

Conclusions

This thesis investigated the effects of ripening on the mechanical properties of dredged material. It was conducted as part of the larger S2S project which seeks to understand and model the transformation of initially contaminated dredged material into a well-aerated soil like material under a stockpiling regime.

To achieve this, several research areas were defined, including the evaluation of soil stability indices, the development of geochemical models, and characterization of the material's chemical, physical, and biological properties. Focusing on the last research topic, a series of experiments were conducted in this thesis to measure key physical and mechanical properties for assessing the suitability of the material to be used in dike construction. The investigated properties include soil tensile strength, crack formation, shrinkage behavior, and the Atterberg limits.

The aim of this thesis was then to examine how these properties evolved throughout the ripening process, and analyze how different stockpiling techniques influence the material's properties. This was used as input to determine a preliminary recommendation of the best practice for future handling of dredged material, from the standpoint of tensile strength and crack formation.

Based on the research questions formulated in chapter 1, the following results were found:

1. **How does soil tensile strength and crack formation evolve during the ripening procedure?**

Stockpiling alone, thus without the influence of active management, was found to be beneficial to the material's tensile strength. The de-watering and aeration processes that occur in the field increased the material's bulk density, and enabled soil structure formation (among other processes), that in turn benefit tensile strength. Sediments in SP-4 (control) exhibited a 12% increase in TS after one year, and a 70% increase after two years, compared to the the original material. This trend was not observed to have stabilized, and tensile strength is therefore expected to keep increasing with additional stockpiling time. This was measured at a constant compaction level equivalent to the Proctor density of the original HIP material.

Compactability, however, also increased throughout ripening, which further benefits tensile strength of the dredged material upon application. When tensile strength was tested at 95% of the ripened material's Proctor density, an increase of 270 % was observed after 1.5 years of ripening.

In contrast, no consistent pattern was identified in the crack formation behavior. Samples showed varying CIF, width, and number of cracks throughout the ripening period. However, an anomalous result was observed in samples from September 2024, when these results were excluded, SP-4 (control) exhibited a decrease in crack width accompanied by an increase in crack number, a trend consistent with the reduced shrinkage measured in the stockpile.

More importantly, compared with the original material, CIF and crack width in the stockpiled material were consistently lower. This behavior was likely caused by the decrease in the shrinkage, rather than the increase in tensile strength. This is supported by COLE results, which displayed a considerable reduction in shrinkage behavior at the end of the ripening period.

In general, further crack formation tests are necessary, and the methodology developed further to reduce uncertainty. Specifically, a more reliable analysis would have been possible if tests were conducted in a controlled environment.

2. **How do different stockpile management procedures affect crack formation and tensile strength of the material?**

It was initially hypothesized that a higher turning frequency would be beneficial to the tensile strength of the material, given that increased aeration tends to reduce shrinkage and improve compactability. However, the results showed an opposite trend. Stockpiles with the highest turning frequencies exhibited a decrease from the original material of around 30%, consistent throughout the investigated period. In contrast, SP-4, with no turning, exhibited an increase of up to 70% after two years. Intermediate behavior was exhibited by SP-1 and SP-6, which underwent two turning events per year, and showed an increase of around 30 %.

These results can be attributed to the mechanical breakdown of the soil structure during turning, which reduces the stability of the soil. Notably, this was only observed after a few turning events, and tensile strength values were highest after one turning event. In those stockpiles, tensile strength was found to be approximately 105 % higher than the original material, likely due to the enhanced aeration provided by turning, without the significant structural breakdown caused by repeated turning events.

Compactability, in contrast, was found to improve with increased turning frequency. When tested at 95% of their Proctor density, samples from stockpiles with a higher turning frequency (4x/year) exhibited the highest tensile strength. This result was expected, as higher compactions lead to higher tensile strength. SP-9 - with the highest Proctor density - exhibited a tensile strength 430% higher than the original material.

A relation between the crack formation behavior and stockpile management techniques was not as clear. SP-6 and SP-7 consistently showed the smallest number of cracks, with the largest average width. This indicates a higher resistance to cracking, while the lowest resistance was seen in SP-9. SP-1 and SP-4 show a similar pattern to SP-6 and SP-7, but at a smaller magnitude. Both displayed a discrepant result in the September 2024 time series, however, suggesting another variable may have influenced their crack formation characteristics. In general, however, all stockpiles displayed a reduced cracking behavior when compared to the original material.

3. **Are the ripened METHA material physical properties sufficiently evolved for use in dike construction?**

Based on the answers found for the previous research questions, the ripening process significantly improves the suitability of dredged material for use in dike construction. Tensile strength increases over time, although care needs to be taken with the decision on stockpiling techniques. Overall, a higher turning rate appears to be best, as enhanced compactability greatly benefits tensile strength upon application.

Shrinkage also decreases significantly through ripening, which was likely the reason for the reduction observed in crack formation behavior. Although the Atterberg limits render the material unsuitable to be used as a cover layer, due to insufficient erosion resistance, it was found to be suitable as core material. For the additional regulatory criteria, samples fulfilled the requirements imposed under Dutch standards. Specifically, a sand content below 40 wt % and an OM content below 5 % dw was observed in all samples. Under German standards, the material fulfilled requirements for the plasticity index ($I_P \geq 15$) and for the TOC ($\leq 9\text{wt}\%$), which means it is suitable for use in dike construction, provided the material also meets contaminant leaching criteria.

6.1. Recommendations for Future Research

Some of the recommendations for future research were already highlighted in section 5.5, as they are directly related to limitations in the experiments conducted in this thesis. In short, the following improvements for the tensile strength and crack formation tests methodology are recommended:

- A more sensitive load cell for BTS tests (500N maximum capacity).

- Further tensile strength testing with a direct method, to validate results.
- Sieving samples to 2mm instead of 4mm for both tests.
- Crack formation samples with initial moisture content of at least 1.5 times the liquid limit, and allowing them to rest for 24 hours before test.
- Crack formation tests in a temperature and humidity controlled chamber.

A promising topic to branch out the researched conducted by the S2S project is to conduct fracture toughness experiments. Desiccation cracks are a result of tensile stress, but the propagation of these cracks was not investigated in this thesis. Researching fracture toughness would lead to better understanding of the boundary between the formation of short or long cracks upon application in dikes.

Additionally, as shear strength plays a major role in crack formation in the field (section 2.3.1), its investigation would add another layer of understanding for the S2S project.

Additional research needs to be conducted on crack formation in the field. Although the experiments carried out in this thesis - with some adjustments - should provide insights on the stockpiled material's propensity to crack, it is unknown how these potential results would materialize in real-life applications. This can be potentially tackled by further experiments meant to investigate different aspects in field conditions. For example, the influence of aggregate size on tensile strength and crack formation (this would entail tests with larger samples). Stockpiles currently have a wide range of aggregate size, and the influence of the larger ones was not investigated due to the small size of tested specimens. Another area of interest is the influence of the short to middle term stockpile condition prior to sampling, given by weather patterns. Finally, the moisture content at cracking, which was briefly tackled in this thesis, would have been an interesting aspect to investigate throughout ripening.

Additionally, crack formation tests can be conducted on samples of different compactions. As different materials yielded a range of Proctor densities, it would be more representative to field conditions to test sample cracking behavior when compacted to 95 % of their Proctor density. Tian et al. [99] already reported that varying compaction rates influence the final crack patterns.

Finally, another interesting are to expand the S2S research horizon are the methods available for crack remediation. An example is doing this through microbially induced calcite precipitation. Or alternatively, investigating the self-healing characteristic of the soil through re-wetting.

References

[1] Royal Netherlands Meteorological Institute (KNMI). *KNMI'14 Climate Scenarios for the Netherlands: Revised Edition 2015*. Tech. rep. Royal Netherlands Meteorological Institute (KNMI), 2015. URL: https://www.climatescenarios.nl/.

[2] Muhammad Abid and Rattan Lal. "Tillage and drainage impact on soil quality: II. Tensile strength of aggregates, moisture retention and water infiltration". In: *Soil and Tillage research* 103.2 (2009), pp. 364–372.

[3] Nikeh Booister Alex Hekman. *Ruimte voor de toekomst: Flexibel invullen van investeringsopgaven om effecten van zeespiegelstijging in de toekomst te kunnen opvangen*. Tech. rep. Sweco, 2025. URL: https://www.omgevingsweb.nl/wp-content/uploads/po-assets/393142.pdf.

[4] Sandra Arndt and Douglas Edward LaRowe. "Organic matter degradation and preservation". In: *Encyclopedia of Geochemistry*. Springer, 2018, pp. 1–6.

[5] ASTM International. *Standard Test Method for Splitting Tensile Strength of Intact Rock Core Specimens with Flat Loading Platens*. https://store.astm.org/d3967-23.html. ASTM D3967-23. West Conshohocken, PA: ASTM International, 2023.

[6] Dewi Le Bars, Sybren Drijfhout, and Hylke De Vries. "A high-end sea level rise probabilistic projection including rapid Antarctic ice sheet mass loss". In: *Environmental Research Letters* 12.4 (Mar. 2017), p. 044013. DOI: 10.1088/1748-9326/aa6512. URL: https://doi.org/10.1088/1748-9326/aa6512.

[7] AR Barzegar et al. "Tensile strength of dry, remoulded soils as affected by properties of the clay fraction". In: *Geoderma* 65.1-2 (1995), pp. 93–108.

[8] Marina Araújo Bavoso et al. "Soil tillage in grain and silage-producing areas and pasture: effect on tensile strength and aggregate friability". In: *Revista Brasileira de Ciência do Solo* 34 (2010), pp. 227–234.

[9] K Been and GC Sills. "Self-weight consolidation of soft soils: an experimental and theoretical study". In: *Geotechnique* 31.4 (1981), pp. 519–535.

[10] ZT Bieniawski and I Hawkes. "Suggested methods for determining tensile strength of rock materials". In: *International Journal of Rock Mechanics and Mining Sciences* 15.3 (1978), pp. 99–103.

[11] ET Brown. "Suggested methods for determining tensile strength of rock materials". In: *International Journal of Rock Mechanics and Mining Sciences and Geomechanics Abstracts* 15.3 (1978), pp. 99–103. ISSN: 0148-9062. DOI: https://doi.org/10.1016/0148-9062(78)90003-7. URL: https://www.sciencedirect.com/science/article/pii/0148906278900037.

[12] Hector Causarano. "Factors affecting the tensile strength of soil aggregates". In: *Soil and Tillage Research* 28.1 (1993), pp. 15–25.

[13] Controls Group. *Liquid Limit Cone Penetrometer Devices*. https://controls-group.com/product/liquid-limit-cone-penetrometer-devices-controls/. Product No. 22-T0029/E. Milan, Italy: Controls Group, 2023.

[14] Arturo E. Corte and Akira Higashi. *Experimental Research on Desiccation Cracks in Soil*. Tech. rep. CRREL Research Report 66. Accessed: 2025-05-29. U.S. Army Cold Regions Research and Engineering Laboratory, 1964. URL: https://usace.contentdm.oclc.org/digital/collection/p266001coll1/id/6153/.

[15] Susanga Costa, JK Kodikara, and B Shannon. "Salient factors controlling desiccation cracking of clay in laboratory experiments". In: *Géotechnique* 63.1 (2013), pp. 18–29.

[16] TA DelValls et al. "Chemical and ecotoxicological guidelines for managing disposal of dredged material". In: *TrAC Trends in Analytical Chemistry* 23.10-11 (2004), pp. 819–828.

[17] I Deniz Akin and WJ Likos. “Brazilian tensile strength testing of compacted clay”. In: *Geotechnical Testing Journal* 40.4 (2017), pp. 608–617.

[18] Heinz-Dieter Detzner. *Dredged Material Treatment and Disposal Facilities*. https://sednet.org/download/H-Detzner.pdf. Presentation at SedNet Special Session: Managing the Elbe Estuary, 9 October 2009. Oct. 2009.

[19] Heinz-Dieter Detzner, Andreas Netzband, and Rainer Knies. “Dredged Material Management in Hamburg”. In: *Terra et Aqua* 96 (2004), pp. 3–13. URL: https://www.iadc-dredging.com/wp-content/uploads/2017/03/article-dredged-material-management-in-hamburg-96-01.pdf.

[20] Ravi Diamond and Renjitha Mary Varghese. “Desiccation cracking behavior and strength characteristics of areca fiber-reinforced fine grained soils”. In: *Ground Improvement and Reinforced Soil Structures: Proceedings of Indian Geotechnical Conference 2020 Volume 2*. Springer. 2021, pp. 105–118.

[21] VP Efimov. “Brazilian tensile strength testing”. In: *Journal of Mining Science* 57.6 (2021), pp. 922–932.

[22] European Environment Agency. *Accelerating the Circular Economy in Europe – State and Outlook 2024*. EEA Report 13/2023. 2024. URL: https://www.eea.europa.eu/publications/accelerating-the-circular-economy.

[23] Mirko Felici et al. “PVD-assisted consolidation of dredged sediments in a CDF: design of the test field”. In: *Japanese Geotechnical Society Special Publication* 9.4 (2021), pp. 124–129.

[24] Delwyn G. Fredlund, Hendry Rahardjo, and Murray D. Fredlund. *Unsaturated Soil Mechanics in Engineering Practice*. English. John Wiley & Sons, Incorporated, 2012, pp. 80–81, 108–118. ISBN: 9781118280515.

[25] TAV Gaspar and SW Jacobsz. “Brazilian tensile strength test conducted on ductile unsaturated soil samples”. In: *Geotechnical Testing Journal* 44.3 (2021), pp. 799–810.

[26] Julia Gebert. Personal communication from the project leader. 2025.

[27] Julia Gebert, Claire Chassagne, and Rob Comans. *Project Title: Sediment to Soil (S2S)*. Research proposal. 2022.

[28] Julia Gebert, Claire Chassagne, and Rob Comans. *Sediment to Soil (S2S)*. 2023. URL: https://www.tudelft.nl/citg/over-faculteit/afdelingen/geoscience-engineering/research/research-themes/research-not-related-to-themes/sediment-to-soil-s2s (visited on 08/04/2025).

[29] Julia Gebert and Alexander Groengroeft. “Long-term hydraulic behaviour and soil ripening processes in a dike constructed from dredged material”. In: *Journal of Soils and Sediments* 20 (2020), pp. 1793–1805.

[30] RJ. Glopper, AGM. Minten, and HJ. Winkels. *Chemical ripening of the soil in Zuidelijk Flevoland (in Dutch)*. Lelystad, Flevoland: Rijkswaterstaat, Directie Flevoland, 1992. ISBN: 9036910919.

[31] Colin William Gray and Robert Allbrook. “Relationships between shrinkage indices and soil properties in some New Zealand soils”. In: *Geoderma* 108.3-4 (2002), pp. 287–299.

[32] Marjolijn Haasnoot et al. “Adaptation to uncertain sea-level rise; how uncertainty in Antarctic mass-loss impacts the coastal adaptation strategy of the Netherlands”. In: *Environmental Research Letters* 15.3 (2020), p. 034007.

[33] Hamburg Port Authority. *Umgang mit Baggergut aus dem Hamburger Hafen – Teilbericht: Umlagerung von Baggergut nach Neßsand: 2023*. Tech. rep. Internal report on dredged material relocation for 2023. Hamburg, Germany: Hamburg Port Authority, Dec. 2024.

[34] J. Harmsen. “Bioremediation of polluted sediment: a matter of time or effort”. English. In: *Phytoremediation, wetlands, and sediments; the sixth international in situ and on-site bioremediation symposium, San Diega, California, June 4-7, 2001. Columbus OH (USA), Battelle, 2001. Vol.5*. Ed. by A. Leeson et al. 2001, pp. 279–287.

[35] JA Hin, LA Osté, and CA Schmidt. “Guidance document for sediment assessment: methods to determine to what extent the realization of water quality objectives of a water system is impeded by contaminated sediments”. In: *Dutch Ministry of Infrastructure and the Environment–DG Water* (2010).

[36] R Horn et al. “Pore rigidity as an undervalued process in soil structure development”. In: *Soil and Tillage Research* 245 (2025), p. 106280.

[37] Bin Huang et al. “Effects of soil particle size on the adsorption, distribution, and migration behaviors of heavy metal(loid)s in soil: a review”. In: *Environmental Science: Processes and Impacts* 22.8 (2020), pp. 1596–1615. DOI: 10.1039/D0EM00189A. URL: https://doi.org/10.1039/D0EM00189A.

[38] Zhen Huang et al. “Surface crack development rules and shear strength of compacted expansive soil due to dry–wet cycles”. In: *Geotechnical and Geological Engineering* 37 (2019), pp. 2647–2657.

[39] Zhengjun Huang et al. “Determining Tensile Strength of Rock by the Direct Tensile, Brazilian Splitting, and Three-Point Bending Methods: A Comparative Study”. In: *Advances in Civil Engineering* 2021.1 (2021), p. 5519230.

[40] S Imhoff, A Pires Da Silva, and A Dexter. “Factors contributing to the tensile strength and friability of Oxisols”. In: *Soil Science Society of America Journal* 66.5 (2002), pp. 1656–1661.

[41] International Organization for Standardization. *ISO 17892-12:2018: Geotechnical investigation and testing — Laboratory testing of soil — Part 12: Determination of liquid and plastic limits*. https://www.iso.org/standard/72017.html. ISO 17892-12:2018. Geneva, Switzerland: International Organization for Standardization, 2018.

[42] Jacob N Israelachvili. “Van der Waals Forces between Surfaces”. In: *Intermolecular and Surface Forces*. 3rd ed. Burlington, MA; Oxford, UK: Academic Press, 2011. Chap. 6.1, pp. 107–109. ISBN: 9780123919274.

[43] JL Justo and M Vasquez. “A model for capillary pressure in unsaturated granular soils within the pendular saturation regime”. In: *Unsaturated soils* (2010), pp. 151–156.

[44] B.L. Karihaloo. *Fracture Mechanics and Structural Concrete*. Concrete design and construction series. Longman Scientific & Technical, 1995. ISBN: 9780470249888. URL: https://books.google.nl/books?id=XX1tQgAACAAJ.

[45] Kamil Kayabali et al. “Determination of Atterberg limits using newly devised mud press machine”. In: *Journal of African Earth Sciences* 116 (2016), pp. 127–133.

[46] WD Kemper and RC Rosenau. “Soil cohesion as affected by time and water content”. In: *Soil Science Society of America Journal* 48.5 (1984), pp. 1001–1006.

[47] Alex Kirichek et al. “Sediment management in the Port of Rotterdam”. In: June 2018.

[48] Aram Harold Klaassen. “Surface charge characterization of gibbsite nanoparticles: An atomic force microscope study”. English. PhD Thesis - Research UT, graduation UT. Netherlands: University of Twente, Nov. 2020. ISBN: 978-90-365-5071-0. DOI: 10.3990/1.9789036550710.

[49] K Koller and A El Titi. “Techniques of soil tillage”. In: *Soil tillage in agroecosystems* (2003), pp. 1–25.

[50] J-M Konrad and R Ayad. “A idealized framework for the analysis of cohesive soils undergoing desiccation”. In: *Canadian Geotechnical Journal* 34.4 (1997), pp. 477–488.

[51] SK Kourkoulis, Ch F Markides, and PE Chatzistergos. “The Brazilian disc under parabolically varying load: theoretical and experimental study of the displacement field”. In: *International Journal of Solids and Structures* 49.7-8 (2012), pp. 959–972.

[52] LAGA. *Anforderungen an die stoffliche Verwertung von mineralischen Abfällen – Technische Regeln. Allgemeiner Teil, Teil II (TR Boden), Teil IV (Aschen aus Kohlekraftwerken)*. 2003. URL: https://www.bafg.de/SharedDocs/Downloads/DE/baggergut/LAGA_TR_Boden.pdf?__blob=publicationFile&v=1.

[53] G. Lagaly and I. Dékány. “Chapter 8 - Colloid Clay Science”. In: *Handbook of Clay Science*. Ed. by Faïza Bergaya and Gerhard Lagaly. Vol. 5. Developments in Clay Science. Elsevier, 2013, pp. 243–345. DOI: https://doi.org/10.1016/B978-0-08-098258-8.00010-9. URL: https://www.sciencedirect.com/science/article/pii/B9780080982588000109.

[54] M Ramasesha Lakshmikantha. “Experimental and theoretical analysis of cracking in drying soils”. In: (2009).

[55] MR Lakshmikantha, PC Prat, and A Ledesma. “Image analysis for the quantification of a developing crack network on a drying soil”. In: *Geotechnical Testing Journal* 32.6 (2009), pp. 505–515.

[56] MR Lakshmikantha, Pere C Prat, and Alberto Ledesma. “Boundary effects in the desiccation of soil layers with controlled environmental conditions”. In: *Geotechnical Testing Journal* 41.4 (2018), pp. 675–697.

[57] Jian Li et al. “Effect of discrete fibre reinforcement on soil tensile strength”. In: *Journal of Rock Mechanics and Geotechnical Engineering* 6.2 (2014), pp. 133–137.

[58] Hang Lin, Wei Xiong, and Qixiang Yan. “Three-dimensional effect of tensile strength in the standard Brazilian test considering contact length”. In: *Geotechnical Testing Journal* 39.1 (2016), pp. 137–143.

[59] Hui Liu. “Chapter 3 - Rail transit collaborative robot systems”. In: *Robot Systems for Rail Transit Applications*. Ed. by Hui Liu. Elsevier, 2020, pp. 89–141. ISBN: 978-0-12-822968-2. DOI: https://doi.org/10.1016/B978-0-12-822968-2.00003-6. URL: https://www.sciencedirect.com/science/article/pii/B9780128229682000036.

[60] Ning Lu, Bailin Wu, and Chee P Tan. “Tensile strength characteristics of unsaturated sands”. In: *Journal of Geotechnical and Geoenvironmental Engineering* 133.2 (2007), pp. 144–154.

[61] Ministry of Infrastructrure and Water Management. *Delta Programme 2025: Towards a new balance in the living environment: Room to live with water.* Sept. 2024. URL: https://english.deltaprogramma.nl/documents/2024/09/17/dp2025-complete-version.

[62] Peter H Morris, James Graham, and David J Williams. “Cracking in drying soils”. In: *Canadian Geotechnical Journal* 29.2 (1992), pp. 263–277.

[63] Ian Murray, Alessandro Tarantino, and Fernando Francescon. “A tensile strength apparatus with the facility to monitor negative pore-water pressure”. In: *Geotechnical Testing Journal* 42.5 (2019), pp. 1384–1401.

[64] Tuan D Ngo et al. “Additive manufacturing (3D printing): A review of materials, methods, applications and challenges”. In: *Composites Part B: Engineering* 143 (2018), pp. 172–196.

[65] Katja Oing, Alexander Gröngröft, and Annette Eschenbach. “Enhanced dewatering optimizes compactibility of processed dredged material”. In: *Journal of Soils and Sediments* 18.9 (2018), pp. 3020–3030.

[66] Katja Oing, Alexander Gröngröft, and Annette Eschenbach. “Ripening reduces the shrinkage of processed dredged material”. In: *Journal of Soils and Sediments* 20 (2019), pp. 571–583.

[67] DK Painuli et al. “Crack formation in a swell–shrink soil under various managements”. In: *Agricultural research* 6 (2017), pp. 66–72.

[68] PANAGOS Panagiotis et al. “The state of soil in Europe: a contribution of the JRC to the European Environment Agency’s Environment State and Outlook Report—SOER 2010”. In: (2012). URL: https://coilink.org/20.500.12592/f2kmjk.

[69] E Perfect, BD Kay, and AP Da Silva. “Influence of soil properties on the statistical characterization of dry aggregate strength”. In: *Soil Science Society of America Journal* 59.2 (1995), pp. 532–537.

[70] Hueckel Peron et al. “Fundamentals of desiccation cracking of fine-grained soils: experimental characterisation and mechanisms identification”. In: *Canadian Geotechnical Journal* 46.10 (2009), pp. 1177–1201.

[71] Stephan Peth et al. “Heavy soil loading its consequence for soil structure, strength, deformation of arable soils”. In: *Journal of Plant Nutrition and Soil Science* 169.6 (2006), pp. 775–783.

[72] Nicolas Poncelet and Bertrand François. “Effect of laboratory compaction mode, density and suction on the tensile strength of a lime-treated silty soil”. In: *Transportation Geotechnics* 34 (2022), p. 100763.

[73] L.J. Pons and I.S. Zonneveld. *Soil ripening and soil classification : initial soil formation of alluvial deposits with a classification of the resulting soils = Pedogenese initiale et classification des sols = Initiale Bodenbildung und Bodenklassifikation = Pedogenesis initial y clasificacion de los suelos*. English. Publication / International Institute for Land Reclamation and Improvement 13. Netherlands: Veenman, 1965.

[74] LJ Pons and WH Van der Molen. “Soil genesis under dewatering regimes during 1000 years of polder development”. In: *Soil Science* 116.3 (1973), pp. 228–235.

[75] Benjamin S Ponto and John C Berg. “Clay particle charging in apolar media”. In: *Applied Clay Science* 161 (2018), pp. 76–81.

[76] Tibi Puiu. *Direct measurement of Van der Waals force made for the first time*. Online at ZME Science. Accessed May 2025. July 2013. URL: https://www.zmescience.com/science/physics/direct-measurement-of-van-der-waals-force-made-for-the-first-time/.

[77] Anand J Puppala et al. “Effects of organic matter on physical, strength, and volume change properties of compost amended expansive clay”. In: *Journal of Geotechnical and Geoenvironmental Engineering* 133.11 (2007), pp. 1449–1461.

[78] Hasan Rahimi, Ebrahim Pazira, and Fuad Tajik. “Effect of soil organic matter, electrical conductivity and sodium adsorption ratio on tensile strength of aggregates”. In: *Soil and Tillage Research* 54.3-4 (2000), pp. 145–153.

[79] Henrich Röper. *Sediment Management Port of Hamburg*. https://rijkewaddenzee.nl/wp-content/uploads/2021/12/211007-Sediment-Solutions-HPA-WS.pdf. Presentation at Waddensea Sediment Solutions workshop, 07 October 2021. Oct. 2021.

[80] Fokke Saathoff, Stefan Cantré, and Zbigniew Sikora. “Application of dredged materials, coal combustion products and geosynthetics in dike construction”. In: *South Baltic Guideline* (2015).

[81] Mai Sawada, Yusuke Sumi, and Mamoru Mimura. “Measuring desiccation-induced tensile stress during cracking process”. In: *Soils and Foundations* 61.4 (2021), pp. 915–928.

[82] Helmar Schubert. “Tensile strength of agglomerates”. In: *Powder Technology* 11.2 (1975), pp. 107–119.

[83] Ronny Seidel, Ullrich Dettmann, and Bärbel Tiemeyer. “Reviewing and analyzing shrinkage of peat and other organic soils in relation to selected soil properties”. In: *Vadose Zone Journal* 22.5 (2023), e20264.

[84] Senators für Umwelt, Bau, Verkehr und Europa (Bremen). *Verwendung von Baggergut im Deichbau*. May 2008.

[85] DR Shiwakoti et al. “Influences of diatom microfossils on engineering properties of soils”. In: *Soils and Foundations* 42.3 (2002), pp. 1–17.

[86] SINGH, SP and Tack, Filip and Verloo, Marc. *Land disposal of heavy metal contaminated dredged sediments: a review of environmental aspects. Land Contamination Reclamation, 1998, 6, pp. 149-158.* eng.

[87] SR Stephens et al. “Changes in the leachability of metals from dredged canal sediments during drying and oxidation”. In: *Environmental Pollution* 114.3 (2001), pp. 407–413.

[88] Lujo Šuklje. *Rheological aspects of soil mechanics*. Wiley-Interscience London, 1969.

[89] Abu Taiyab, Nazmun Naher Islam, and Mokhlesur Rahman. “Desiccation characteristics and direct tension attributes of thin clayey soil containing discrete natural fibers”. In: *Soils and Rocks* 45 (2022), e2022074421.

[90] Chao-Sheng Tang et al. “Desiccation cracking of soils: A review of investigation approaches, underlying mechanisms, and influencing factors”. In: *Earth-Science Reviews* 216 (2021), p. 103586.

[91] Chao-Sheng Tang et al. “Effect of wetting-drying cycles on soil desiccation cracking behaviour”. In: *E3S Web of conferences*. Vol. 9. EDP Sciences. 2016, p. 12003.

[92] Chao-Sheng Tang et al. “Tensile strength of compacted clayey soil”. In: *Journal of Geotechnical and Geoenvironmental Engineering* 141.4 (2015), p. 04014122.

[93] Chao-Sheng Tang et al. “Tensile strength of fiber-reinforced soil”. In: *Journal of Materials in Civil Engineering* 28.7 (2016), p. 04016031.

[94] Chaosheng Tang et al. “Influencing factors of geometrical structure of surface shrinkage cracks in clayey soils”. In: *Engineering geology* 101.3-4 (2008), pp. 204–217.

[95] Technical Advisory Committee for Flood Defence in The Netherlands. *Technical Report: Clay for Dikes*. Tech. rep. Technical Report prepared under the responsibility of the project group TAW-B6. Delft, The Netherlands: The Road and Hydraulic Engineering Institute (DWW), Rijkswaterstaat, 1996.

[96] Karl Terzaghi, Ralph B Peck, and Gholamreza Mesri. *Soil mechanics in engineering practice*. John wiley & sons, 1996.

[97] E. Thoen et al., eds. *Landscapes or Seascapes? The history of the coastal environment in the North Sea area reconsidered*. English. Brepols 13. Corn Publication Series. Comparative Rural History of the North Sea Area, 2013.

[98] Djebbar Tiab and Erle C. Donaldson. “Chapter 9 - Effect of Stress on Reservoir Rock Properties”. In: *Petrophysics (Fourth Edition)*. Ed. by Djebbar Tiab and Erle C. Donaldson. Fourth Edition. Boston: Gulf Professional Publishing, 2016, pp. 483–582. ISBN: 978-0-12-803188-9. DOI: https://doi.org/10.1016/B978-0-12-803188-9.00009-7. URL: https://www.sciencedirect.com/science/article/pii/B9780128031889000097.

[99] Ben-Gang Tian et al. “Desiccation Cracking Behavior of a Clayey Soil with Different Compaction States”. In: *International Association for Engineering Geology and the Environment*. Springer, 2023, pp. 187–195.

[100] Roderick N Tollenaar. “Experimental investigation on the desiccation and fracturing of clay”. In: (2017).

[101] U.S. Department of Agriculture: Soil Conservation Service. *SCS National Engineering Handbook (NEH), section 16 — Chapter 6: Dikes*. Tech Report. May 1971. URL: https://irrigationtoolbox.com/NEH/Part624_Drainage/NEH%2016%20Chapter%206.pdf.

[102] Jos Van Alphen, Marjolijn Haasnoot, and Ferdinand Diermanse. “Uncertain accelerated sea-level rise, potential consequences, and adaptive strategies in the Netherlands”. In: *Water* 14.10 (2022), p. 1527.

[103] N. van Breemen and P. Buurman. *Soil formation.* English. Netherlands: Kluwer Academic Publishers, 1998, p. 21. ISBN: 9780792352631.

[104] Louis V Verchot et al. “Organic matter stabilization in soil aggregates: Understanding the biogeochemical mechanisms that determine the fate of carbon inputs in soils”. In: *Geoderma* 161.3-4 (2011), pp. 182–193.

[105] Johan Vermeulen et al. “Ripening of clayey dredged sediments during temporary upland disposal a bioremediation technique”. In: *Journal of soils and sediments* 3 (2003), pp. 49–59.

[106] Jun-Jie Wang et al. “Experimental study on fracture toughness and tensile strength of a clay”. In: *Engineering Geology* 94.1-2 (2007), pp. 65–75.

[107] Rong Wang et al. “Comparison of test methods for determining the tensile strength of soil and weak rocks”. In: *Frontiers in Earth Science* 10 (2022), p. 835851.

[108] Tao Wang et al. “Size effect on soil desiccation cracking”. In: *Journal of Rock Mechanics and Geotechnical Engineering* (2025).

[109] Xiang Wang et al. “Soil aggregation and the stabilization of organic carbon as affected by erosion and deposition”. In: *Soil Biology and Biochemistry* 72 (2014), pp. 55–65.

[110] Yung-Chieh Wang and Rui-Yang Hung. “Effects of sediment properties on the erosion resistance of natural cohesive soils in Taiwan”. In: *Catena* 223 (2023), p. 106950.

[111] Hui Wei et al. “High clay content accelerates the decomposition of fresh organic matter in artificial soils”. In: *Soil Biology and Biochemistry* 77 (2014), pp. 100–108.

[112] Shuoshuo Xu et al. “Mechanism, influencing factors and research methods for soil desiccation cracking: a review”. In: *European Journal of Environmental and Civil Engineering* 27.10 (2023), pp. 3091–3115.

[113] Chao Ye et al. “Effect of water content, bulk density, and aggregate size on mechanical characteristics of Aquults soil blocks and aggregates from subtropical China”. In: *Journal of soils and sediments* 17 (2017), pp. 210–219.

[114] F Zander et al. “Effects of organic matter degradation in cohesive sediment: linking sediment rheology to spatio-temporal patterns of organic matter degradability”. In: *Journal of Soils and Sediments* 22.11 (2022), pp. 2873–2882.

[115] Hao Zeng et al. “Coupling effects of interfacial friction and layer thickness on soil desiccation cracking behavior”. In: *Engineering Geology* 260 (2019), p. 105220.

[116] Hao Zeng et al. “Desiccation cracking of soil subjected to different environmental relative humidity conditions”. In: *Engineering Geology* 297 (2022), p. 106536.

[117] Haiquan Zhang. “Organic matter incorporation affects mechanical properties of soil aggregates”. In: *Soil and Tillage Research* 31.2-3 (1994), pp. 263–275.

[118] Yuping Zhang et al. “Effect of biochar on desiccation cracking characteristics of clayey soils”. In: *Geoderma* 364 (2020), p. 114182.

[119] Ya Zhao et al. “Development Characteristics and Mechanism of Crack in Expansive Soil under Wet–Dry Cycling”. In: *Applied Sciences* 14.15 (2024), p. 6499.

Declaration Use of Language Models

After the full thesis text was written, and with approval of the supervising committee, a large language model was used for editing purposes. This includes suggesting changes in the text for improved flow, grammar, and tone. The model had no influence on the content of this thesis.

A

Code Used for analysis of BTS tests.

```
import numpy as np
import matplotlib.pyplot as plt
import pandas as pd
import json
import os
import seaborn as sns
from scipy.optimize import curve_fit

#Define a function that takes as input the data, along with the measured parameters, and
#outputs a clean version of it, ready to be plotted


def BTS(initialthickness,initialdiameter,file_name,interval_,startthreshold,peakthreshold,
    time):
    #User inputs
    inthickness = initialthickness; #initial height before Brazillian [mm]
    indiam = initialdiameter; #initial diameter before Brazilian [mm]
    filename = file_name #Name of the file
    interval = interval_ # interval that peak tensile strength occurs in
    start_threshold = startthreshold #threshold that values should differ to indicate slope
        of increased load
    peak_treshold = peakthreshold #threshold that indicates how different values should be to
         say a maximum has been reached
    t = time #start time. Sometimes there is an increase before the start of the test, then
        the start time must be put ahead

    #Pre-processing
    inarea = np.pi*(indiam/2)**2; #Area [mm^2]
    involume = inarea*inthickness; #Volume [mm^3]

    # Import data
    databts = pd.read_csv(filename, delimiter = ';', skiprows = [0,2])
    databts.drop(['Unnamed:␣6'], axis = 1, inplace = True) #drop an useless column from the
        file
    bts_teststart = np.where(np.array(databts['Load␣[N]'].diff(periods=1)[1:]) >
        start_threshold)[0][t] #Start the test interpretation once a load increase is seen
    bts_testend = np.where(np.array(databts['Load␣[N]'].diff(periods=interval)[interval:]) <
        peak_treshold)[0][1] + interval + 20 #stop the test once the first peak has been
        reached

    #Sometimes a peak is seen before the start of the test, this loop clears that.
    n = 0
    condition = bts_teststart + interval +20
    while bts_testend < condition:
        n+=1
        bts_testend = np.where(np.array(databts['Load␣[N]'].diff(periods=interval)[interval
            :]) < peak_treshold)[0][n] + interval + 20
        if bts_testend > condition:
            break
```

```
    # Normalize the data to conditions at the start of the test.
    bts_time = databts['Time'][bts_teststart:bts_testend] - databts['Time'][bts_teststart]
    bts_force = databts['Load␣[N]'][bts_teststart:bts_testend] - databts['Load␣[N]'][
        bts_teststart]
    bts_disp = databts['Pos␣[mm]'][bts_teststart:bts_testend] - databts['Pos␣[mm]'][
        bts_teststart]

    # Calculations

    fail_index = bts_testend - interval - 20 #point at which the start of the first peak
        occured (approximately)
    fail_force = bts_force[databts['Load␣[N]'][fail_index:fail_index + interval].idxmax()] #
        Maximum load obeserved in the first peak
    fail_strain = databts['Pos␣[mm]'][databts['Pos␣[mm]'][fail_index:fail_index + interval].
        idxmax()]
    bts = fail_force * 2 / (np.pi * inthickness / 1000 * indiam / 1000) / 1000  # bts in kPa,
         based on equation from ASTM standard
    bts_tensile_stress = bts_force * 2 / (np.pi * inthickness / 1000 * indiam / 1000) / 1000
         # bts in kPa, applied throughout the load evolution
    bts_compressive_stress = bts_force * 2 / (np.pi * inthickness / 1000 * indiam / 1000) /
        1000  # bts in kPa
    strain_failure = bts_disp[fail_index] / indiam * 100  # strain at failure
    brazilian_modulus = fail_force / (strain_failure / 100)  # strain per load (NOT a real
        modulus)
    bts = fail_force * 2 / (np.pi * inthickness / 1000 * indiam / 1000) / 1000  # bts in kPa

    return bts_disp, indiam, bts_force, databts,fail_index, fail_force, strain_failure,
        inthickness,interval,brazilian_modulus, bts,filename,bts_time

#Use the function on the data and plot it, this is for tensile yield point method

testdata = BTS(initialthickness = 20.9,initialdiameter = 50,
               file_name = 'Raw␣data\SP4_3_0924_95_030725.csv', interval_ = 10,
               startthreshold = 0.2, peakthreshold = 0.002, time = 4)

first_n = 0  #Start of the linear loading phase
starting_n = 40 #How long the linear loading phase lasts
tempo = 1 #First occurence of the tensile yield, this should be adjusted to give the best
    match
xdata = np.array((testdata[0][first_n:starting_n] / testdata[1] * 100))

ydata =  np.array((testdata[2][first_n:starting_n]))

def stressStrain( x, *params ):
    s0, E, a = params                   # x is strain, s0 is linear-elastic strain limit, E is
         elastic modulus (stress/strain)
    return E*x

p0 = ( 0.01, 1e6, 0 )
popt, pcov = curve_fit( stressStrain, xdata, ydata, p0=p0 )
s0, E, a = popt

coef = np.polyfit(xdata,ydata,1)
poly1d_fn = np.poly1d(coef)

#fit a line through the first points, but that goes through all the data points
xfit = testdata[0]/testdata[1]*100;   yfit = poly1d_fn(xfit)
diffdf = pd.DataFrame(testdata[2])
diffdf['Line␣Fit'] = yfit
diffdf['Data_diff'] = diffdf['Load␣[N]'] - diffdf['Line␣Fit']
residuals = testdata[2] - (E * testdata[0] + 0)
above_inflection = np.where(np.abs(np.array(diffdf['Data_diff'])) > 0.25)
inflection_index = above_inflection[0][tempo]

# Plot data
xfit1 = testdata[0]/testdata[1]*100 - 0.3* (testdata[0]/testdata[1]*100) ;   yfit1 =
    poly1d_fn(xfit1)
plt.figure(figsize = (9,7))
plt.plot( testdata[0] / testdata[1] * 100, testdata[2], 'k-', label='Data')
plt.plot( xfit1, yfit1, 'b-', label='Tensile␣strength␣mobilized' )
```

```
#plt.axvline(testdata[0].iloc[inflection_index]/testdata[1] * 100, c = 'r', label = 'Tensile yield point')
plt.scatter(testdata[0].iloc[inflection_index]/testdata[1] * 100,testdata[2].iloc[inflection_index],c = 'r', edgecolor = 'k',
            linewidth = 1, alpha = 1, s = 100, label = 'Tensile yield point' )
plt.xlabel("Diametric strain (%)")
plt.ylabel("Load during Brazilian test (kPa)")
plt.title(f'Load evolution during brazilian test {testdata[11][9:-4]}')
plt.grid()
plt.legend()
plt.savefig(f'Plots/{testdata[11][9:-4]} load evolution tensile yield')
plt.show()

summary = {'File Name' : testdata[11], 'Thickness' :testdata[7],
             'Diameter' :testdata[1], 'Tensile failure load' :testdata[2].iloc[inflection_index]}

with open(f'Data Summaries/{testdata[11][9:-4]} load evolution tensile yield.txt', 'w') as file:
     file.write(json.dumps(summary))
print(summary)
```

B

Proctor Curves for September 2024 samples.

Proctor densities were determined by Nazeir Elnaker, as part of the S2S project. The data is presented in figure B.1.

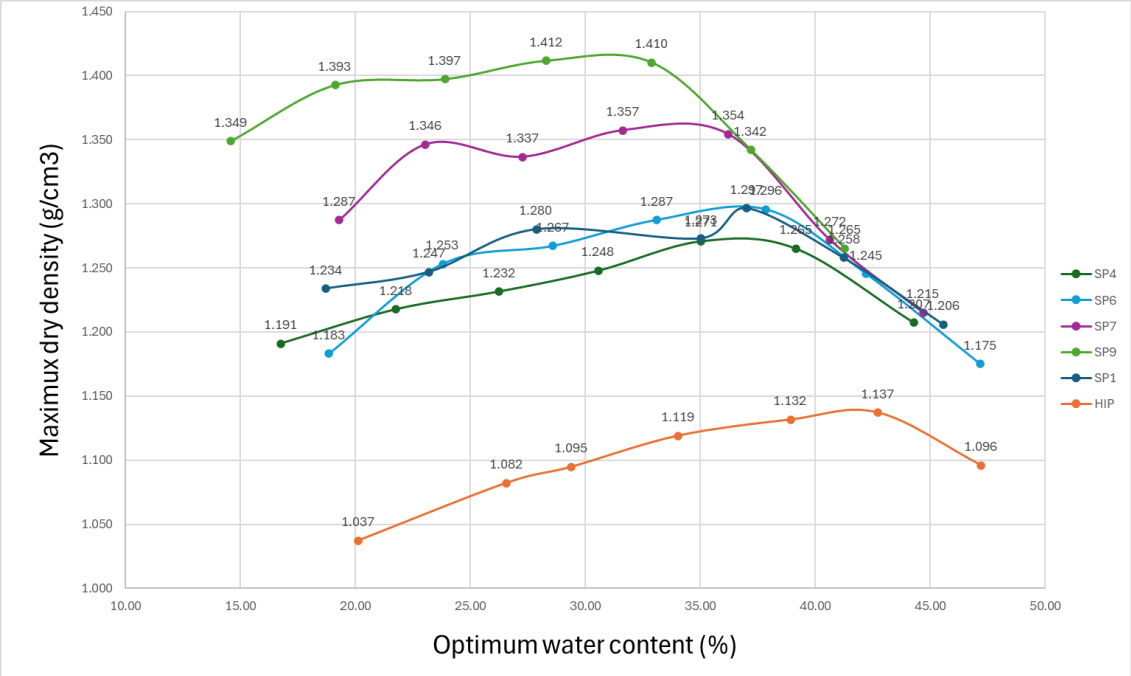

Figure B.1: Proctor Curves for stockpiles from September 2024.

C

Tensile Strength Data Evaluation and Validation

C.1. Comparison Between Tensile Strength Results for Different Load Cells

Tensile tests were conducted between different load cells, in order to determine the validity of the results.

Comparing the results presented in the Figures C.1, C.2, and C.3, the range of values is similar, but most importantly, the trend between stockpiles is consistent.

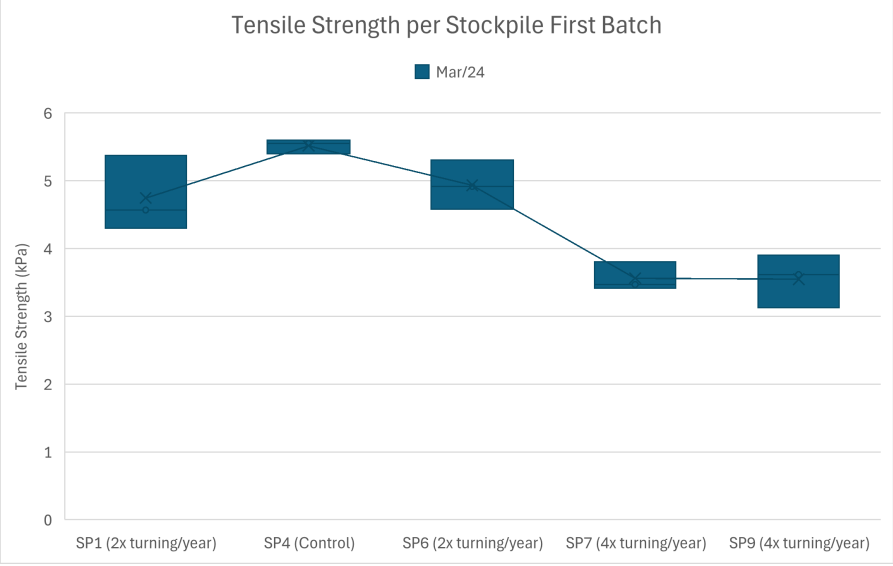

Figure C.1: Tensile strength results using the three kN load cell, first run of tests.

Comparing the results presented in the three figures, range of values is similar, but most importantly, the trend between stockpiles is consistent.

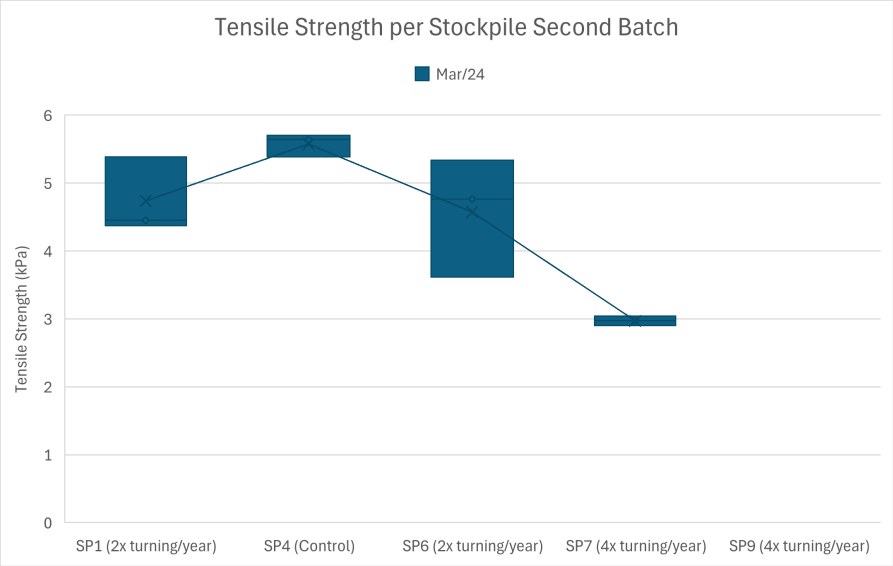

Figure C.2: Tensile strength results using the three kN load cell, second run of tests.

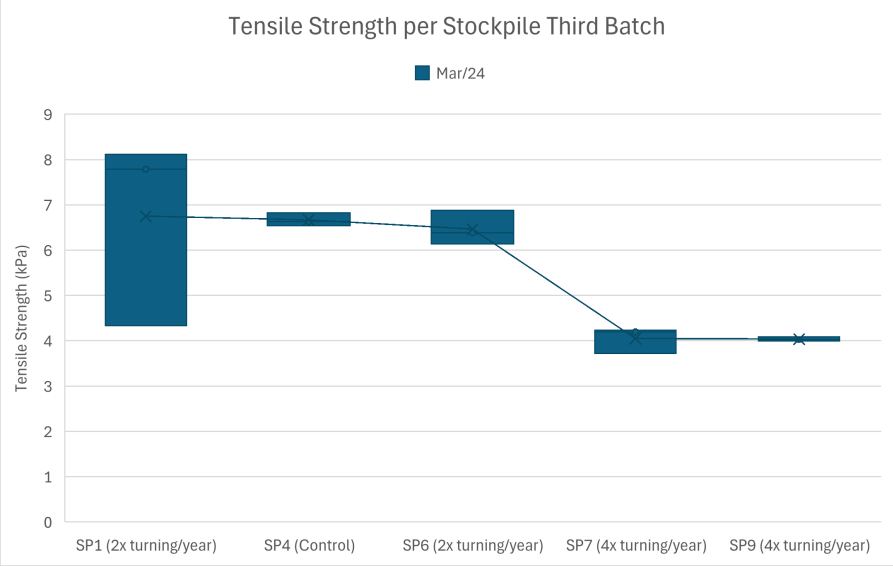

Figure C.3: Tensile strength results using the 500 N load cell.

C.2. Coefficient of Variation Results

Coefficient of Variation (CV) was calculated for each sample, following equation C.1.

$$CV = \frac{\sqrt{\frac{\sum (X-\mu)^2}{N}}}{\mu} \tag{C.1}$$

Where μ is the sample mean, X is an individual test value, and N is the number of tests conducted. The results are shown in table C.1.

Table C.1: Coefficient of Variation results.

Sample	CV (%)
SP1 03/24	9.64
SP4 03/24	1.44
SP6 03/24	5.65
SP7 03/24	5.61
SP9 03/24	8.99
SP1 09/24	0.89
SP4 09/24	0.79
SP6 09/24	10.52
SP7 09/24	4.81
SP9 09/24	3.14
SP1 03/25	1.39
SP4 03/25	1.49
SP6 03/25	4.87
SP7 03/25	5.61
SP9 03/25	8.08
SP1 95%	0.89
SP4 95%	1.88
SP6 95%	1.72
SP7 95%	4.66
SP9 95%	3.14
SP1 03/23	4.66
SP4 03/23	11.99
SP6 03/23	9.49
SP7 03/23	4.35
Mean	5.19

D

Fits used for determination of the liquid limits.

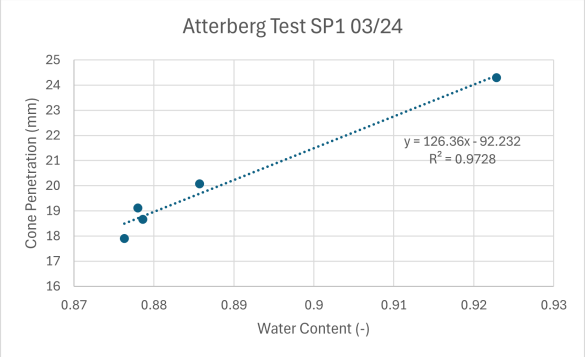

(a) SP1 03/24 liquid limit

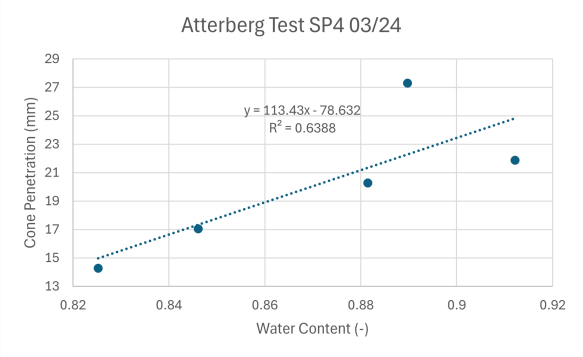

(b) SP4 03/24 liquid limit

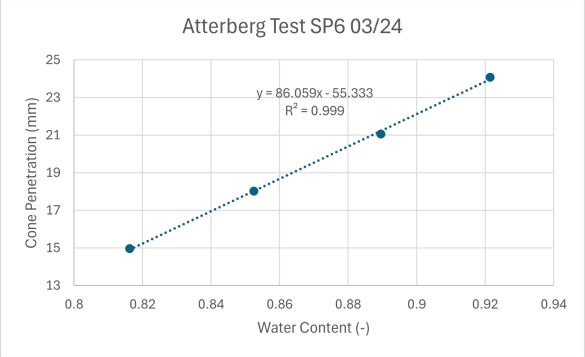

(c) SP6 03/24 liquid limit

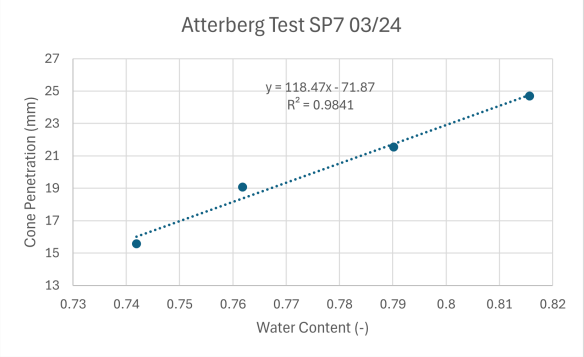

(d) SP7 03/24 liquid limit

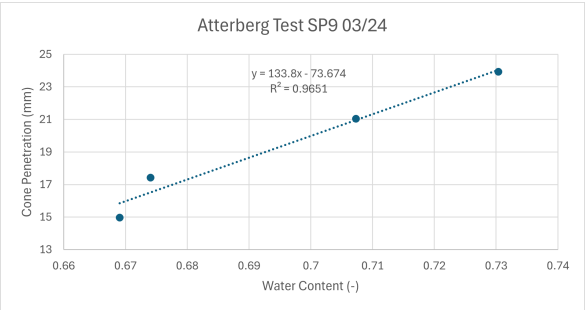

(a) SP9 03/24 liquid limit

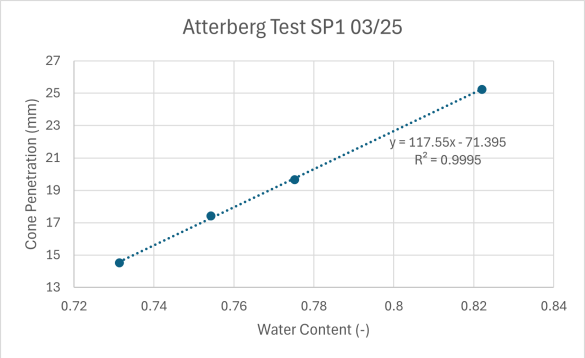

(b) SP1 03/25 liquid limit

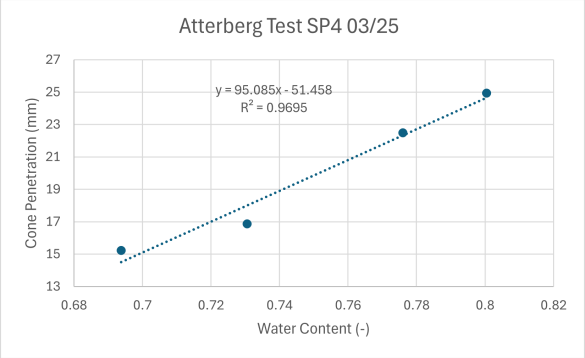

(c) SP4 03/25 liquid limit

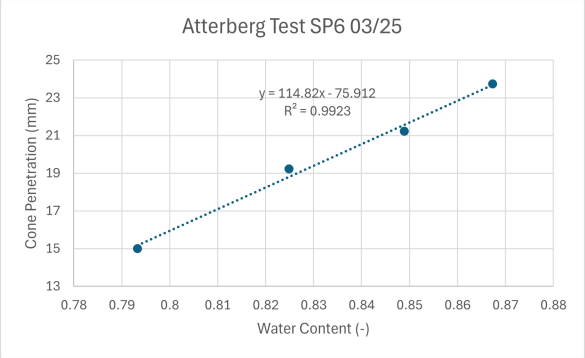

(d) SP6 03/25 liquid limit

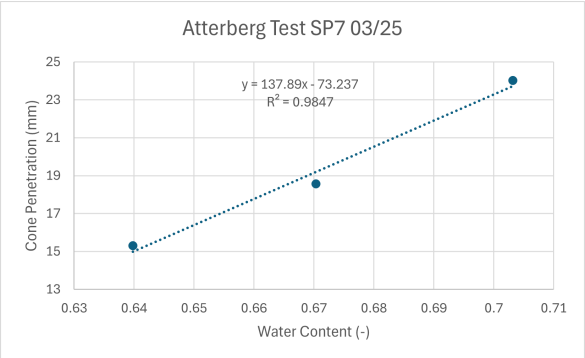

(e) SP7 03/25 liquid limit

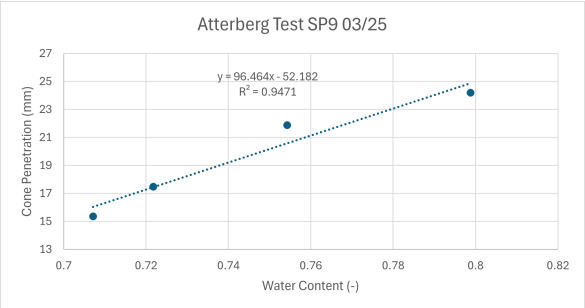

(f) SP9 03/25 liquid limit

E

Details on the METHA plant and stockpiling procedure.

Before de-watering takes place, dredged sediments are sorted and separated through the process shown in Figure E.1.

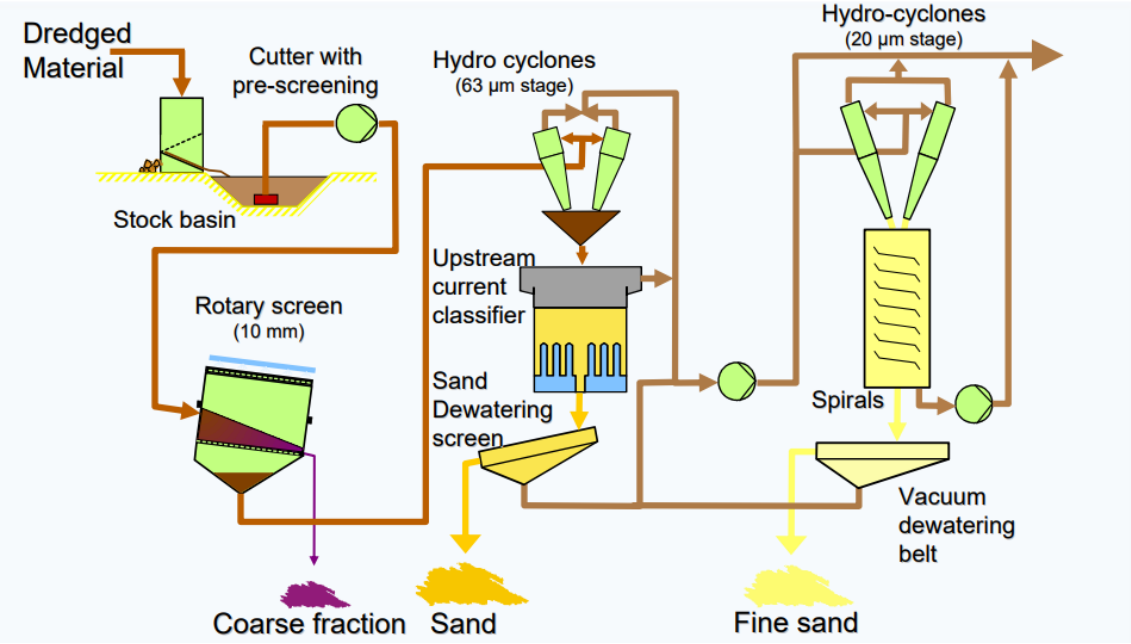

Figure E.1: Sorting and Separation process in the METHA plant [18].

After processing, the METHA material was stockpiled, with the configuration shown in Figure E.2.

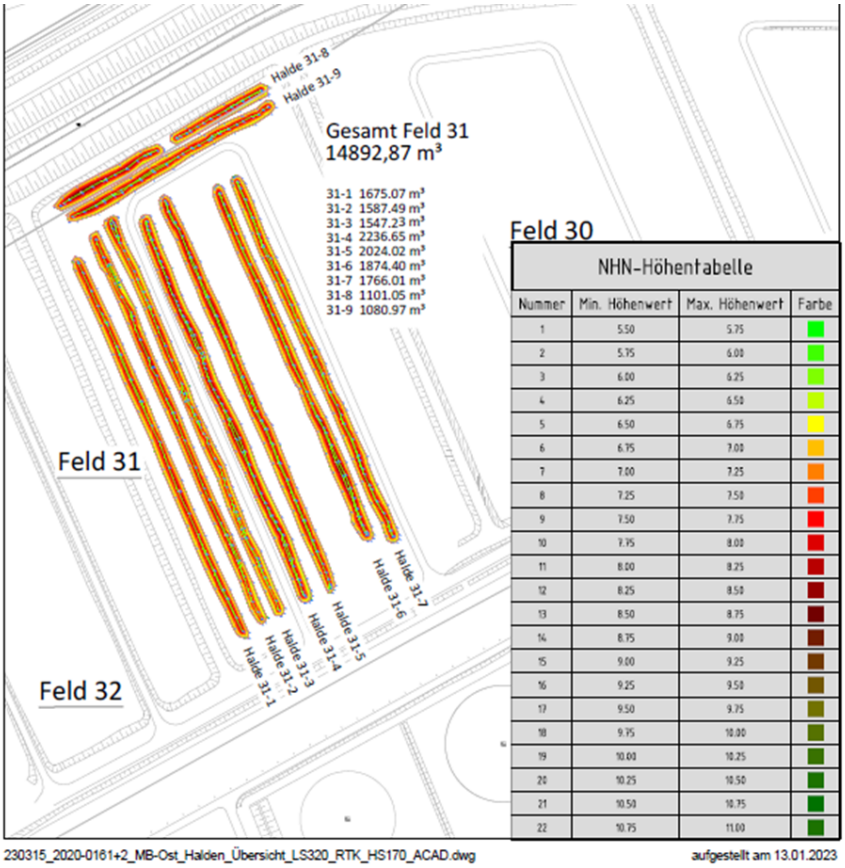

Figure E.2: Bird's eye view of de-watering fields Moorburg-Ost. Stockpile volumes in m^3.

Finally, sampling campaigns were planned in March and September of each year, right before a turning event. Turning was scheduled according to table E.1.

Table E.1: Original stockpile turning schedule. Green = Vegetation worked into stockpile upon turning. Orange = Vegetation + top 20 cm rooting zone removed before turning

#	Jan	Feb	Mar	Apr	May	Jun	Jul	Aug	Sep	Oct	Nov	Dec
1												
2	No stockpile turning, not considered further											
3												
4	No stockpile turning, Control											
5												
6												
7												
8												
9												

F

Raw Tensile Strength Data

Table F.1: Raw Tensile Strength Data

	Tensile Strength				
	Samples	Sample Diameter (mm)	Sample Height (mm)	Maximum Applied Load (N)	Tensile Strength (kPa)
	SP7_1	50	21	6.275816	3.805055765
SP7 03/24	SP7_2	50	20.5	5.497441	3.414419159
	SP7_3	50	21	5.720039	3.468085644
	SP6_1	50	21	7.551084	4.57825655
SP6 03/24	SP6_2	50	20.8	8.672689	5.308851247
	SP6_3	50	21	8.102552	4.912614105
	SP4_1	50	20.9	9.193997	5.601033758
SP4 03/24	SP4_2	50	21	9.158095	5.552594623
	SP4_3	50	21	8.899594	5.395864292
	SP9_1	50	21	6.432352	3.899964253
SP9 03/24	SP9_2	50	21	5.964178	3.616108229
	SP9_3	50	21	5.158519	3.127633516
	SP1_1	50	21	7.087219	4.297013092
SP1 03/24	SP1_2	50	21	8.863692	5.374096746
	SP1_3	50	21	7.532414	4.566936844
	SP1_1	50	21	10.456341	6.339727074
SP1 03/25	SP1_2	50	21	10.169118	6.165582463
	SP1_3	50	21	12.713911	7.708502025
	SP7_1	49.9	21	6.413681	3.896436815
SP7 03/25	SP7_2	49.95	20.7	5.615202	3.457320721
	SP7_3	50	20.7	6.231296	3.832817624
	SP6_1	50	20.8	9.402233	5.755430223
SP6 03/25					

Continued on next page

Table F.1: Raw Tensile Strength Data (Continued)

	Tensile Strength				
	Samples	Sample Diameter (mm)	Sample Height (mm)	Maximum Applied Load (N)	Tensile Strength (kPa)
	SP6_2	49.9	20.8	9.828759	6.028578616
	SP6_3	50	20.9	8.72726	5.316695
	SP4_1	50	20.9	12.000162	7.310564977
SP4 03/25	SP4_2	50	20.9	12.066224	7.350810312
	SP4_3	50.2	21	11.66124	7.042094436
	SP9_1	50	20.7	4.984749	3.066077076
SP9 03/25	SP9_2	49.9	20.5	5.504622	3.425730685
	SP9_3	50	21	6.077632	3.684895905
	SP1_1	50	21.1	10.273954	6.199622992
SP1 09/24	SP1_2	50	21	10.301241	6.245689239
	SP1_3	50	21	10.482191	6.355400046
	SP7_1	50	21	5.15421	3.125020949
SP7 09/24	SP7_2	50	20.7	5.000547	3.075794293
	SP7_3	50	20.6	5.596533	3.459090839
	SP6_1	50	20.8	8.498919	5.202480653
SP6 09/24	SP6_2	50	20.8	7.115941	4.35591225
	SP6_3	50	20.9	9.212666	5.612407016
	SP4_1	50	21	10.048484	6.092441521
SP4 09/24	SP4_2	50	20.9	10.081515	6.141714626
	SP4_3	50	20.9	9.899129	6.030604068
	SP9_1	49.8	20.7	6.228423	3.846436211
SP9 09/24	SP9_2	50	20.8	6.043165	3.69922916
	SP9_3	49.9	20.6	6.521391	4.038802317
	HIP 1	50	20.9	8.964219	5.461051731
HIP	HIP 2	50	20.9	8.531949	5.19771046
	HIP 3	50	20.9	6.771274	4.125097524
	SP7_1	50	21	4.785129	2.901245462
SP7 03/24	SP7_2	50	20.5	4.897146	3.04158046
	SP7_3	50	21	4.90289	2.972644491
	SP6_1	50	21	5.96705	3.617849536
SP6 03/24	SP6_2	50	21	7.859849	4.765462173
	SP6_3	50	21	8.803375	5.337526275
	SP4_1	50	21	9.30027	5.638795972
SP4 03/24	SP4_2	50	21	9.402234	5.700617208
	SP4_3	50	21	8.88236	5.385415239

Continued on next page

Table F.1: Raw Tensile Strength Data (Continued)

Tensile Strength

	Samples	Sample Diameter (mm)	Sample Height (mm)	Maximum Applied Load (N)	Tensile Strength (kPa)
	SP1_1	50	20.9	7.308381	4.452306075
SP1 03/24	SP1_2	50	21	8.886669	5.388027806
	SP1_3	50	21	7.210724	4.371894735
	SP7_1	50	20.9	17.69696	10.78108579
SP7 03/24	SP7_2	50	20.9	19.655037	11.97395711
	SP7_3	50	20.9	18.406515	11.21335061
	SP6_1	50	20.8	15.17565	9.289537354
SP6 03/24	SP6_2	50	20.8	16.111675	9.862510453
	SP6_3	50	20.8	18.9146	11.57827726
	SP4_1	50	20.9	8.362453	5.09445256
SP4 03/24	SP4_2	50	20.9	9.620535	5.860883064
	SP4_3	50	20.9	11.213172	6.831126322
	SP1_1	50	21	16.334468	9.90366219
SP1 03/24	SP1_2	50	21	17.38152	10.53849458
	SP1_3	50	21	15.512413	9.405246508
	SP1_1	50	21.1	10.273954	6.199622992
SP1 95 %	SP1_2	50	21	10.301241	6.245689239
	SP1_3	50	21	10.482191	6.355400046
	SP7_1	50	21	21.710907	13.16342159
SP7 95 %	SP7_2	50	20.7	23.689573	14.57125659
	SP7_3	50	20.6	21.32488	13.18042743
	SP6_1	50	20.8	35.717447	21.86387786
SP6 95 %	SP6_2	50	20.8	35.934358	21.99665655
	SP6_3	50	20.9	34.551277	21.0488288
	SP4_1	50	21	30.427035	18.44804961
SP4 95 %	SP4_2	50	20.9	31.525559	19.20554468
	SP4_3	50	20.9	30.207184	18.40238335
	SP9_1	49.8	20.7	6.228423	3.846436211
SP9 95 %	SP9_2	50	20.8	6.043165	3.69922916
	SP9_3	49.9	20.6	6.521391	4.038802317

G

Pictures of Final Crack Pattern from Crack Formation Tests

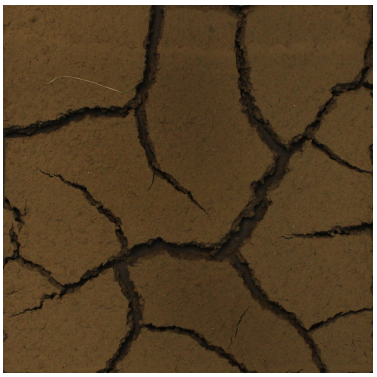

(a) Final crack pattern for SP-1.1 from March 2024.

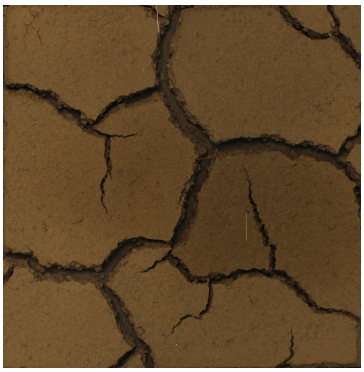

(b) Final crack pattern for SP-1.2 from March 2024.

(c) Final crack pattern for SP-4.1 from March 2024.

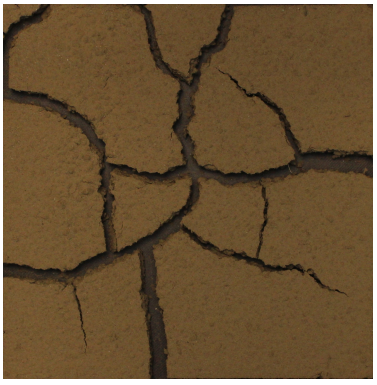

(a) Final crack pattern for SP-4.2 from March 2024.

(b) Final crack pattern for SP-6.1 from March 2024.

(c) Final crack pattern for SP-6.2 from March 2024.

(a) Final crack pattern for SP-7.1 from March 2024.

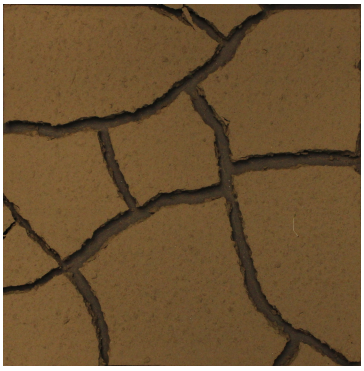

(b) Final crack pattern for SP-7.2 from March 2024.

(c) Final crack pattern for SP-9.1 from March 2024.

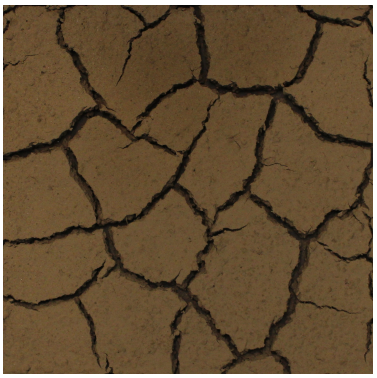

(a) Final crack pattern for SP-9.2 from March 2024.

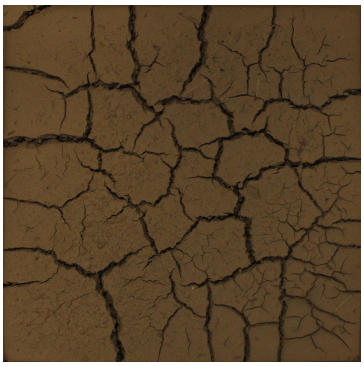

(b) Final crack pattern for SP-1.1 from September 2024.

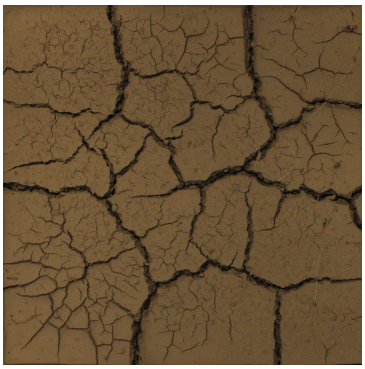

(c) Final crack pattern for SP-1.2 from September 2024.

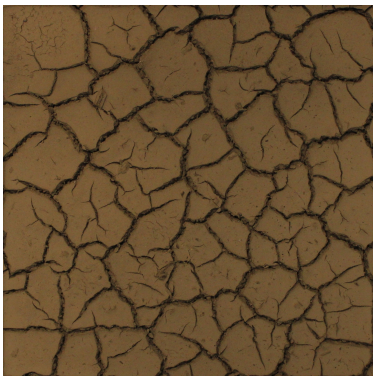

(a) Final crack pattern for SP-4.1 from September 2024.

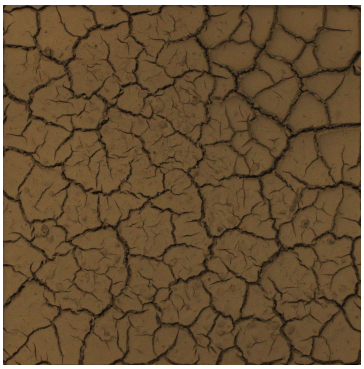

(b) Final crack pattern for SP-4.2 from September 2024.

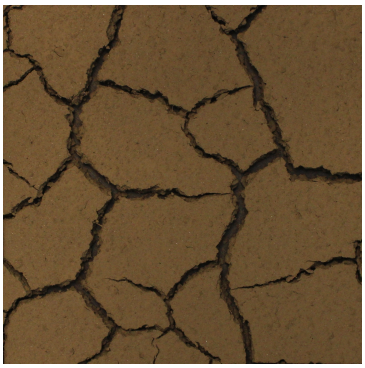

(c) Final crack pattern for SP-6.1 from September 2024.

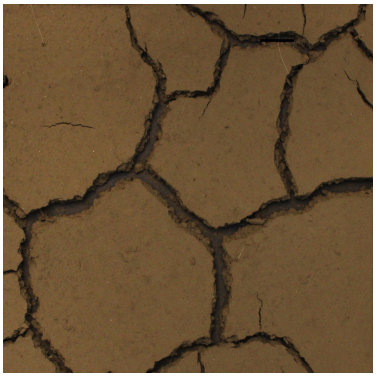

(a) Final crack pattern for SP-6.2 from September 2024.

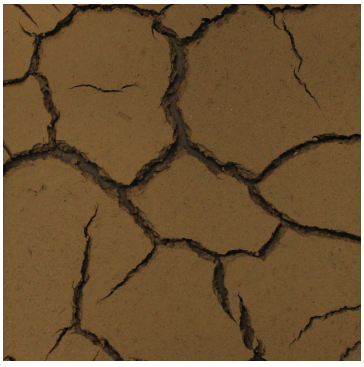

(b) Final crack pattern for SP-7.1 from September 2024.

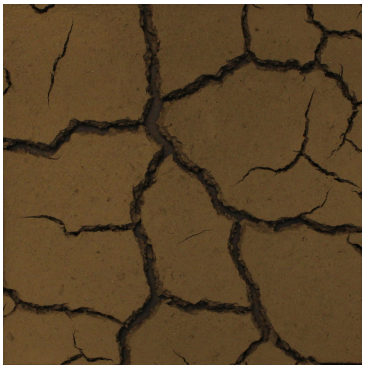

(c) Final crack pattern for SP-7.2 from September 2024.

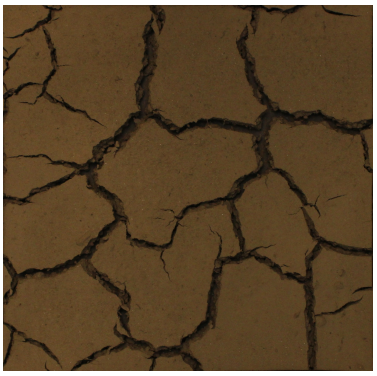

(a) Final crack pattern for SP-9.1 from September 2024.

(b) Final crack pattern for SP-9.2 from September 2024.

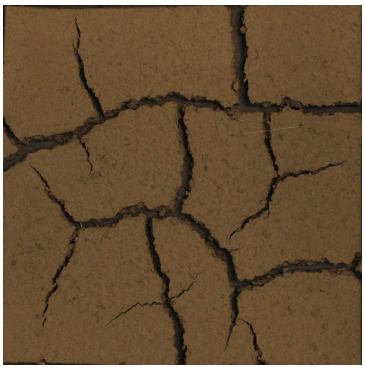

(c) Final crack pattern for SP-1.1 from March 2025.

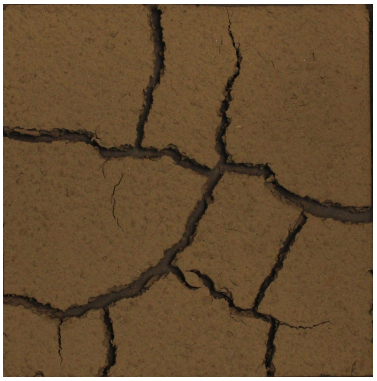

(a) Final crack pattern for SP-1.2 from March 2025.

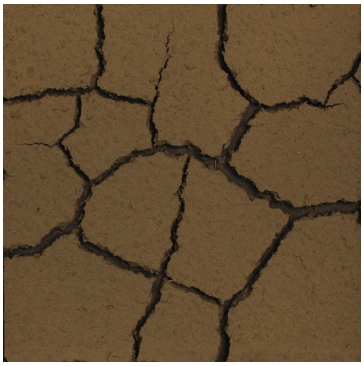

(b) Final crack pattern for SP-4.1 from March 2025.

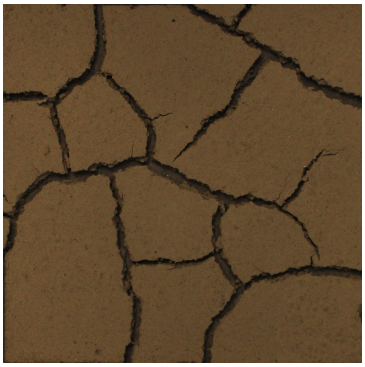

(c) Final crack pattern for SP-4.2 from March 2025.

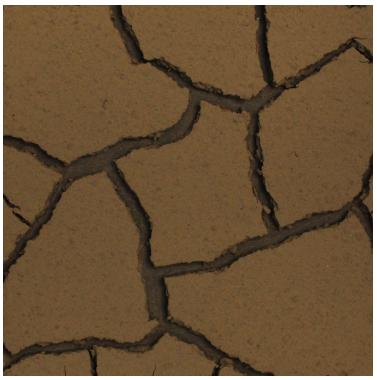

(a) Final crack pattern for SP-6.1 from March 2025.

(b) Final crack pattern for SP-6.2 from March 2025.

(c) Final crack pattern for SP-7.1 from March 2025.

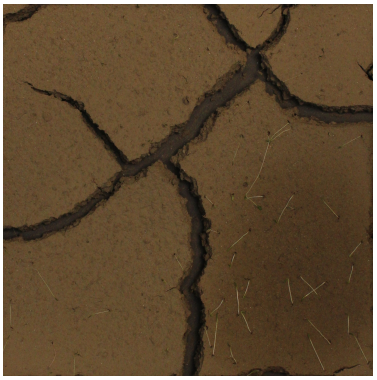

(a) Final crack pattern for SP-7.2 from March 2025.

(b) Final crack pattern for SP-9.1 from March 2025.

(c) Final crack pattern for SP-9.2 from March 2025.

H

Raw Crack Formation Data

Table H.1: Crack intensity factor results.

Samples	CIF 1 (-)	CIF 2 (-)	CIF Avg (-)
SP-1 03/24	0.15078	0.13047	0.140625
SP-4 03/24	0.14765	0.14043	0.14404
SP-6 03/24	0.13737	0.14439	0.14088
SP-7 03/24	0.13776	0.15428	0.14602
SP-9 03/24	0.12081	0.13728	0.129045
SP1 09/24	0.12793	0.11509	0.12151
SP4 09/24	0.2101	0.1763	0.1932
SP6 09/24	0.14027	0.15745	0.14886
SP7 09/24	0.14277	0.16443	0.1536
SP9 09/24	0.15727	0.22772	0.192495
SP1 03/25	0.11376	0.11701	0.115385
SP4 03/25	0.11574	0.12924	0.12249
SP6 03/25	0.16123	0.13766	0.149445
SP7 03/25	0.17347	0.11545	0.14446
SP9 03/25	0.19197	0.19289	0.19243
HIP	0.26913	0.29104	0.280085

Table H.2: Average crack width results.

Samples	Width 1 (pixels)	Width 2 (pixels)	W Avg (-)
SP-1 03/24	37.5277	32.9903	35.259
SP-4 03/24	44.1345	47.234	45.68425
SP-6 03/24	52.466	54.5415	53.50375
SP-7 03/24	48.9205	50.4759	49.6982
SP-9 03/24	26.0281	27.4699	26.749
SP1 09/24	14.5367	13.1165	13.8266
SP4 09/24	19.239	12.8228	16.0309
SP6 09/24	33.2952	46.3763	39.83575
SP7 09/24	37.0865	42.572	39.82925
SP9 09/24	28.0901	29.6391	28.8646
SP1 03/25	27.9129	33.5331	30.723
SP4 03/25	31.4823	30.9336	31.20795
SP6 03/25	50.549	50.536	50.5425
SP7 03/25	46.0906	42.7497	44.42015
SP9 03/25	26.2141	26.203	26.20855
HIP	87.6322	77.3519	82.49205

Table H.3: Average number of cracks results.

Samples	Cracks 1 (-)	Cracks 2 (-)	C Avg (-)
SP-1 03/24	29	27	28
SP-4 03/24	27	21	24
SP-6 03/24	12	19	15.5
SP-7 03/24	18	18	18
SP-9 03/24	39	46	42.5
SP1 09/24	139	133	136
SP4 09/24	229	277	253
SP6 09/24	36	28	32
SP7 09/24	28	33	30.5
SP9 09/24	72	142	107
SP1 03/25	44	29	36.5
SP4 03/25	39	35	37
SP6 03/25	33	20	26.5
SP7 03/25	27	17	22
SP9 03/25	117	93	105
HIP	24	35	29.5